ACTIVE NANOPHOTONIC DEVICES FACILITATED BY ENGINEERED DIPOLE MODES

A Dissertation
Presented to
The Academic Faculty

by

Kyutae Lee

In Partial Fulfillment
of the Requirements for the Degree
Doctor of Philosophy in the
School of Electrical and Computer Engineering

Georgia Institute of Technology
August 2021

ACTIVE NANOPHOTONIC DEVICES FACILITATED BY ENGINEERED DIPOLE MODES

Approved by:

Dr. Wenshan Cai, Advisor
School of Electrical & Computer Engineering
Georgia Institute of Technology

Dr. Andrew Peterson
School of Electrical & Computer Engineering
Georgia Institute of Technology

Dr. Ali Adibi
School of Electrical & Computer Engineering
Georgia Institute of Technology

Dr. Zhuomin Zhang
School of Mechanical Engineering
Georgia Institute of Technology

Dr. Benjamin Klein
Department of Electrical & Computer Engineering
Kennesaw State University

Date Approved: July 22, 2021

To my wife and family,

Whose endless love and support made this work possible.

ACKNOWLEDGEMENTS

First and foremost, I would like to thank my advisor, Prof. Wenshan Cai, for his continuous scientific guidance and great support throughout my Ph.D. study at Georgia Tech. He encouraged me to maximize my potential as an engineer, helped to teach me how to carry out research, guided me with his immense knowledge of science, and taught me to write a journal paper line by line. He has built an incredible optics lab and the nice memories of managing the optic lab for the past 5 years will always remain in my memory. I would also like to thank my thesis committee members Dr. Ali Adibi, Dr. Benjamin Klein, Dr. Andrew Peterson, and Dr. Zhuomin Zhang for their invaluable guidance and for their time and energy in meeting with me and reviewing my thesis document. I'm indebted to the dedication of my labmates, Dr. Mohammad Taghinejad, Dr. Sean P. Rodrigues, Dr. Shoufeng Lan, Dr. Zhaocheng Liu, Lakshmi Raju, Dayu Zhu and Andrew Kim. I was impressed by Mohammad's vast knowledge in science, inspired by his passion for research, and able to learn a lot from conversations with him. I wish the best of luck to the new group member Anjan Goswami and Chiyu Yang.

I would especially like to thank to Professor Doo-Hyun Ko in Kyung Hee University, who was my previous advisor and is now my great collaborator. He gave me unwavering support not only when I was pursuing my Master's degree under his guidance but also during my Ph.D. study at Georgia Tech. During our collaborations, I had the opportunity to work with talented and hard-working members of the Ko Lab, particularly with my friend Byunghoon Kim. Without his knowledge on Chemistry and effort on device

fabrication, optical characterization, and material synthesis, I won't able to demonstrate upconversion nanoparticle related work in this thesis.

Finally, I would like to thank my family for their love and support throughout the years. I would not have made it here without them. With the outmost gratitude and love for my wife, who saw me through my best and worst of graduate school. Over the years, she encouraged me whenever I got frustrated, sacrificed her career for me to pursue my personal dream. I am also thanks to my son, Jioh, for his love.

TABLE OF CONTENTS

LIST OF TABLES

LIST OF FIGURES

LIST OF SYMBOLS AND ABBREVIATIONS

ALD	atomic layer deposition
CD	circular dichroism
CMOS	complementary metal-oxide-semiconductor
DFG	difference frequency generation
DI	deionized
DTE	disulfonyldiarylethene
EBL	electron beam lithography
EFISH	electric-field induced second-harmonic
EFs	enhancement factors
ESA	excited state absorption
ETU	energy transfer upconversion
FDTD	finite-difference time-domain
GSA	ground state absorption
HWP	half waveplate
ICP-RIE	inductively coupled plasma - reactive ion etching
LCP	left circularly polarized
LP	linear polarizer
MIM	metal–insulator–metal
NIR	near-infrared
PFPE	perfluoropolyether
PHPS	perhydropolysilazane
PL	photoluminescence
PMMA	poly(methyl methacrylate)
QWP	quarter waveplate
QY	quantum yield
RCP	right circularly polarized
SEM	scanning electron microscopy
SFG	sum frequency generation
SHG	second harmonic generation
SOI	silicon on insulator
SPF	short-pass filter
SPPs	surface plasmon polaritons
TE	transverse electric
TEM	transmission electron microscope
TM	transverse magnetic

TMAH	tetramethylammonium hydroxide
TRPL	time-resolved photoluminescence
UC	upconversion
UCMM	upconverting chiral plasmonic metamaterials
UCNPs	upconversion nanoparticles
UCPL	upconversion photoluminescence
UV	ultraviolet
VIS	visible

SUMMARY

The miniaturization of optical components in the photonic field is driven by the demand for high performance, fast response time, and low power consumption. Microfabrication methods have shown a way to control the light, through structuring the bulk materials in micrometer sizes, such as Bragg gratings, optical cavities, and waveguides. Though the microfabrication approaches have enabled a dramatic development in optoelectronic devices, including the mobile phone, display, cameras, and laptop, the methods now facing challenges to further control of the light, especially in the optical region. This is because the wavelength of the incoming light is much smaller than the microstructures so that the light-matter interactions are limited by the bulk properties of optical materials. For example, the light phase is still governed by standard Snell's law and the diffraction limit induces difficulties to scale down the optical devices without degrading the optical performance.

Thanks to the recent development of nanofabrication techniques, including e-beam lithography, soft lithography, and focused ion beam lithography, it has provided the flexibility to further control the optical properties by using the subwavelength structures. In particular, the exotic and extraordinary electromagnetic phenomena were realized by arranging the nanostructures artificially that is not easy to achieve or not even available by using the bulk materials. These man-made materials, metamaterials, have been shown to manipulate the light phase, intensity, and even polarization states, by spatially arranging the nanostructures.

In the field of optics, the optical phenomena including the exotic optical properties stem from the interactions between incident waves and materials. From the interaction between the incident photon and the oscillating electron in the materials, the light could accumulate phase, generate heat, and become a source to excite an electromagnetic wave. In this context, scrutinizing the electron charge behavior in the matter is essential to understand the optical phenomena from the light-matter interaction. Therefore, scrutinizing multipole modes in the nanostructures is essential not only to predict the optical characteristics but also to design optical metamaterials.

The electromagnetic multipole expansion has been a powerful tool to analyze such novel structures as it is well suited for describing the scattering of light by small objects. Recently, a myriad of theories and methods are proposed to analyze the problem by multipole decomposition method. Such effort enabled to control of the electric/magnetic dipole and multipoles individually in the metamaterials or metasurfaces by controlling the geometrical parameters concisely. In this thesis, I will start by introducing important aspects of the light-matter interactions that are used in my work to actively control optical devices. Several electromagnetic multipole expansions will be described including the classical electromagnetic multipole decomposition method. By analyzing the light-matter interactions based on the multipole decomposition method, I will focus on the electric and magnetic dipolar moments to design active nanophotonic devices: 1) Utilizing the magnetic dipole mode in silicon to control nonlinear optical phenomena; 2) Enhanced photochemical switching by using the electric dipole modes in novel metals; 3) Forming a nonorthogonal electric and magnetic dipole modes for enantiomer selective detector.

CHAPTER 1. INTRODUCTION

Recently, the nanophononics field has shown dramatic progress ranging from exhibiting exotic optical properties to controlling the light wave more precisely (*1-3*). The important factors that carried the advance of nanophononics were the development of nano-fabrication technology and the progress of the multipole analysis methods. Nanofabrication technology, including e-beam lithography, soft lithography, and focused ion beam lithography, has provided the flexibility to control the geometry of the structure. Thanks to the development of nanofabrication technology, nanostructuring optical materials enabled to exhibit enrich the optical properties that the bulk materials could not possess (*1*). For example, an electromagnetic metamaterial, metasurfaces, plasmonic nanostructures were introduced at the nanophotonic fields that perform an extraordinary optical phenomenon, such as chirality (*4*, *5*) and optical nonlinearity (*6-8*). These properties are realized by controlling the light-matter interaction at the structured optical materials where the structure is comparable or smaller than the wavelength of the incident light. Furthermore, these unusual light behaviors were also has shown at the optical wavelength or at the near-infrared region which are rarely shown at the bulk material (*9*).

In the field of optics, most of the optical phenomena including the exotic optical properties stem from the interactions between incident waves and materials (*10*). When the matter is illuminated by an electromagnetic wave, it may convert some light to heat, or it may scatter the wave in all directions at the frequency of the incident beam. The first phenomenon is called absorption and the second phenomenon is called scattering. When the matter absorbs the incoming light, it converts its energy to excite the electrons in the

matter. The excited electrons undergo a relaxation process, while the energy of the excited electron is now converted to heat which elevates the local temperature. Then the elevated local temperature is transferred to the lattice via electron-phonon interactions and returns to the equilibrium condition. On the other hand, when it comes to light control, such as manipulation and propagation of the light at the photonic devices, light scattering plays a key role (*11*). The radiate scattered light results from the oscillation of charges in the matter that is excited by the oscillating electromagnetic field of the incident light. From the interaction between the incident photon and the oscillating electron, the light could accumulate phase or become a source to excite an electromagnetic wave with a new frequency. In this context, scrutinizing the electron charge behavior in the matter is essential to understand the optical phenomena from the light-matter interaction.

As I stated above, understanding the interaction between light and matter is necessary to actively control the optical properties at the nanostructure. The Mie scattering theory, which is named after Gustav Mie, provides a generalized solution that describes the scattering in the spherical media when an electromagnetic wave is incident upon it (*12*). When the size of the structure is comparable or smaller than the incident wavelength of the light, it precisely interprets and anticipates the scattered light from the matter by solving Maxwell's equations for the multipole radiation due to the electric polarization (*13*). As the results are derived by the behavior of the electrons in the material, the theory can be applied to most optical materials such as plasmonic, dielectric, and semiconductors. Therefore, the Mie-theory could promote to develop the active nanophotonic devices which are driven by the engineered dipole modes at the nanostructure.

1.1 Light-matter Interactions

1.1.1 Nonlinear Optics

In the event of the incoming light interacts with the matter, such interactions can be described within the electric dipolar approximation by the induced polarization P in a power series in the optical electric field E_ω:

$$\boldsymbol{P} = \varepsilon_0\left[\boldsymbol{\chi^{(1)}E_\omega} + \boldsymbol{\chi^{(2)}E_\omega E_\omega} + \boldsymbol{\chi^{(3)}E_\omega E_\omega E_\omega} + \cdots\right]. \quad (1)$$

The quantities ε_0 is the permittivity of free space and $\chi^{(1)}$, $\chi^{(2)}$ and $\chi^{(3)}$ are known as the first-, second- and third- order nonlinear optical susceptibilities, respectively (*14*). Higher-order susceptibilities are expressed using $\chi^{(n)}$, where n≥4, which is not shown in the equation. The first-order susceptibility is a tensor of second grade, χ_{ij}, which determines the linear optical properties. This linear dielectric tensor, which is determined by $\varepsilon=1+\chi^{(1)}$, represent the basis of the refractive indices of light wave in the material which explains the linear optical properties such as reflection and transmission. For simplicity, we assume the material is isotropic material, so that the quantities ε_0 and $\chi^{(1)}$ are considered as a simple scalar. To further simplify the interactions between the light and matters, we adopt a macroscopic view so that the detailed interactions are confined to the permittivity term.

The second-order susceptibility, $\chi^{(2)}$, is a third-rank tensor χ_{ijk}, which describes the second-order nonlinear processes such as second harmonic generation (SHG), sum/difference frequency generation (SFG / DFG), and the Pockels effects. And the third-order susceptibility, $\chi^{(3)}$, is represented by a fourth-rank tensor χ_{ijkl}, which explains the

third-order nonlinear processes as, for example, optical Kerr effect, four-wave mixing, and multi-photon absorptions. The higher-order susceptibilities are described as $\chi^{(n)}$ with (n+1 order tensor which is responsible for more complicated nonlinear effects. As we can expect from the nature of the power series expansions, the value of the elements of χ-tensors rapidly decreases as the order of the tensor increases. For example, in general, the second-order nonlinear effects are much stronger than the third-order or higher-order nonlinear processes (*15*).

Here, the main objective of utilizing the nonlinear process is to achieve large photon energy with small photon energy. One well-known way to achieve such nonlinearity is the SHG process as shown in Figure 1 (*14*). As illustrated in Figure 1a, two photons of frequency ω are converted to a photon of frequency 2ω. Figure 1b illustrates a standard SHG process where the material in which the $\chi^{(2)}$ is non-zero is excited by the incoming light. If we assume that the strength and the frequency of incoming light are E and ω, then the incoming light can be represented as

$$\tilde{E}(t) = Ee^{-i\omega t} + c.c. \tag{2}$$

By substituting the Eq. (2) into Eq. (1) and by taking the real part, we can extract the SHG process term as

$$P_{2\omega} \propto \chi^{(2)}(2\omega; \omega, \omega)E_{\omega}E_{\omega} \tag{3}$$

where $\chi^{(2)}$, E_{ω}, $P_{2\omega}$ represent the second-order dielectric susceptibility, the optical field at the fundamental frequency ω, and the induced second-harmonic nonlinear polarization at 2ω, respectively.

Though the three-wave mixing is the most standard method to generate the second-harmonic signal, the process is not allowed at the centrosymmetric materials as the even-order nonlinear susceptibility vanishes under the electric-dipole approximation. One way to achieve the SHG signal is by using the even-order nonlinear susceptibilities, which universally exist among the optical materials. An example is shown in Figure 1c, where the SHG signal is generated by using both the third-order susceptibility and the external static electric field. This process can be expressed as

$$P_{2\omega} \propto \boldsymbol{\chi}^{(3)}(2\omega; \omega, \omega, 0) E_{\omega} E_{\omega} E_{dc} \tag{4}$$

where $\chi^{(3)}$, E_{ω}, E_{dc}, $P_{2\omega}$ represent the third-order dielectric susceptibility, the optical field at the fundamental frequency ω, the static electric field provided from an external source, and the induced second-harmonic nonlinear polarization at 2ω, respectively. As the SHG process is achieved by incorporating the static electric fields, the process is called as electric field-induced second-harmonic generation (EFISH) process.(*6*, *16*)

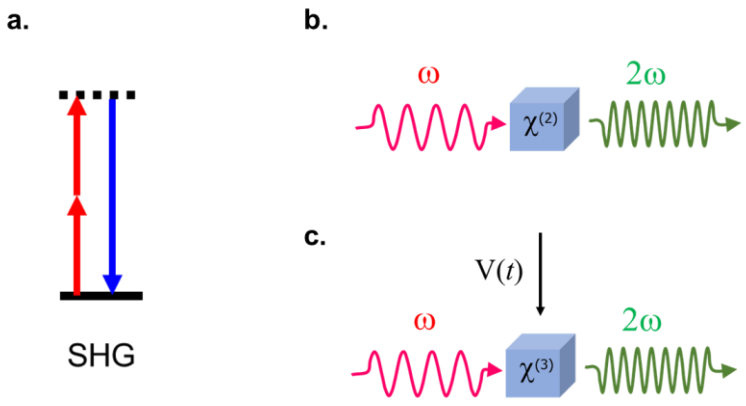

Figure 1. Second-harmonic generation process. (a) Second-harmonic generation process described by using the energy-level diagram. The solid line represents the real stat, and the dashed line represents the virtual level. The virtual level is not the real energy eigenstates and only describes the combined energy of the energy eigenstates of the atom. (b) Second-harmonic generation signal produced by using the $\chi^{(2)}$ material. (c) Second-harmonic generation signal produced by combining the static and incoming photons of frequency ω. This process is called electric-field induced second-harmonic generation.

1.1.2 Photon Upconversion Process

The photon upconversion process (UC) is an anti-Stokes type emission process that can convert the small energy photons to high-energy photons. Though the UC process produces similar results with the nonlinear process in terms of converting the small energy photons to the high energy photons, these two processes should be distinguished (*17*). The comparison between the upconversion and nonlinear process is shown in Figure 2. Figure 2a and b represent the upconversion process, while Figure 2c shows the SHG process. As shown in Figure 2, the SHG process involves virtual states so that it requires both high-intensity excitation and simultaneous photon absorption. On the other hand, upconversion processes go through with the real states. Therefore, low-power photons with subsequent absorption would be able to convert the low photon energy to the high photon energy.

The simplest upconversion process is the ground state absorption / excited state absorption (GSA/ESA). As shown in Figure 2a, the GSA/ESA process is achieved by absorbing two photons sequentially by a single ion. When the first photon is absorbed, the electron at the ground state jumps to the intermediate state. If the next photon is absorbed before the excited electron in the intermediate state transit back to the ground state, in other words, the lifetime of the intermediate is long enough, the absorbed photon energy elevates the electron to the higher excited state. The emission from the relaxation from this excited state to the ground state would possess higher photon energy than the incident photon energy. The Lanthanide ions (Ln^{3+}) is a well-known material that exhibits such upconversion luminescence (*18*). Especially, erbium ions (Er^{3+}) are commonly doped in the optical fiber two amplify the telecommunication signal through the upconversion process.

The most efficient upconversion process is ground state absorption/energy transfer upconversion (GSA/ETU). As shown in Figure 2b, the process requires two different ions which are a sensitizer and an activator. The sensitizer act as an absorber that has much higher absorption efficiency than the activator itself. When the small photons are incident to the material, sensitizer absorbs most of the photons. Then the sensitizer transfers its energy to the activator where the upconversion process occurs. The rest of the process is the same as the GSA/ESA process. As the process involves the energy transfer steps, the distance between the sensitizer and the activator ion is critical. Typically, these two ions are co-doped in the host materials, and the efficiency of the upconversion process is optimized by controlling the concentration of the two ions. Typically, $NaYF_4$ complex is

used as a host material, while the lanthanide ions such as Yb^{3+} and Er^{3+} ions are used as a sensitizer and an activator, respectively (*19, 20*).

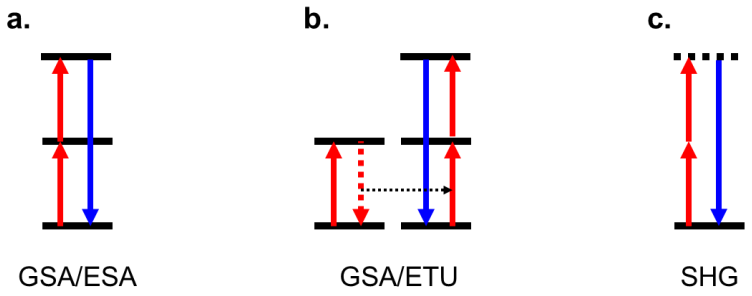

Figure 2. Low energy photons to high energy photons conversion processes. (a) The ground state absorption / excited state absorption process. (b) The ground state absorption/energy transfer upconversion process. (c) Second-harmonic generation nonlinear optical process. The solid black lines indicate the real energy levels while the dashed black lines indicate the virtual energy levels.

1.2 Analysis of the Light-Matter Interaction

The recent development of the nanofabrication technique has elevated the interest of the optical phenomena from light-matter interactions in subwavelength structures. The interest, in particular, has largely focused on realizing the exotic and extraordinary electromagnetic phenomena, such as negative refraction (*1, 8, 21*), super-resolution (*22*), and giant chirality (*23*), that is not easy to achieve or not even available by using the bulk materials. These novel phenomena were able to functionalize by arranging the nanostructures artificially to engineer the optical properties which are called metamaterials (*1*). Furthermore, recently, two-dimensional metamaterials, which is also called

metasurfaces, has shown that it could manipulate the light phase, intensity, and even polarization states, by spatially arranging the nanostructures (*2, 24*).

Naturally, the concept of metamaterials/metasurfaces leads to a need for the exact analysis of the light-matter interactions in the nanostructures. The electromagnetic multipole expansion has been a powerful tool to analyze such novel structures as it is well suited for describing the scattering of light by small objects (*10*). This is because the total scattered field from the light-matter interactions can be expressed by the superposition of the fields radiated by localized charge and current induced in the material. Unlike bulk materials that the electric dipole mode mainly involves the scattering properties, nanostructured materials are able to support higher-order multipoles which contribute to generate the prescribed extraordinary optical properties in metamaterials. Therefore, scrutinizing multipole modes in the nanostructures is essential not only to predict the optical characteristics but also to design optical metamaterials.

However, the classical multipole expansion methods are focused on the interaction between the light and an individual matter, where the metamaterial/metasurfaces consist of a set of nanostructures. These nanostructures, meta-atoms, not only interact with the incoming light but also interact with the scattered light from other meta-atoms. Therefore, a myriad of theories and methods are proposed to analyze the problem by multipole decomposition method including the method by using the induced current in the meta-atoms (*25*) and the method in the cartesian coordinates (*26*). Such effort enabled to control of the electric/magnetic dipole and multipoles individually in the metamaterials or metasurfaces by controlling the geometrical parameters concisely. In this section, I will start by describing the multipolar decomposition methods including the classical multipole

expansion method and recently proposed methods. By comparing their suitability for the analysis of periodic nanostructures, I then focus on two types of optical materials, plasmonics, and high refractive index materials, which are mainly applied to design metamaterials/metasurfaces.

1.2.1 Multipolar Decomposition Methods

The classical electromagnetic multipole expansion by solving the Maxwell equations for the scattered field for an individual particle is shown in Figure 3a (*10*). With the assumption of a source-free region of empty space, the scattered electric field, $\vec{E}$ can be found by solving the Maxwell equations as shown below (magnetic field, $\vec{H}$, can be derived by following the same procedure):

$$(\nabla^2 + k^2)\vec{E} = 0, \quad \nabla \cdot \vec{E} = 0, \quad \vec{H} = -\frac{i}{kZ_0}\nabla \times \vec{E} \tag{5}$$

where k and Z_0 represents the wave vector and impedance of free space, respectively. The general solution of Eq. (55) and Eq. (6) in spherical coordinate can be written as:

$$\vec{E} = Z_0 \sum_{l,m} \left[\frac{i}{k} a_E(l,m) \boldsymbol{\nabla} \times f_l(kr) \boldsymbol{X}_{l,m} + a_M(l,m) g_l(kr) \boldsymbol{X}_{l,m} \right] \tag{6}$$

where $a_E(l,m)$, $a_M(l,m)$, (l,m), r, and $\boldsymbol{X}_{l,m}$ represents electric multipole coefficients, magnetic multipole coefficients, integer that defines the specific order of multipoles, position vector, and normalized form of vector spherical harmonic, respectively. In Eq. (6),

$f_l(kr)$ and $g_l(kr)$ is the radial function which is express by a combination of spherical Hankel functions of the first and second kind. And the multipole coefficients can be determined by applying the sources and boundary conditions as:

$$Z_0 a_E(l,m) f_l(kr) = -\frac{k}{\sqrt{l(l+1)}} \int Y_{lm}^* \boldsymbol{r} \cdot \vec{E} d\Omega$$
$$a_M(l,m) g_l(kr) = \frac{k}{\sqrt{l(l+1)}} \int Y_{lm}^* \boldsymbol{r} \cdot \vec{H} d\Omega \quad (7)$$

As shown in Eq. (7), each electric multipole coefficient can be calculated where the total scattered field is the superposition of the fields created by a corresponding set of multipoles. For an individual particle, the classical multipole expansion method is able to determine the contribution of multipole modes to the scattered field. However, when the light interacts with many particles as shown in Figure 3b, the method cannot predict the exact contribution of multipole modes in each particle as particles interact with the scattered field by other particles.

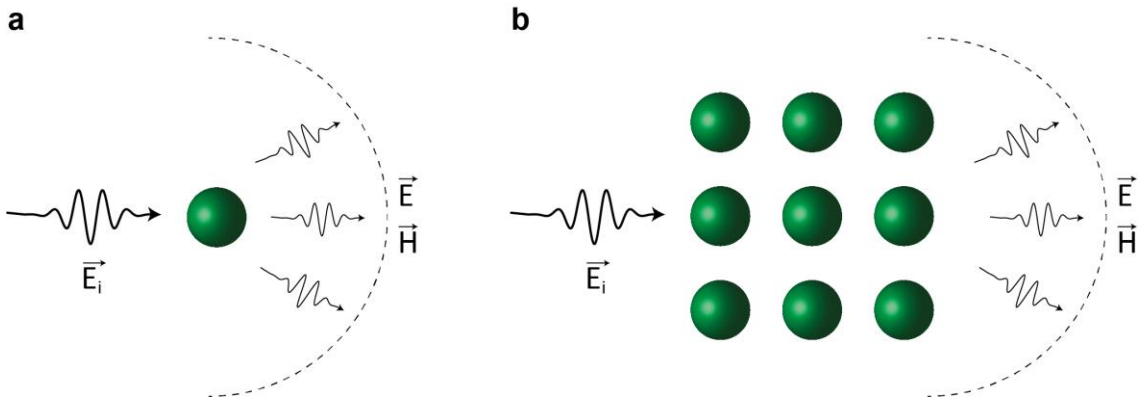

Figure 3. Illustration of the light-mater interactions. (a,b) Scattered electromagnetic field from a single particle and many particles.

To overcome the limitation of the classical multiple expansion, alternative approaches were introduced which are based on the induced electric current in nanostructures by the incident light (*25-27*). The multipole expansion by using the induced electric current in scatterers can be expressed in both the spherical and the Cartesian coordinates. Unlike the spherical multipole expansion, the multipole expansion in the Cartesian coordinates can distinguish the contribution from the toroidal multipoles (*28*). In this thesis, I will focus on the dipolar electric and magnetic modes and ignore the contribution from the toroidal multipoles that appear from the third-order multipoles.

The induced polarization, *P*, in the nanostructure can be described as:

$$\vec{P} = \varepsilon_0(\varepsilon_r - \varepsilon_{r,d})\vec{E} \tag{8}$$

whereε_0, ε_r, and $\varepsilon_{r,d}$ are the vacuum dielectric constant, relative dielectric permittivity of the scatterers, and relative dielectric permittivity of the surrounding medium, respectively. In Eq. (8), $\vec{E}$ is the total electric field inside the nanoparticle which includes the interactions between the nanoparticles and the scattered field from other nanoparticles. Then, the induced polarization, or the induced current $\vec{J} = -i\omega\vec{P}$, can be expanded in a Taylor series as:

$$\vec{P}(\boldsymbol{r}) = \int \vec{P}\,(\boldsymbol{r}')\delta(\boldsymbol{r} - \boldsymbol{r}')d\boldsymbol{r}' \approx \vec{p}\delta(\boldsymbol{r}) + \frac{i}{\omega}[\boldsymbol{\nabla} \times \vec{m}\delta(\boldsymbol{r})] \tag{9}$$

where δ is the Dirac delta function, and $\vec{p} = \int \vec{P}(\boldsymbol{r}')\, d\boldsymbol{r}'$ and $\vec{m} = -\frac{i\omega}{2}\int [\boldsymbol{r}' \times \vec{P}(\boldsymbol{r}')]\, d\boldsymbol{r}'$ is the electric and magnetic dipole moment. Then the scattered electric field in the far field by electric and magnetic dipole moment can be expressed by (*28*):

$$\overrightarrow{E_s}(\boldsymbol{r}) \approx \frac{k_0^2 e^{ik_d(r-\boldsymbol{n}\boldsymbol{r_0})}}{4\pi\varepsilon_0 \boldsymbol{r}} \left\{ [\boldsymbol{n} \times (\vec{p} \times \boldsymbol{n})] + \frac{1}{v_d} (\vec{m}(\boldsymbol{r_0}) \times \boldsymbol{n}) \right\} \tag{10}$$

where k_d and v_d are the wavenumber and light phase velocity in the surrounding medium, respectively, and $\boldsymbol{n}$ is the unit vector directed along the radius vector **r**.

1.2.2 Plasmonics

When the frequency of the incident light could evoke the dipole mode in the small matter, the electrons in the matter oscillate at the frequency matched with the incoming light (*10*). In noble metals, such as gold, silver, and copper, the effect becomes much stronger at the surface due to the free electrons. This strong confinement of the electric field due to the interaction between the incoming light and the free electrons is named as surface plasmon effect (*29-31*). The properties of surface plasmon such as resonance frequency and intensity of the confined electric field are strongly depending on the geometry of the metal structures and their surrounding environment. Furthermore, the geometry determines the type of the surface plasmon such as wave-like plasmon mode, which is named as surface plasmon polaritons, and the strong field localization on the surface, which is the localized surface plasmon effect. The localized surface plasmons lead to a strong field enhancement near the surface which is beneficial in diverse fields such as

surface-enhanced Raman spectroscopy (*32*), surface plasmon catalytic (*33*), and hot-electron generation and transfer process (*7, 34*).

The distinct optical properties of noble metals stem from the bound and free electrons in the metallic structures. The dielectric response of the metal in terms of electronic behavior is described by the Drude model as:

$$\boldsymbol{\varepsilon_{\mathrm{m}}(\omega) = \varepsilon_b(\omega) - \frac{\omega_p^2}{\omega(\omega + i\Gamma)}} \ , \boldsymbol{where\ \omega_p = \sqrt{\frac{n_e e^2}{\varepsilon_0 m_e^*}}} \tag{11}$$

where $\varepsilon_b(\omega)$ represents the contribution of bound electrons, ω_p is the bulk plasma frequency, n_e is the free electron density, m_e^* is the electron effective mass, ε_0 is the free space permittivity, and Γ is the electron scattering rate (*1*). When the transverse magnetic mode (TM mode) of light excites the interface of the metal and dielectric layer, collective electron oscillations coupled with light which is known as surface plasmon polaritons (SPPs). The SPPs dispersion relation can be derived as:

$$\boldsymbol{k_{spp} = \frac{\omega}{c}\sqrt{\frac{\varepsilon_d \varepsilon_m}{\varepsilon_d + \varepsilon_m}}} \tag{12}$$

where $\varepsilon_d(\omega)$ represents the permittivity of dielectric material and c represents the speed of light. The permittivity of metal is negative up to visible or even ultra-violet wavelength that produces large k_{spp}. The large k_{spp} implies that the SPPs wavelength is able to reach nanoscale at the optical frequency that is much smaller than the incident wavelength of light.

The SPPs can be further confined at the metal-dielectric interfaces by shrinking down the dimensions of the metallic nanostructures. The tight confinement of the SPPs at the metallic nanoparticle, which is known as localized surface plasmons, gives rise to the significant enhancement of the local field around the nanoparticle. By assuming a spherical metallic nanoparticle placed in an electric field, the localized surface plasmons can be modeled as an electric dipole as (*35*):

$$\vec{p} = 4\pi R^3 \frac{\varepsilon_m - \varepsilon_d}{\varepsilon_m + 2\varepsilon_d} \varepsilon_m \overrightarrow{E_0} \tag{13}$$

where R and $\overrightarrow{E_0}$ represent the radius of nanoparticle and electric field. The Eq. (13) shows that the electric dipole mode can be tuned by modifying the geometrical parameters of nanoparticles and the resonance can be achieved when the $|\varepsilon_m(\omega) + 2\varepsilon\_d|$ become minimum.

The capability of metamaterials to engineer the electromagnetic properties is based on engineering the effective refractive index of the material. As the effective refractive index can be described by using the electric permittivity and the magnetic permeability, tailoring the electric and magnetic moment is the key to the metamaterials. As mentioned above, the plasmonic structures are well-known to control the electric moment by controlling the geometrical parameters, while it could not possess a strong magnetic moment as the field inside the metal is not allowed. Accordingly, to fully utilize the plasmonic materials as metamaterials, it is necessary to possess the ability to tune the magnetic moment which can be induced by the circulating current (*3*). Consequently, geometrical considerations of the plasmonic metamaterials are focused on inducing the

magnetic moment such as split-ring resonator shapes and the metal-insulator-metal shapes (*36, 37*).

1.2.3 Dielectric / Semiconductor materials

The mechanism for the creation of magnetic or electric resonances in the materials is called Mie resonance, which is named after Gustav Mie, a German professor of physics, in 1908 (*12*). However, thanks to the development of nanofabrication technology, the utilization of the Mie theory to control the light with the dielectric metamaterials has been demonstrated recently (*38, 39*). The use of high-index materials, such as dielectric and semiconductors, has given more flexibility to design the meta-atoms to construct metamaterials or metasurfaces compared to the plasmonic materials. This is because, unlike plasmonic materials such as silver and gold, the high-index materials could possess the electric field inside the structure so that the electric/magnetic or both resonances are able to exist in the materials. On the other hand, the plasmonic structure should be designed to induce the magnetic moments externally. Furthermore, the plasmonic structures exhibit undesired loss at the optical wavelength, while the high-index materials generally show a low optical loss.

The concept of the semiconductor Mie resonator combined with the nonlinear optics has shown a promising way to exploit semiconductor materials as a nonlinear medium. For example, silicon which is the most important materials in both electric and optical field has been demonstrated as a nonlinear material which can largely enhance harmonic generation signal using the magnetic dipole resonance (*40-42*). Moreover, the

active nonlinear device using the Mie type silicon resonator has been demonstrated recently (*43*). The development of the semiconductor metamaterials/metasurfaces enabled a way to fully control the incident light which can be a promising candidate to achieve the integrated optics devices.

CHAPTER 2. SILICON METASURFACES WITH MAGNETIC MIE RESONANCE FOR TUNABLE HARMONIC GENERATION OF LIGHT VIA ELECTRICAL CONTROL

Silicon, as the premier material in the complementary metal-oxide-semiconductor (CMOS) technology, has been vastly adopted for the implementation of photonic systems to enable various on-chip optical functionalities through the integration of optics and electronics (*44*). The use of silicon in integrated photonics, however, is restricted due to the absence of the bulk second-order nonlinear susceptibility, $\chi^{(2)}$, under the electric dipole approximation. To circumvent this challenge, we introduce an induced second-order nonlinear response facilitates SHG across the depletion region through a process best known as the electric-field induced second-harmonic (EFISH) generation (*16, 45*).

The EFISH generation process is ubiquitous as it depends on the third-order nonlinear susceptibility:

$$P_{2\omega}^{NL} \propto \chi^{(3)}(2\omega;\omega,\omega,0)E_{\omega}E_{\omega}E_{dc} \tag{14}$$

where $\chi^{(3)}$, E_{ω}, E_{dc}, $P_{2\omega}^{NL}$ represent the third-order dielectric susceptibility, the optical field at the fundamental frequency ω, the static electric field, and the induced second-harmonic nonlinear polarization at 2ω, respectively. While externally triggered $\chi^{(2)}$ behavior can be realized in various optical media, under the EFISH scheme the efficiency of the second-order nonlinear processes is rather limited due to the weak $\chi^{(3)}$

responses. One way to enhance the EFISH generation based on Eq. (14) is by boosting the optical field (E_ω). The local field enhancement can be obtained through the formation of a resonant mode in the structure at a target wavelength. For example, high refractive index semiconductor nanostructures have been exploited to create a significant resonant enhancement of both electric and magnetic fields, facilitated by the formation of Mie-type resonance modes (*40, 42, 46*). Indeed, magnetic dipolar Mie resonance has been reported to improve nonlinear optical responses (*41, 42, 47*).

In this work, we demonstrate the enhancement and tunability of field-induced optical nonlinearity of the second-order type in silicon metasurfaces, where strong magnetic Mie resonances are leveraged to intensify the nonlinear interaction of light with silicon at a prescribed spectral range. On top of the strengthened surface SHG from the silicon metasurface, as facilitated by the magnetic Mie effect, introducing an electrical signal to our silicon structure provides an additional route to the frequency-doubling of light via the EFISH process. Our experiments reveal that a substantial SHG enhancement is achievable at the spectral vicinity of the magnetic Mie resonances, which is exclusively accessible via TM-polarized illuminations. Simulation results accurately corroborate our experimental observations, verifying the essential role of the magnetic Mie resonance on the observed nonlinear responses in silicon-based metasurfaces.

2.1 Mie-type Silicon nanostructures for electrically-controlled nonlinear signal

The dielectric metasurfaces comprise one-dimensional arrays of (100) crystalline silicon with a rectangular cross section, as schematically illustrated in Figure 4a. The field-

induced nonlinearity in such silicon structures is critically correlated to the crystallinity and direction of the material, as will be detailed in a later part of this paper. To experimentally elucidate the role of the magnetic Mie resonance on the strength of nonlinear light-matter interactions, five different metasurfaces with varying geometrical parameters are fabricated, as described in Figure 4. The structural parameters of the samples are carefully chosen via finite-differential time-domain simulations, so that all the silicon metasurfaces share a magnetic Mie resonance at the same operating wavelength, but with different level of field enhancement. The unit height (h) and width (w) of the silicon gratings are fixed at 190 nm and 130 nm, respectively, as the spectral location of the magnetic Mie resonance is dictated by the dimension of the individual silicon bar instead of their mutual interactions. In addition, the silicon strips are arranged at five different periodicities (p), from 280 nm (sample S1) to 480 nm (sample S5) at a 50 nm interval, in order to control the field enhancement in the silicon metasurfaces (Figure 4b-e). An unpatterned, planar silicon pad, S6, is also prepared as a control sample to substantiate the role of the magnetic resonance on the second-harmonic response of the silicon platform.

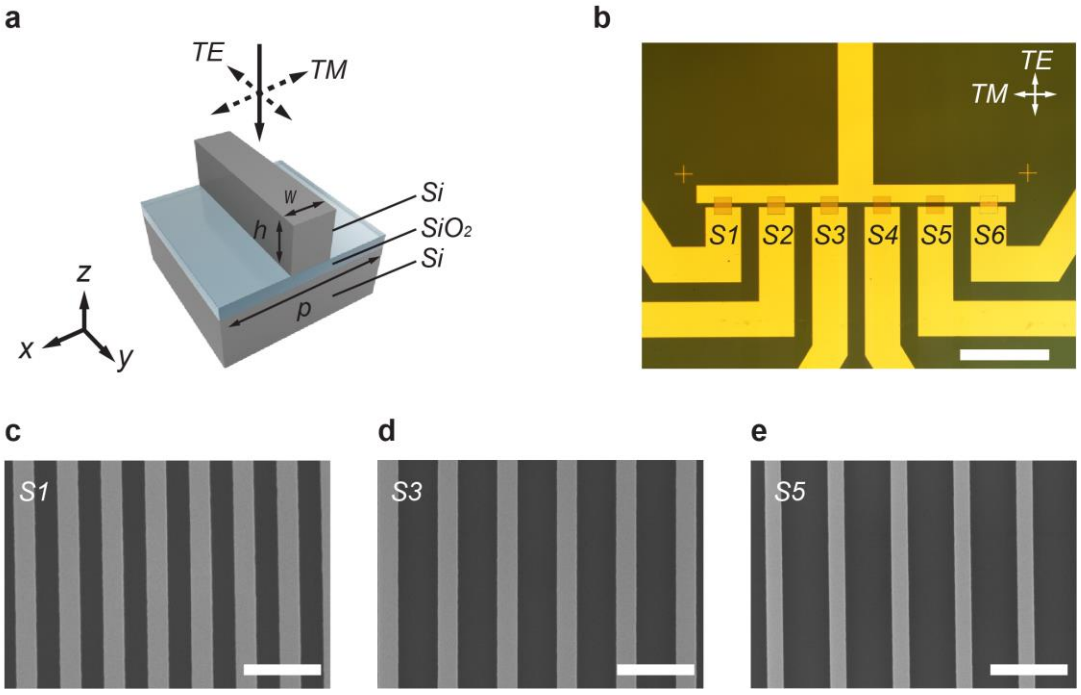

Figure 4. Schematic, optical microscope, and scanning electron microscope images of the silicon metasurfaces with electrical connections. (a) Schematic illustration of a unit cell of the silicon metasurfaces. The width (w) and height (h) of each bar are fixed to be 130 nm and 190 nm, respectively. The TM (TE) polarization of the incident light is defined when its electric field is parallel (perpendicular) to x-z plane, as depicted. (b) Optical microscope image of the fabricated device. Silicon metasurfaces with different periodicities are labeled from S1 to S5, whose periodicity varies from 280 nm to 480 nm at a 50 nm interval. An unpatterned silicon pad is also prepared (labeled as S6) for comparison purpose. The scale bar represents 1 mm. (c-e) SEM images of three representative metasurfaces, S1, S3, and S5. The scale bars represent 500 nm.

2.2 Linear optical characteristics and calculations

Figure 5a depicts the linear optical reflection spectra of the silicon metasurfaces, acquired under TM-polarized illumination at a normal incident angle. The observed broad reflection band can be explained based on the spectral proximity of the electric- and magnetic-dipole modes formed within the silicon nanostructure. We elucidate this speculation by performing finite-difference time-domain simulations, aiming to identify

the resonance nature of the dipolar modes through the field distributions inside the Si gratings. As shown in Figure 5b, the calculated reflection spectra of metasurfaces are in good agreement with the measured ones, except for a slight spectral redshift due to fabrication imperfections.

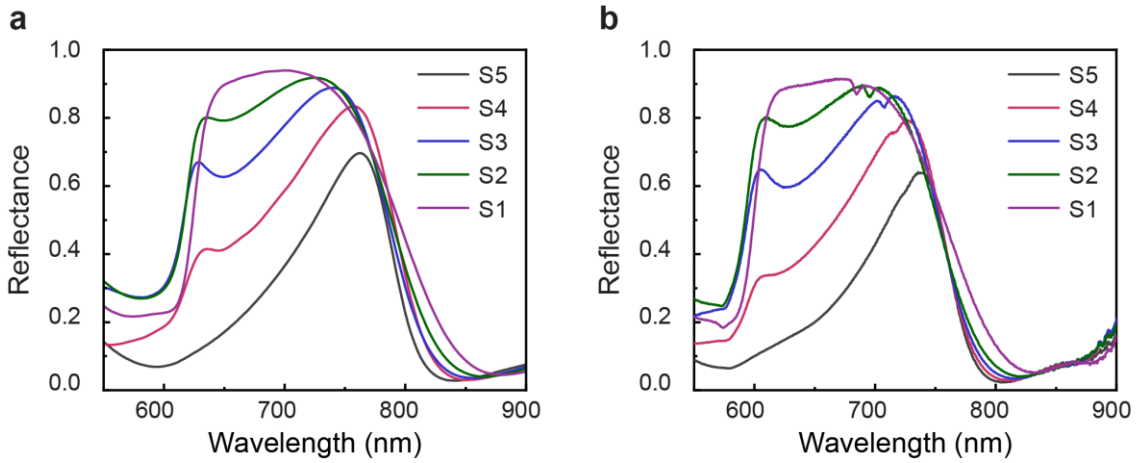

Figure 5. Linear optical properties of the silicon metasurfaces. (a, b) Measured (a) and calculated (b) reflection spectra of the five silicon metasurfaces under TM polarized illumination. Remarkable agreement between the numerical and experimental results is identified.

For a representative case of sample S3 with a periodicity of 380 nm, the field enhancement profiles at various wavelengths (Figure 6c) reveal the formation of a magnetic resonance mode at the wavelength of 785 nm, as evidenced by the circulating nature of the electric field within the cross-section of each silicon strip. This strong magnetic Mie resonance is only accessible via TM-polarized illumination and disappears as the polarization of light is switched to the TE state. By comparing the measured reflection spectra to the simulated ones, we expect a magnetic Mie resonance of the fabricated device to occur at the wavelength of 750 nm. Furthermore, at this specific wavelength, all metasurface samples exhibit nearly-identical magnitude of optical

reflection (Figure 5a), which allows for a fair comparison of the nonlinear interaction of light with this set of samples, independent of their linear light absorption.

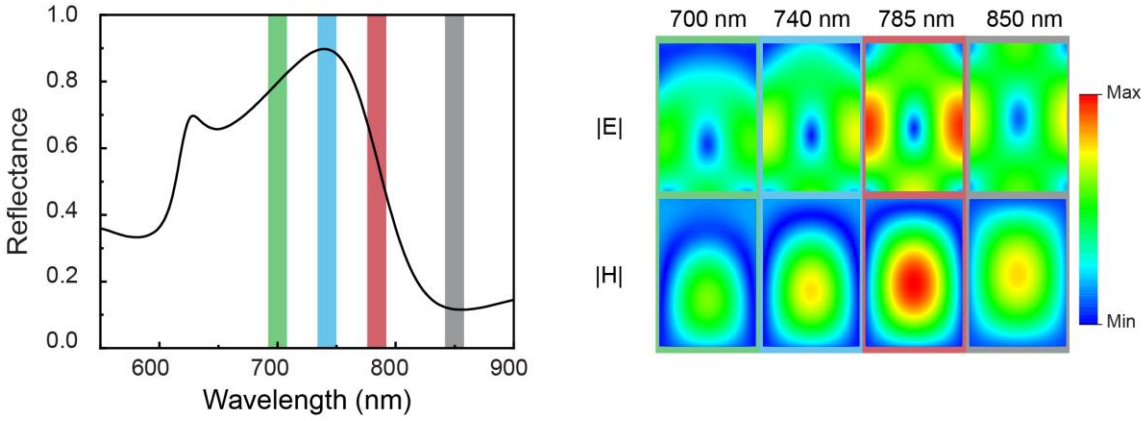

Figure 6. Simulated reflectance spectrum and field distribution of one representative sample (S3). The vertical color bars indicate selective wavelengths at 700 nm (green), 740 nm (blue), 785 nm (red), and 850 nm (gray). Cross-sectional views of the normalized electric and magnetic field distributions at these wavelengths are presented on the right. Strong field enhancement is shown at the wavelength of 785 nm, induced by the magnetic Mie resonance mode.

2.3 Nonlinear optical characteristics and calculations

Prior to examining the role of the magnetic Mie resonance on the EFISH generation, we first characterized the static SHG signals from the silicon metasurfaces. This helps to identify the impact of the magnetic Mie resonance on the enhancement of the nonlinear light generation from the silicon nanostructures. Since grating samples are made from single crystalline silicon, the second-order nonlinear processes are essentially forbidden under the electric-dipole approximation, surfaces and interfaces are the possible locations where the termination of bulk crystal lattice allows for optical nonlinearities of the second order. Figure 7 illustrates the acquired spectra of the SHG signals of the six devices, when the metasurfaces are excited by TM-polarized laser pulses of varying fundamental

wavelength λ_ω, from 720 to 900 nm, at a constant intensity. In most devices, the frequency-doubling process appears most efficient at the fundamental wavelength of 750 nm, which is precisely the spectral location of the magnetic Mie resonance as identified through the linear optical characterizations. Devices with a weak magnetic Mie resonance, sample S1 for instance, exhibits a weak nonlinear response resembling that of the unpatterned control sample S6.

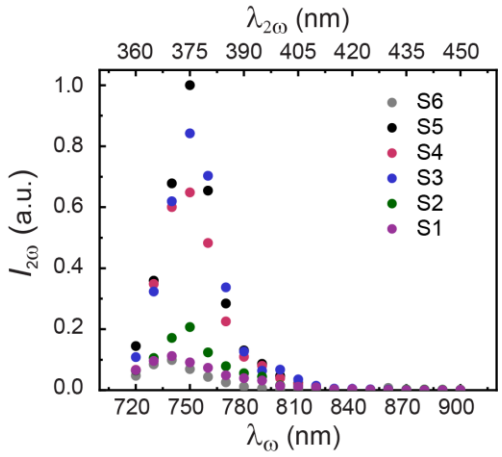

Figure 7. Static nonlinear optical responses from the silicon metasurfaces. Measured magnitude of the SHG from the six silicon patterns for fundamental waves of varying wavelength at a constant excitation intensity. Generally, the peak is observed at the fundamental wavelength of around 750 nm, which corresponds to the magnetic Mie resonance supported in the silicon strips.

To scrutinize the relationship between the magnetic Mie resonance mode and the SHG enhancement from the surface of the structures, we performed numerical calculations by incorporating the surface $\chi^{(2)}$ tensor of the (100) silicon and the field enhancement at the surface of the silicon devices. We first analyze the effective surface $\chi^{(2)}$ tensor induced by the electric field components of light at the silicon surface (*15*, *48*, *49*). The nonlinear surface polarization tensor ($P^{NL,\mathrm{surf}}$) for a (100) crystalline silicon is described below:

$$\begin{pmatrix} P_x^{NL,\mathrm{surf}} \\ P_y^{NL,\mathrm{surf}} \\ P_z^{NL,\mathrm{surf}} \end{pmatrix} = \begin{pmatrix} 0 & 0 & 0 & 0 & d_{15} & 0 \\ 0 & 0 & 0 & d_{15} & 0 & 0 \\ d_{31} & d_{31} & d_{33} & 0 & 0 & 0 \end{pmatrix} \begin{pmatrix} E_x^2 \\ E_y^2 \\ E_z^2 \\ 2E_yE_z \\ 2E_xE_z \\ 2E_xE_y \end{pmatrix} \quad (15)$$

where estimated values of d_{15} ~10^{-19}, d_{31} ~10^{-21}, and d_{33} ~10^{-18} m^2/V are used for the calculation (*50*). To evaluate the electric field components of the fundamental light at the surface of the silicon nanostructure, the electric field vector profile is simulated and then incorporated in the nonlinear calculations. For the case of sample S3, Figure 8 illustrates the electric field profile at the fundamental wavelength of 785 nm under the TM-polarization, which features a strong magnetic resonance with a circulating electric field concentrated around the silicon surface. This circulating field distribution implies that both the x- and z-components of the electric field inside the silicon gratings need to be included in the calculation of the nonlinear field profile. In contrast, for samples lacking a magnetic resonance mode, as seen in the unpatterned control sample (i.e., S6), the second-order nonlinear interaction of light with silicon is limited to the contribution from only the x-polarized field, under the TM excitations.

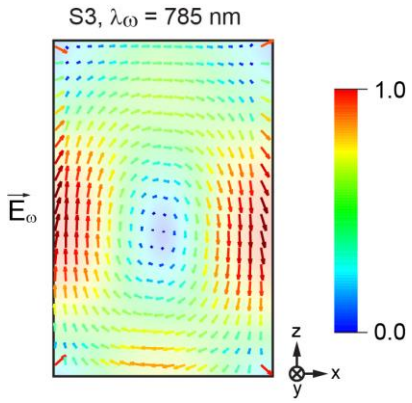

Figure 8. Cross-sectional view of the simulated electric field distribution at the Mie resonance wavelength (785 nm). The observed circulation of electric field in the grating is induced by the magnetic Mie resonance. The color of the arrows represents the normalized strength of the field vector.

Combining the field profile at the fundamental wavelength λ_ω and the surface second-order nonlinear tensor, the total nonlinear polarization responses of S6 and metasurfaces are described as:

$$\begin{aligned} P_{\text{tot,S6}}^{NL,\text{surf}} &= P_z^{NL,\text{surf}} = d_{31}E_x^2 \\ P_{\text{tot,meta}}^{NL,\text{surf}} &= P_x^{NL,\text{surf}} + P_z^{NL,\text{surf}} = 2d_{15}E_xE_z + d_{31}E_x^2 + d_{33}E_z^2. \end{aligned} \tag{16}$$

Compare to the unpatterned sample S6 where only the E_x component plays a role, silicon metasurfaces possess additional nonlinear polarization components induced by the E_z term at the surface of Si gratings. Furthermore, since the value of d_{31} is much smaller than the other two tensor elements, the nonlinear polarization of the metasurfaces is largely governed by the electric field along the z-direction, especially when the fundamental wavelength falls in the spectral vicinity of the magnetic Mie resonance mode. Since the E_z term at the grating surfaces dictates the total nonlinear polarization, the calculation of the SHG enhancement at the surface can be simplified by considering only two major factors: the enhancement of E_z at the silicon surfaces, and lateral filling ratio of the Si gratings. The

overall E_z enhancement is estimated by integrating the magnitude of E_z at silicon surfaces, and the filling ratio is defined as the width of the grating normalized to its periodicity (see Supporting Information for details). In the experiment, the generated frequency-doubled signal qualitatively follows the calculated nonlinear field intensity, except for sample S5, where the peak of the reflectance due to an electric dipole response merges with that of the magnetic Mie resonance. To elucidate the effect of the magnetic Mie resonance on the nonlinear optical response, without complication from other resonance modes, in subsequent studies we will focus on device S3, whose magnetic Mie mode is spectrally distant from the reflection peak.

Figure 9 shows the spectral behavior of the nonlinear optical generation from sample S3, together with its power dependence. The SHG spectra are characterized by varying the fundamental wavelength from 720 to 840 nm, with a step size of 10 nm, while the intensity and polarization states remain unaltered. The collected intensity of SHG signals is normalized to the maximum intensity occurring at the fundamental wavelength of 750 nm. The inset of Figure 9 presents the relationship between the intensity of the SHG output ($I_{2\omega}$) and that of the fundamental light (I_{ω}). The acquired signals are plotted in a double logarithmic scale and fitted with a function $I_{2\omega} \propto I_{\omega}^{K}$, where K = 2.09 is obtained from the least square fitting method. This quadratic relation further confirms the nature of the collected nonlinear signal from the silicon metasurfaces.

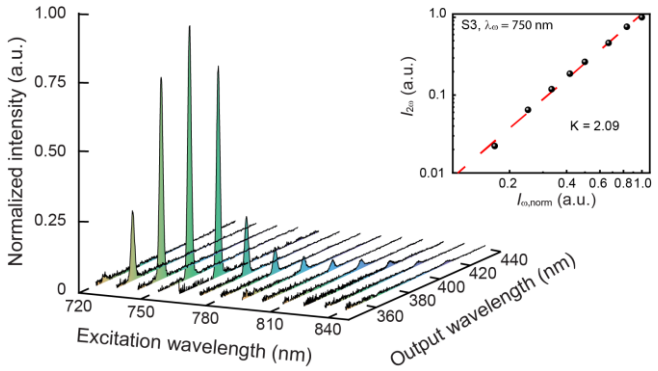

Figure 9. Second harmonic signal from sample S3 at a series of excitation wavelength of a constant intensity. The inset exhibits the power dependence of the generated second harmonic signal from sample S3 on the intensity of the fundamental light at λ_ω = 750 nm. The dashed line in the double logarithmic plot represents a slope of 2.09, which is estimated by using the least-square method.

2.4 Electrically induced nonlinear optical response

Now that we have addressed the origin and characteristics of the static SHG from the silicon metasurfaces, in the following part, we will modulate the magnitude of the harmonic signal using a bias voltage, and further elucidate the role of the magnetic Mie resonance on the achievable EFISH generation. Figure 10 shows the calculated field maps for the fundamental and the EFISH signals from device S3, at the fundamental wavelength of 785 nm and 850 nm, respectively. These two wavelengths correspond to the cases with and without the magnetic Mie resonance mode, and the field values have been normalized to their respective maxima for the fundamental wavelength of 785 nm. As expected, the fundamental field within the cross section of the silicon strips at 785 nm is substantially stronger compared to that at 850 nm, thanks to the field localization and enhancement facilitated by the strong magnetic Mie resonance. As for the calculated field map for EFISH generation (bottom row of Figure 10), unlike the static SHG analysis, which is largely a

surface effect, the calculation of EFISH signal requires the consolidation of the spatial distributions of both the optical and static fields across the bulk of the silicon structure.

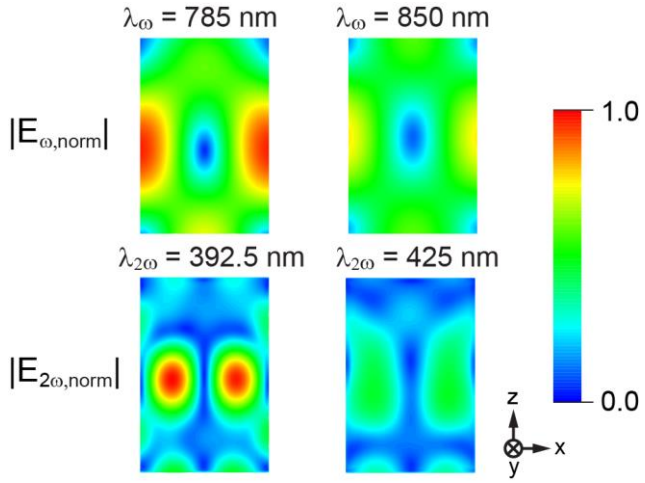

Figure 10. Calculated field distributions for both the fundamental and the second harmonic waves. The field maps are produced at the fundamental wavelengths of 785 nm and 850 nm, respectively, which represent the cases with and without the magnetic Mie resonance mode. Strong second harmonic generation is observed under the on-resonance excitation (i.e., λ_{ω} = 785 nm).

For these calculations, the third-order nonlinear susceptibility of bulk silicon ($\chi_{\mathrm{Si}}^{(3)} \approx 2.8 \times 10^{-18}$ m^2/V^2) is used (*14*), and a uniform static electric field along the y-direction ($E_y^0 = 2 \times 10^5$ V/m) inside the silicon strips is assumed. Considering both the elements of the $\chi_{\mathrm{Si}}^{(3)}$ susceptibility tensor of silicon and all involved electric field components inside the silicon structure, only two effective terms may contribute to the EFISH generation under the TM illumination: $\chi_{yxxy}^{(3)} E_x^{\omega} E_x^{\omega} E_y^0$ and $\chi_{yzzy}^{(3)} E_z^{\omega} E_z^{\omega} E_y^0$ (see Supporting Information for details). Note that in the expression of the $\chi^{(3)}$ elements, the last subscript index has been reserved for the applied dc field in our case. The numerical data shows that strong output of the frequency doubled signal is generated at $\lambda_{2\omega}$ = 392.5 nm, while substantially weaker signals are observed when the structure is excited off-resonance (e.g.,

at λ_ω = 850 nm and $\lambda_{2\omega}$ = 425 nm). These numerical tests have revealed the significant impact of the magnetic Mie resonance on achievable EFISH strength.

The EFISH generation from the silicon metasurfaces, along with its resonant characteristics and electrical tunability, have been experimentally explored. Figure 4b shows the voltage induced a change in the intensity of the second-harmonic signal $\Delta I_{2\omega}(V)$, normalized to the SHG level in the unbiased case at the fundamental wavelength of 750 nm (I_0), at a series of voltages from 0 to 10V. Moreover, to further illuminate the importance of magnetic Mie resonance for the EFISH generation process, we have characterized the device under both the TM- and the TE-polarized fundamental lights. As illustrated in Figure 4b, under the TM excitation that supports a magnetic Mie resonance, the EFISH signal grows monotonically as the voltage is increased. In stark contrast, with the TE-polarized fundamental light, a negligible variation of the SHG level is observed as no magnetic Mie mode is present in this case.

The voltage dependence of the EFISH generation observed in Figure 11a can be explained based on the expression of the overall SHG intensity:

$$\begin{aligned} I_{2\omega}^{\mathrm{tot}} \propto |P_{2\omega}^{\mathrm{tot}}|^2 \propto \left|\left(\chi_{\mathrm{tot}}^{(3)} E_y^0 + \chi_{\mathrm{surf}}^{(2)}\right) E_\omega^2\right|^2 \\ = \left\{\left[\chi_{\mathrm{tot}}^{(3)} E_y^0\right]^2 + \left[2\chi_{\mathrm{tot}}^{(3)} \chi_{\mathrm{surf}}^{(2)} E_y^0\right]\right\} E_\omega^4 + \left(\chi_{\mathrm{surf}}^{(2)}\right)^2 E_\omega^4 \end{aligned} \tag{17}$$

where E_y^0 represents the applied static field along the y-direction, $\chi_{\mathrm{tot}}^{(3)}$ is the total third-order susceptibility, and $\chi_{\mathrm{surf}}^{(2)}$ denotes the second-order nonlinear susceptibility from the silicon surface. On the right-hand side of Eq.17, the first term consisting of two parts with

E_y^0 describes the EFISH generation enabled by an applied voltage, and the last term corresponds to the static SHG response stemmed from surfaces. Therefore, the magnitude of the EFISH generation would grow with the level of the static field E_y^0 (and thusly the applied voltage), with an exponential factor between 1 and 2 as observed in Figure 11a. In addition, the EFISH expression shows that the efficiency of the EFISH generation scales with the E_ω^4 term, where the strong field confinement enabled by the Mie resonance in the silicon strips further contributes to the field-induced generation of the second-harmonic signal.

The EFISH generation and its voltage-induced tunability are examined at various fundamental wavelengths around the magnetic Mie mode, as depicted in Figure 11b. The frequency doubled signal at each measurement point is normalized to the SHG intensity at the fundamental wavelength of 750 nm without an applied voltage. These results reveal that noticeable control over the EFISH generation can be performed only when the metasurface possesses both an applied static field and a strong magnetic Mie resonance. The presented set of experimental and numerical findings have confirmed the significant role of the magnetic Mie resonance on controlling the EFISH generation in silicon micro- and nanostructures.

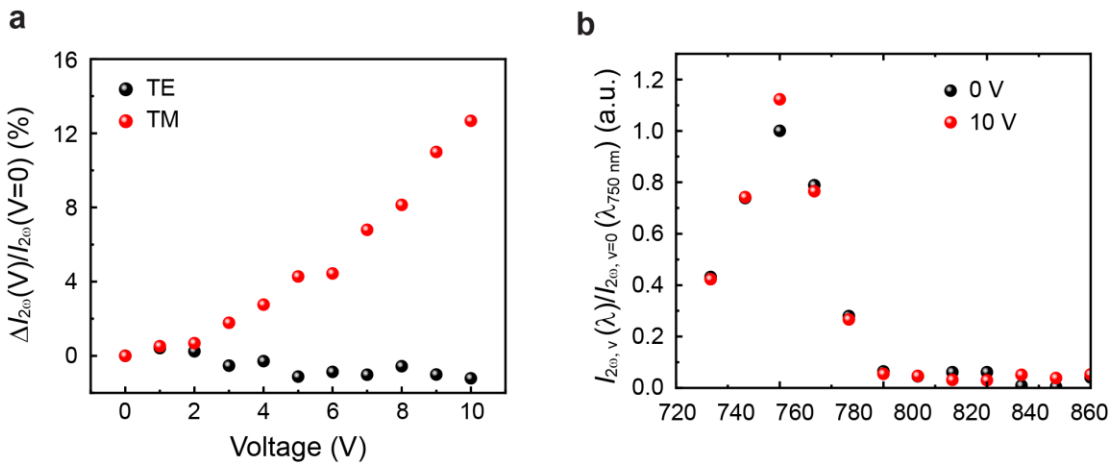

Figure 11. Experimental results for the electrically induced nonlinear optical response. (a) Characterization of the dependence of normalized change in the frequency doubled intensity on the applied voltage, when the sample is excited with the TM- (red dots) and TE- (black dots) polarized fundamental wave at the wavelength of 750 nm. Pronounced EFISH generation is observed under the TM polarized excitation, which is capable of inducing the magnetic Mie resonance mode in the silicon metasurfaces. (b) The wavelength dependence of SHG generation with (red, 10 V bias) and without (black) applied voltage. The intensity of the harmonic signal is normalized to the SHG value at the fundamental wavelength of 750 nm with no bias.

2.5 Summary

To summarize, we have demonstrated electrically-enabled second-harmonic generation of light in single crystalline silicon structures, where the intrinsic inversion symmetry in the crystal lattice prohibits optical nonlinearities of the second-order type. Our experiments reveal that the application of a static electric field transduces the large third-order susceptibility of silicon into an effective $\chi^{(2)}$ process that facilitates the generation of frequency-doubled signals via the EFISH process. To circumvent the need for a high static field, we engineered crystalline silicon into rationally designed metasurfaces that provide a strong light concentration in the spectral vicinity of the magnetic Mie resonance.

The polarization sensitivity of the structure for the excitation of the magnetic modes offers an extra degree of freedom to control nonlinear interactions of light with the devised metasurfaces. The outcome of this study suggests that by exploiting magnetic Mie resonances in electrically enabled metasurfaces, silicon can be envisioned for photonic platforms with actively controlled light properties through second-order nonlinear processes.

2.6 Methods

Device fabrication: The silicon devices for this experiment are fabricated by a three-step process. First, a standard electron beam lithography (E-beam litho., Elionix ELS-G100 EBL system) using the HSQ (XR-1541) as a negative e-beam resist is performed. After the exposure, the resist turns into SiO_2 so that it can serve as a hard mask for the etching process. Second, the SOI wafer with the hard mask is etched by chlorine gas in the ICP-RIE (Plasma-Therm) equipment and the hard mask removal is followed by using buffered oxide etchant for 2 seconds. Third, a standard metal electrode (Cr / Au) is formed by photolithography (Karl Suss Mask Aligner) and metal evaporation (CHA Industries, Inc.) followed by the lift-off process. The more detailed processes with a flow chart are described at the supporting information.

Linear optical characterization: Tungsten halogen lamp (B&W Tek BPS 120) is used as a broadband light source to characterize the linear response of the device. The input polarization of the source is controlled by a set of linear polarizers and half waveplates. The analysis is performed in reflection mode where the objective lens (Mitutoyo, 20X plan

Apo NIR infinity-corrected) focus light onto the sample and collect the reflected light from the sample using the same objective lens. The light collected by the objective is delivered to the spectroscopy system (Princeton Instrument Acton SP 2300i with PIXIS 400B camera). The reflectance of each sample is normalized to the reflection from the plane gold electrode.

Nonlinear optical characterization: Both the SHG and EFISH characterization is done by using a homemade microscope type measurement system. The fundamental wave is generated from a tunable Ti: Sapphire ultrafast oscillator (Spectra-Physics, Mai Tai HP, 690~1040 nm) with 100-femtosecond pulse duration and 80 MHz repetition rate. Power and the polarization state are controlled by a set of halfwave plate and Glan polarizer. The fundamental wave is focused by the objective lens (20X, Nikon) and both the reflected and the harmonic generated light from the sample are collected by the same objective lens. The fundamental wave is eliminated as it passes through the bandpass filter and only the generated signal from the sample is characterized by the detector system which is composed of a monochromator (Princeton Instruments, IsoPlane) with CCD camera (Princeton Instruments, Pixis 400B). The generated signal is collected with/without applying voltage so that the effect of static field induced SHG signal can be analyzed by further data processing. The more details with the schematics of the optical setup can be found in the Supporting information.

2.7 Supporting Information

Supplementary Note 1. Detailed Fabrication process

The fabrication flowchart is illustrated in Figure 12. (a) The silicon metasurfaces are fabricated on the silicon on insulator (SOI) wafer (Solitec). The SOI wafer is composed of 190 nm of (100) silicon on top of 150 nm of SiO_2 layer. (b) A 115 nm of negative e-beam resist (XR-1541, 6% HSQ) is formed on top of the SOI wafer by spin coating the resist at 3200 RPM for 60 seconds with ramp time of 2 seconds followed by a pre-baking process at 80 °C for 4 min. The resist is selected to form a hard mask to etch the top silicon layer, as it turns into silicon dioxide after the full EBL process is performed. (c) Next, electron beam lithography (Elionix ELS-G100 EBL system) is carried out to define the geometry of the silicon metasurface. In this step, the alignment marks are also defined, which is necessary for the photolithography process. After the EBL exposure, the resist is developed in 25% Tetramethylammonium hydroxide (TMAH) solution for 30 s under 80 °C and rinsed gently by deionized water to reduce residue. Then the remaining e-beam resist structure turns into silicon dioxide which can serve as a hard mask during the etching process (d) The exposed area of the single crystalline silicon layer is etched by inductively coupled plasma - reactive ion etching (ICP-RIE) technique using the chlorine (Cl_2) gas. The etch rate of the silicon is measured as ~12 Å/s, where the etch selectivity between the Si and HSQ hard mask is 4 to 1. By controlling the pressure, coil and platen power, we could achieve a vertical sidewall of the silicon strips. (e) Hard mask (HSQ) is removed by dipping the sample into the buffered oxide etchant (6:1) for 1~2 seconds and quickly rinsed by DI water. This step is conducted carefully and precisely to prevent etching the buried SiO_2 layer in the SOI wafer during the process. (f) Next, standard photolithography technique is conducted to define the electrodes. Positive photoresist (SC1813) of 1.7 μm in thickness is spin-coated at 3000 RPM with ramp time of 2 seconds for 60 seconds and

it is prebaked at 115 °C for 50 seconds. Then the photoresist layer was exposed (Karl Suss mask aligner) and developed by Microposit MF-319 (MicroChem) developer. (g) Afterwards, 100 Å and 2500 Å thick Cr and Au layer is deposited by using e-beam evaporator (CHA Industries, Inc.), respectively, where the deposition rate for the both processes is fixed at 0.5 Å/s. (h) Subsequently, a lift-off process using the Acetone solution is carried out to form a metal electrode for the silicon metasurfaces. (i) and (j) show the top and side views of the fabricated device, respectively. It shows that the silicon gratings are well covered by the top gold electrode layer.

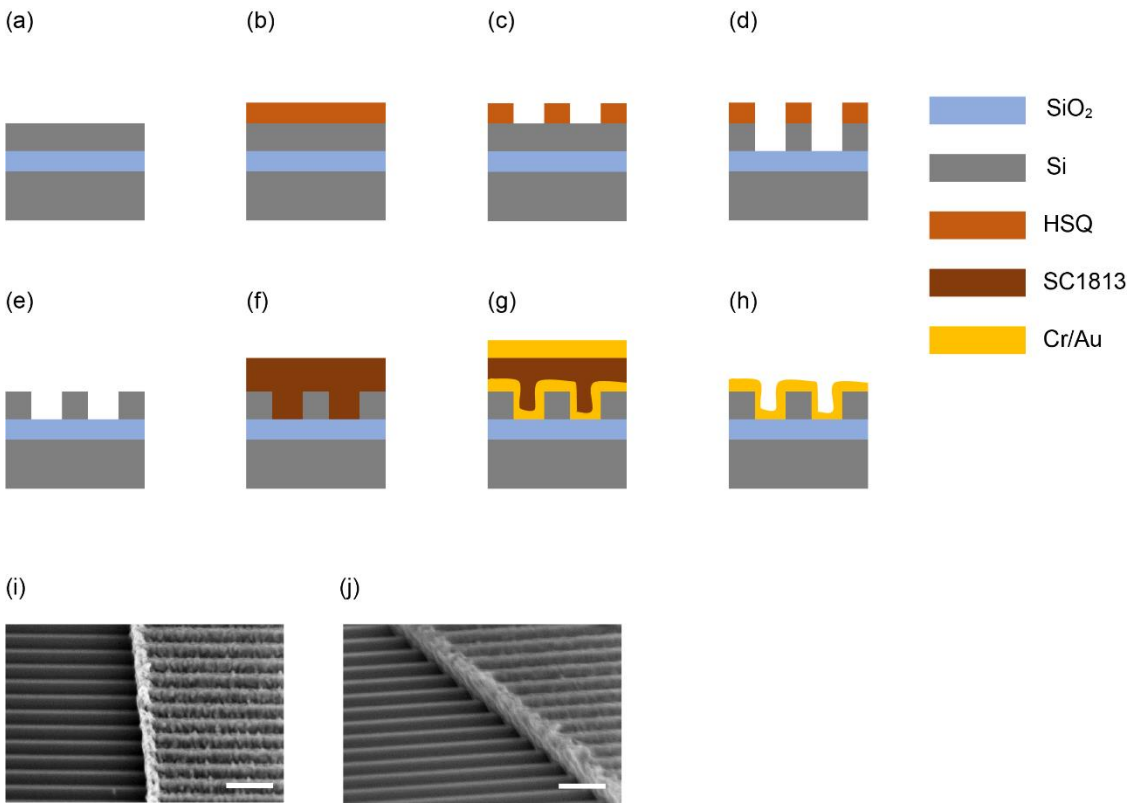

Figure 12. Fabrication flowchart of the Si metasurfaces with electric contacts. The scale bars represent 500 nm.

Supplementary Note 2. Nonlinear optical characterization

A schematic of the home-mad experimental setup for nonlinear optical characterization is shown in Figure 13a. The fundamental wave is generated from a tunable Ti: Sapphire ultrafast oscillator (Spectra-Physics, Mai Tai HP, 690~1040 nm) with 100 femtosecond pulse duration and 80 MHz repetition rate. The power and the polarization states of the incident light are controlled by the set of halfwave plates and the Glan polarizer. The fundamental light passes through the beam splitter and focused on the sample by the objective lens (20x, NA =0.5). Both the fundamental and harmonic generated signals are collected by the objective and reflected by a beam splitter. The bandpass filter eliminates the fundamental wave so that only generated signal could be characterized by the detection system which is consists of a monochromator (Princeton Instruments, IsoPlane) with CCD camera (Princeton Instruments, Pixis 400B). The generated signal is collected with/without biasing the sample which the effect of static field induced SHG signal is analyzed by further data processing.

The focused beam has a spot size of 20 ~ 40 μm depending on the intensity of the incident beam so that it could excite the silicon gratings while minimizing the nonlinear effect from the gold electrode. Though the beam size is smaller than the width of the exposed silicon grating area, the comparison of acquired spectra of the SHG signals between the gold pad and the device is performed to further elucidate the effect of the SHG signal from the gold electrode on the total SHG signal from the device S3 (see Figure 13b). For the measurement, TM-polarized laser pulses of varying fundamental wavelengths from 720 to 900 nm are used to excite the pad and device at a constant intensity. As shown in Figure S3b, the SHG signal acquired from the gold pad was negligible compared to the SHG signal observed from the silicon grating, from which we can safely assume that the signal from the gold pad can be ignored.

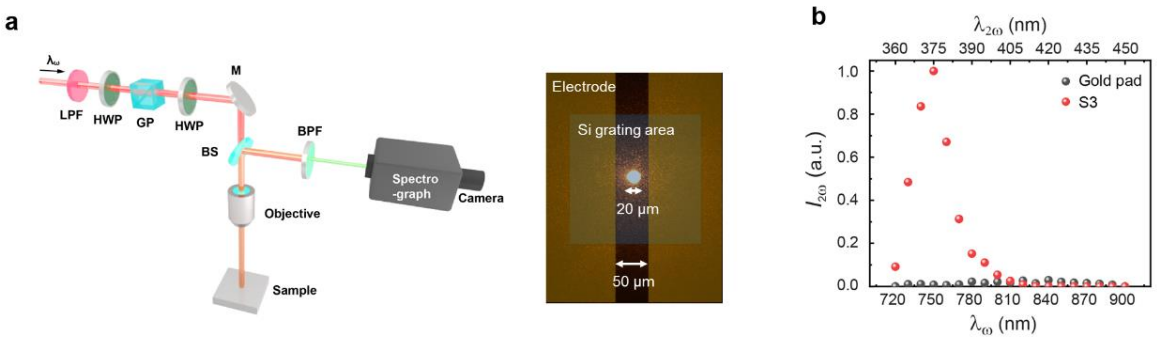

Figure 13. (a) Experimental setup for characterizing SHG / EFISH signal from the device. Abbreviation for optical components: LPF: long-pass filter; HWP: half waveplate; GP: Glan-Polarizer; M: mirror; BS: Beam splitter; BPF: band-pass filter. (b) Comparison of the second harmonic signal from the gold pad and device S3 at a series of excitation wavelengths of a constant intensity.

Supplementary Note 3. Polarized excitation analysis

Figure 14a illustrates the polarization survey of the S3 device to investigate the behavior of the magnetic Mie resonance due to the polarization of the illuminating light. The input polarization of the light is controlled by the halfwave plate as described above in the “Linear optical characterization” section. At the expected spectral location of the magnetic Mie resonance, at 750 nm, the TE polarized light exhibits lower reflectance than the TM polarized light. However, the cross-sectional view of the calculated field profile inside the silicon strips of the S3 device shows a stronger field is confined in the silicon stripes under TM polarization excitation as shown in Figure 14b. This is because the silicon stripes experience a strong coupling with TM polarized light and form a circulating electric field in the grating. This indicates that the magnetic Mie resonance is the source of the strong field enhancement in the silicon stripes which is dependent on the polarization of the incident light.

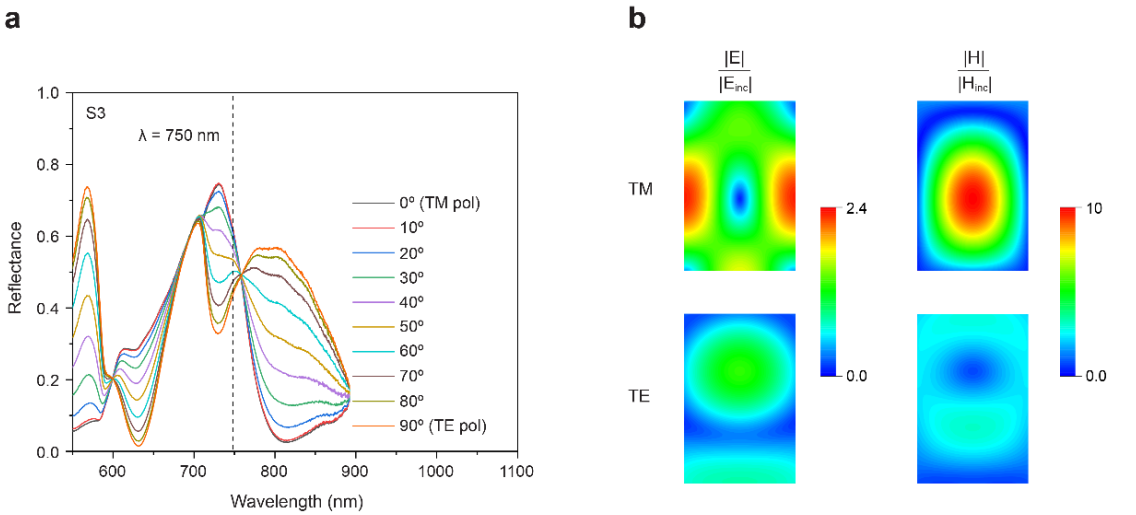

Figure 14. (a) Linear optical response of the S3 device obtained by varying the polarization of the incident light. (b) Calculated Cross-sectional views of the normalized electric and magnetic field distributions for the TE / TM polarization excitation at the wavelength 785 nm. Strong field confinement is shown only under the TM polarization, which is induced by the magnetic Mie resonance.

Supplementary Note 4. Estimation of static SHG enhancement

Calculation of the static SHG is executed by incorporating the surface $\chi^{(2)}$ tensor of the (100) crystalline silicon (*15, 48*) and field enhancement originating from the magnetic Mie resonance. The bulk contribution to the SHG signal due to the high order multipoles, i.e., magnetic dipoles or electric quadrupoles, is neglected in this calculation due to its small contribution to the overall SHG intensity from the silicon structure (*51*).

As the devices are fabricated simultaneously on the same SOI wafer, the azimuthal dependency of the SHG output from the (100) silicon surface is ignored to simplify the calculation. From the cross-sectional view of the electric field vector profile in Figure 15, the silicon strips under the TM-polarized fundamental wavelength of 785 nm can possess electric field in both x and z directions, while the planar Si pad device possess electric field

in only the x direction. Moreover, the electric field inside the strips is strongly confined so that it could further enhance the SHG signal from the grating surfaces.

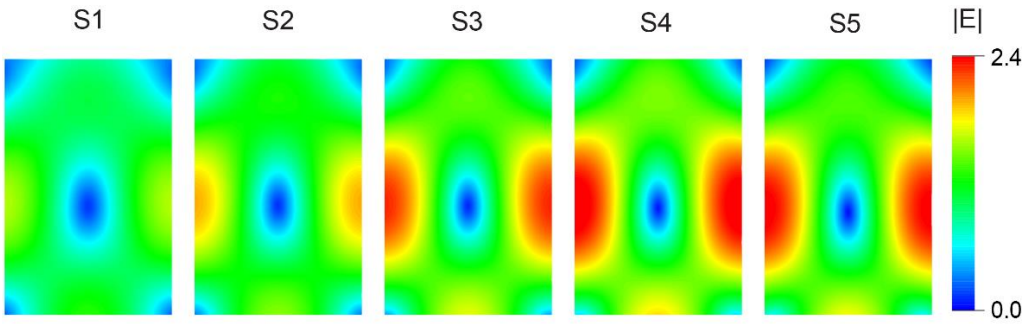

Figure 15. Electric field profile from the five devices at the TM polarized wavelength of 785 nm

Therefore, the contribution of the surface $\chi^{(2)}$ tensor can be analyzed based on the two cases: second harmonic signal generates 1) only from the x-component and 2) from both x- and z-components of the electric field. By combining the nonlinear polarization tensor of the silicon surface, $P^{NL,\mathrm{surf}}$, with the two cases, the total nonlinear polarization which contributes to the SHG signals of each case are derived as shown in Eq.16.

The first case corresponds to the plane silicon sample, S6, where the second case describes the SHG behavior at the silicon metasurfaces. The value for d_{15}, d_{31}, and d_{33} can be determined by a frequency-domain interferometric second harmonic generation technique (*50*). In this calculation, the d_{ij} values are assumed to be positive and real so that $d_{15} \sim 10^{-19}$, $d_{31} \sim 10^{-21}$, and $d_{33} \sim 10^{-18}$ m^2/V are estimated at the fundamental wavelength of 745 nm. By assigning the d_{ij} values to Eq. 7, we could find the significant role of E_z components in the total nonlinear polarization as the magnitude of d_{31} is negligible compare to the other two terms.

Next, we calculated the total field enhancement in the silicon metasurfaces, by combining two factors from the field enhancement in a single silicon rod due to the magnetic Mie resonance and the filling ratio of the silicon strips at the silicon metasurfaces. The filling ratio (FR) is defined by dividing the width of the grating (130 nm) to its periodicity (S1: 280 nm, S2: 330 nm, S3: 380 nm, S4: 430 nm, S5: 480 nm). Then the field enhancement and the nonlinear polarization is incorporated to estimate the SHG enhancement from the given silicon metasurfaces. Since the E_z term at the surface of the silicon metasurfaces governs the total nonlinear polarization, only the electric field in z-direction at the surface of the grating is used for the SHG enhancement calculation. Figure S5 illustrates the cross-sectional view of the electric field profile of the proposed five metasurface device under TM polarized incidence at the fundamental wavelength of 785 nm and Table 1 illustrates the estimated SHG enhancement results from the contribution of E_z field. High SHG enhancement is shown at the device S3 and S4 regardless of its low filling factors compare to S1 and S2. To explore the nonlinear response clearly at the spectral vicinity of the magnetic Mie resonance, the sample S3 is chosen whose magnetic Mie mode is spectrally distant from the reflection peak.

Table 1. SHG enhancement estimation based on the E_z enhancement at the surface

	P [nm]	**FR**	**E_z^2 enhancement**	**SHG enhancement (d_{33})**
S1	280	0.46	2.79	1.67
S2	330	0.39	4.21	2.75
S3	380	0.34	5.67	3.77
S4	430	0.30	6.44	3.79
S5	480	0.27	5.72	2.40

Supplementary Note 5. Numerical calculation of the EFISH generation

EFISH generation from the device S3 is calculated numerically by combining the field profile at the fundamental wavelength λ_ω, the static field induced by the external voltage, and the third-order susceptibility tensor ($\chi^{(3)}$). As shown in Figure S4b, the field distribution in the silicon nano-stripes exhibits a strong dependence on the polarization of the incident light. When the silicon nanograting is excited by the TM polarized light, the structure could couple with the incoming wave which induces a circulating electric field inside the grating. This magnetic Mie mode indicates that the x- and z- components of the electric field dominate in the grating. On the other hand, the field profile shows that the field coupling between the silicon gratings and the TE polarized incident light is negligible compared to the TM polarized case.

Crystalline silicon belongs to the m3m symmetry group, where the third-order susceptibility tensor ($\chi^{(3)}$) possesses 21 nonzero elements. Among the nonzero elements, only 4 are independent as shown below (*14*):

$$\begin{aligned} &xxxx = yyyy = zzzz, \\ &yyzz = zzyy = zzxx = xxzz = xxyy = yyxx, \\ &yzyz = zyzy = zxzx = xzxz = xyxy = yxyx \\ &yzzy = zyyz = zxxz = xzzx = xzzx = xyyx = yxxy \end{aligned} \tag{18}$$

As the static electric field induced by the external voltage forms the electric field along the silicon gratings (E_y^0) and the dominant electric field direction induced by the magnetic Mie

resonance are in the x- and z-direction, only two effective terms could contribute to the EFISH generation: $\chi^{(3)}_{yxxy}E^{\omega}_{x}E^{\omega}_{x}E^{0}_{y}$ and $\chi^{(3)}_{yzzy}E^{\omega}_{z}E^{\omega}_{z}E^{0}_{y}$.

Using the two effective terms as a source for the EFISH generation in the silicon gratings, a nonlinear response at device S3 is calculated. Figure 16 shows the EFISH generated signal for both TE / TM polarized incident fundament light. The result clearly shows that the TM polarized light could produce the second-order signal effectively, thanks to the field localization and enhancement facilitated by the strong magnetic Mie resonance.

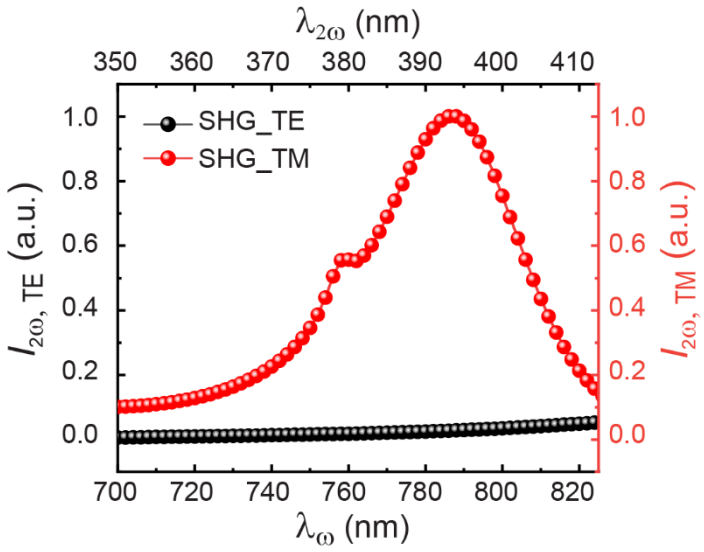

Figure 16. Numerical results for the EFISH generation from the S3 device for TE / TM polarized fundamental light.

Supplementary Note 1. Output polarization analysis of the EFISH signals

Figure 10 shows the calculated and experimental results of EFISH generation from the S3 device. As described in the manuscript two effective terms, $\chi^{(3)}_{yxxy}E^0_y$ and $\chi^{(3)}_{yzzy}E^0_y$, are derived by incorporating the third-order nonlinear susceptibility tensor of single crystalline silicon and all involved electric field components in the silicon structure. The EFISH generation results exhibit in Figure 10a,b clearly shows that the SHG signal is generated along the silicon strips. Therefore, the EFISH generated signal is expected to possess polarization in the y-direction. Figure 17 shows the experimental results of the output polarization of second-order nonlinear signal in the device S3. The intensity of the y-polarization from the voltage induced SHG (red dot) is shown to have higher value compared to the surface SHG (black dot) which indicates that the polarization of the EFISH generated signal contains a y-direction polarization.

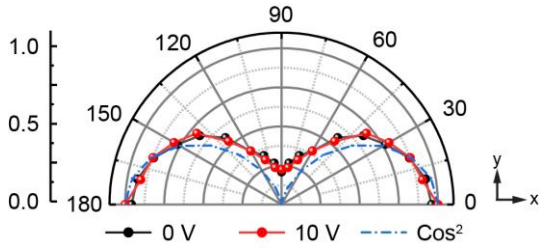

Figure 17. Output polarization of SHG signal with / without applying the voltage at the S3 device.

CHAPTER 3. PHOTOCHEMICAL SWITCHING VIA PLASMONICALLY ENHANCED UPCONVERSION PHOTOLUMINESCENCE

Over recent years, photochromic materials have received considerable attention for application in a variety of electronic, spectroscopic, and photonic systems (*52, 53*). Due to their appealing properties of moderate response time, high photoisomerization quantum yield, and notable photobleaching resistance, diarylethene-based photochromic molecules have been widely used for molecular photoswitching (*53-56*). However, they typically require a dual illumination source, such as short-wavelength ultraviolet (UV) light for initiating photoisomerization and visible (VIS) wavelength light for reversible molecular isomerization. One solution is to associate lanthanide-doped upconversion nanoparticles (UCNPs) with photochromic molecules (*57-59*). This combination is typically used to control photoisomerization reactions, making it appropriate for application in near-infrared (NIR)-triggered photoswitchable systems (*60-63*). With an assortment of dissimilar materials, the UCNPs absorb two or more photons in the NIR region and produce photons with shorter wavelengths (e.g., UV or VIS). Subsequently, photoisomerization of the photochromic molecules is triggered by reabsorption of photons emitted from UCNPs. Despite these attractive prospects, UCNPs possess fundamental limitations, including low quantum efficiency and low absorption efficiency, which prevent their use in facilitating photoisomerization reactions (*64-68*). Moreover, these inherent constraints could reduce both photochromic responsiveness and photochemical stability during fabrication into solid films for versatile optical applications. Consequently, these constraints require novel

approaches for improving the magnitude of upconversion photoluminescence (UCPL) and embracing the duplex-trigger wavelengths corresponding to the UV and Vis regions.

To improve the performance of the UCPL, UCNPs have been incorporated with the surface plasmon resonances that arise from the nanosized metallic structures (*69, 70*). In particular, metal–insulator–metal (MIM) configurations provide strong electric field confinement in the dielectric region due to the gap plasmon resonance mode (*71-73*). By tailoring the spectral response of the resonance mode at the NIR and/or VIS region, the MIM structures efficiently improve the UCPL (*20, 74-76*). Although previous inspirational studies have reported improvements in UCPL, its enhancement is mainly restricted to emission in the Vis region, such as green and red (*20, 69, 74-76*). Thus, control of photochromic isomerization is hindered due to lack of UCPL in the UV region. Furthermore, to control the isomerization reaction, orthogonality between UV and VIS emissions from the UCPL corresponding to NIR stimuli is simultaneously needed. Consequently, an innovative strategy is required to excite the resonance mode over the broadband wavelength between the UV and VIS regions.

In this study, we propose a versatile plasmonic platform of quasi-periodic arrays that exhibits an efficient photocyclization reaction by deriving fine-tuned resonance mode from UV to NIR regions. To realize photoswitchability in plasmonic platforms, multilayer $NaYF_4$:Yb^{3+}/Tm^{3+}@β-$NaYF_4$:Yb^{3+}/Er^{3+}@β-$NaYF_4$ UCNPs with different emission ranges from UV (346 nm) to Vis red (657 nm) based on excitation power intensity were employed. The synthesized UCNPs were incorporated in a dielectric SiO_2 layer that serves as an insulator layer in the MIM structure, where quasi-periodic arrays of silver (Ag) nanopatterns were precisely fabricated via the double metal-transfer technique.

Subsequently, the disulfonyldiarylethene (DTE) derivative-doped SiO_2 was placed on the prepared nanopatterns. Remarkable UCPL enhancement factors (EFs) of at least two orders of magnitude were observed by the plasmonic-enhanced photoswitchable platform at broadband emission ranges from UV to VIS. The broadband photoluminescence (PL) enhancement stemmed from the diverse plasmon resonance modes, which were induced by quasi-periodic arrays. Furthermore, the photocyclization reaction was increased threefold by the enhanced UCPL compared to the reference device, while maintaining photobleaching resistance and photocyclization stability. Our study shows the highly efficient two-way photoisomerization of DTE derivatives, which are regulated by incident single-wavelength NIR modulation and UV/VIS irradiation. Combined with improved optical performance, this facile fabrication methodology for large-scale production of a fast-response photoisomerization system provides an innovative alternative for various feasible applications, such as optically switchable electronic devices, enzyme/inhibitor mimicking, and standard methods of super-resolution PL imaging (*53, 77-83*).

3.1 Photochemical plasmonic-platform structure

To achieve NIR-triggered photoisomerization of the photochromic materials, we first prepared photoswitchable UCNPs that could produce distinctive orthogonal PL under high (588 W/cm^2) and low power (31 W/cm^2) irradiations of 980 nm wavelength NIR. As shown in Figure 18, the photoswitchable UCNPs comprised a core and multiple shells, including a luminescent core (LC), an inner luminescent shell (LS), and an outer inert shell, through sequential epitaxial growth (*60*). The hexagonal β-phase $NaYF_4$ was used as a host matrix due to its low lattice phonon energy (*84*). The LC and LS were doped with Tm^{3+} or Er^{3+} ions as activators, respectively, and Yb^{3+} was co-doped with each activator as a sensitizer

for efficient upconversion. The LC/LS core-shell structure was wrapped with pure $NaYF_4$ to minimize energy dissipation loss outside of the particles (*85*). The optical characterizations of UCNPs were examined under both high- and low-power irradiation at the wavelength of 980 nm.

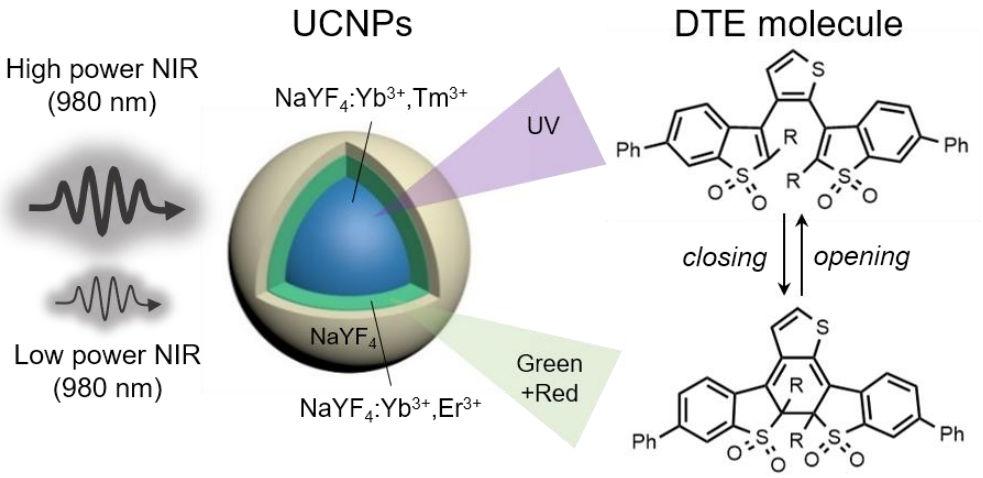

Figure 18. Schematic of the photoswitching system facilitated by core–shell–shell UCNPs. The reversible photoisomerization reactions of the DTE molecules (R = Methyl or Ethyl) were driven by UV/Vis UCPL.

As shown in Figure 19a, the peaks of the UCPL under high-power irradiation at 980 nm (588 W/cm^2) were located at wavelengths of 346 nm ($^1I_6 \rightarrow {}^3F_4$), 452 nm ($^1D_2 \rightarrow {}^3H_6$), 545 nm ($^4S_{3/2} \rightarrow {}^4I_{15/2}$), and 657 nm ($^4F_{9/2} \rightarrow {}^4I_{15/2}$), corresponding to the major emissive transitions in the Tm^{3+} and Er^{3+} states. On the other hand, Figure 19b illustrates the UCPL under the low pumped-power 980 nm excitation (31 W/cm^2), where the peaks at 545 nm and 657 nm correspond to emission transitions in the Er^{3+} state (Figure S3). These orthogonal emission characteristics according to irradiation power imply applicability to trigger reversible photoisomerization through strong UV emission at high-power 980 nm excitation or pure VIS emission at low-power 980 nm excitation.

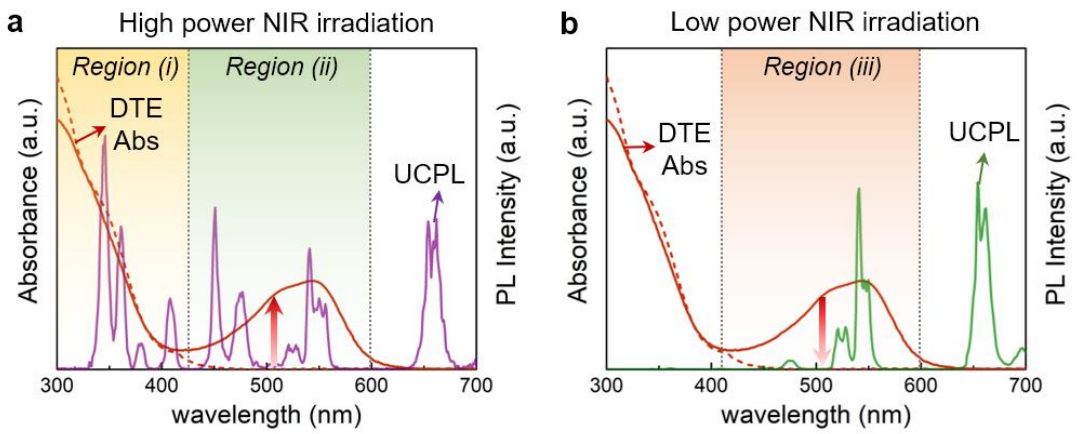

Figure 19. Absorbance and PL spectra under NIR irradiation. The red dashed and solid lines indicate absorbance of ring-opened and ring-closed structures of 2 DTE derivatives, respectively. (b) The UV UCPL under high-power 980 nm irradiation activated the ring-closing reaction of the 2 DTE derivatives in region (i). The green UCPL under high-power 980 nm irradiation excited the PL of the 2 DTE derivatives in region (ii). (c) The green UCPL under low-power 980 nm irradiation triggered the ring-opening reaction of the 2 DTE derivatives.

Moreover, considering the spectral match with the switchable PL wavelength of the UCNPs, we synthesized the new DTE derivatives **1** (R = Methyl) and **2** (R = Ethyl) in accordance with the procedures in Figure 20. In this experiment, the diarylethene **7** was synthesized using Suzuki coupling reaction, and selective oxidation of **7** with meta-chloroperoxybenzoic acid (mCPBA) afforded **1** and **2** in 38% and 42% yields, respectively (see Supplementary Method for details). The synthesized DTE derivatives in Figure 1a were adequately photocyclized under UV irradiation, leading to absorption increase in the visible region and exhibiting PL of the ring-closed derivatives at the wavelength of 600 nm (see Figure S5). Along with the spectral changes, the DTE derivatives showed compatible intrinsic characteristics (*e.g.,* photoisomerization conversion efficiency and PL quantum yield) to previous studies (**Table 2**) (*86, 87*).

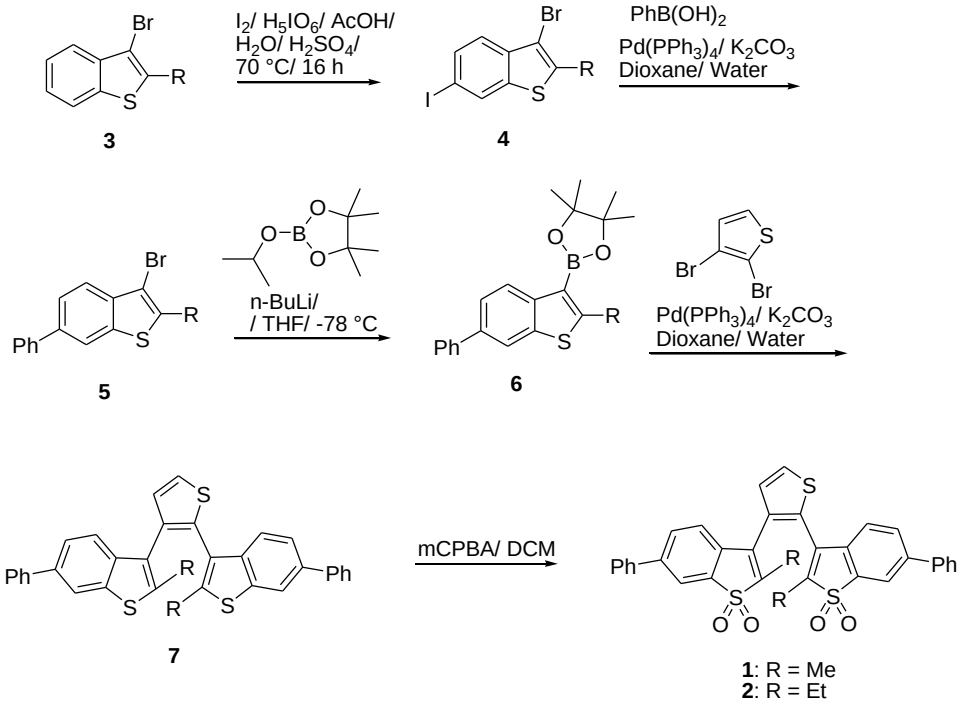

Figure 20. Syntheses of disulfonyldiarylethenes 1 and 2. The major intermediate compound 5 were synthesized in 48 % (R=Methyl) and 29 % (R=Ethyl) yield from 3, respectively.

Table 2. Optical characteristics of DTE molecules.

	$\varepsilon_{abs}(10^4\ M^{-1}m^{-1})$	φ_{PL}	$\varphi_{o\rightarrow c}$	$\varphi_{c\rightarrow o}$	**Ref.**
1 DTE	2.8	0.015	0.81	~1.00	In this study
2 DTE	3.4	0.028	0.62	~1.00	In this study
1 a	2.1	0.036	0.40	0.055	(*88*)
2 a	1.0	0.19	0.23	0.38	(*88*)
1 b	-	0.034	0.73	-	(*86*)
2 b	-	0.0001	0.91	-	(*86*)
1 c	0.79	0.07	0.14	3.5×10^{-5}	(*89*)

Table 2 continued.

2 c	0.83	0.5	0.12	2.1×10^{-3}	(*89*)
1 d	1.9	0.87	0.62	5.9×10^{-4}	(*90*)
2 d	0.97	0.79	0.59	1.8×10^{-2}	(*90*)
1 e	-	0.004	0.36	0.06	(*91*)
2 e	-	0.06	0.24	0.25	(*91*)
BTTE	0.68	0.008	0.26	0.07	(*92*)
BTF6	1.6	-	0.31	0.28	(*93*)

All absorption peaks of the ring-opened DTE were located below 380 nm and spectrally overlapped the UV emission of UCPL (Figure 19a). In addition to the absorption peaks at the UV region, the ring-closed DTE displayed one additional peak near 545 nm wavelength, which matched the green emission of UCPL. In particular, as described in Figure 1b, the UV emission (region (i)) of the UCPL at high-power excitation facilitated photocyclization of the ring-opened DTE toward the ring-closed DTE, and the Vis emission (region (ii)) of the UCPL effectively functioned as a PL excitation source for the ring-closed DTE. Due to significantly higher photoisomerization quantum yield (QY) of the DTE derivatives in the UV region than in the green region, the co-emitted VIS UCPL in the region (ii) did not impede the ring-closing reaction of the DTE. As shown in Figure 19b, on the other hand, UCPL exhibited only green and red emissions when subjected to low-power irradiation. Therefore, the pure VIS UCPL in region (iii) guided the ring-

opening reaction of the DTE molecule, resulting in reversible photoisomerization via regulation of the intensity of incident NIR power.

Despite efforts to utilize UCPL as a substituted light source, efficient photoisomerization of the DTE derivatives was impeded by both the low quantum efficiency of UCNPs and the difficulty of obtaining coherent results on a large scale. Therefore, to mitigate the restrictions and improve photoswitching performance, this study investigated a plasmonic platform comprised of a metallic nanostructure-insulated layer-metal reflector platform (see Figure 21). In this platform, the prepared UCNPs were embedded in an insulate layer (SiO_2) as shown in the inset of Figure 21. To reduce PL quenching due to direct contact between the metal layers and UCNPs, UCNPs were separated from the top and bottom Ag layers (*94*). Finally, the DTE film was placed on the Ag nanostructures to harness the light-management benefits of the proposed plasmonic platform.

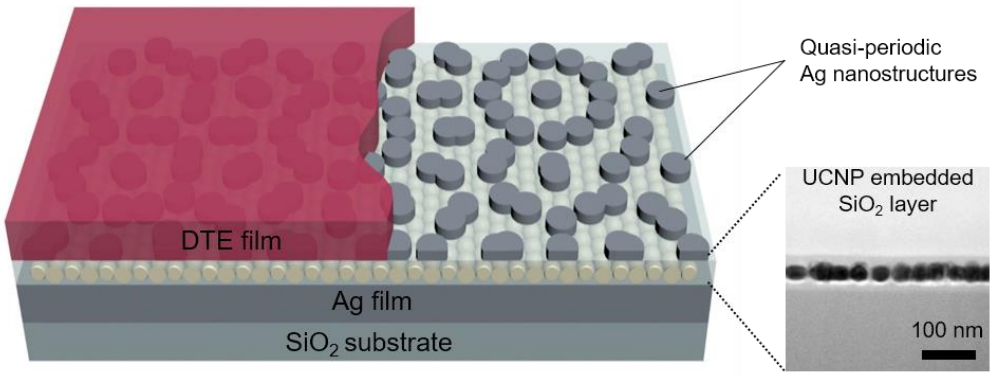

Figure 21. Schematic of the DTE-incorporated quasi-periodic plasmonic platform and the cross-sectional TEM image of the UCNP-embedded SiO2 layer.

3.2 Design and fabrication of the quasi-periodic plasmonic platform

To realize facile fabrication of a quasi-periodic lattice MIM platform, the metal-contact nanolithography technique was utilized via a perfluoropolyether (PFPE) stamp with a large area for nanoscale features (Figure 22a) (*71, 95*). Herein, an Ag reflector (100 nm) was deposited on a quartz substrate, and the synthesized UCNPs (β-$NaYF_4$:Yb^{3+}/Tm^{3+}@β-$NaYF_4$:Yb^{3+}/Er^{3+}@β-$NaYF_4$ nanoparticles) in a perhydropolysilazane (PHPS) SiO_2 precursor solution was spun-cast onto the Ag reflector substrate to form the UCNP-embedded SiO_2 layer. To fabricate the Ag nanopattern, a 35-nm Ag layer was deposited on the nanopatterned PFPE stamp. Then, the Ag nanopatterns were transferred from the stamp onto the UCNP-embedded SiO_2 (70 nm) layer via contact under precisely controlled temperature, pressure, alignment, and polymerization duration (refer to the detailed conditions in the experimental section). These procedures facilitated construction of a hexagonal array of periodic Ag nanostructures (200 nm in diameter and 400 nm in pitch) on the UCNP-embedded SiO_2/Ag substrate. Subsequently, an identical metal-transfer process was conducted by controlling the stamping procedures with specific rotated alignment. Finally, to complete the quasi-periodic MIM structure, the SiO_2 precursor (PHPS) was hydrolyzed. Scanning electron microscopy (SEM) images presented in Figure 22b–e showed the fabricated plasmonic platforms with a single and quasi-periodic Ag nanopattern with the modulated alignments, indicating a large-scale, facile quasi-periodic nanopatterning process.

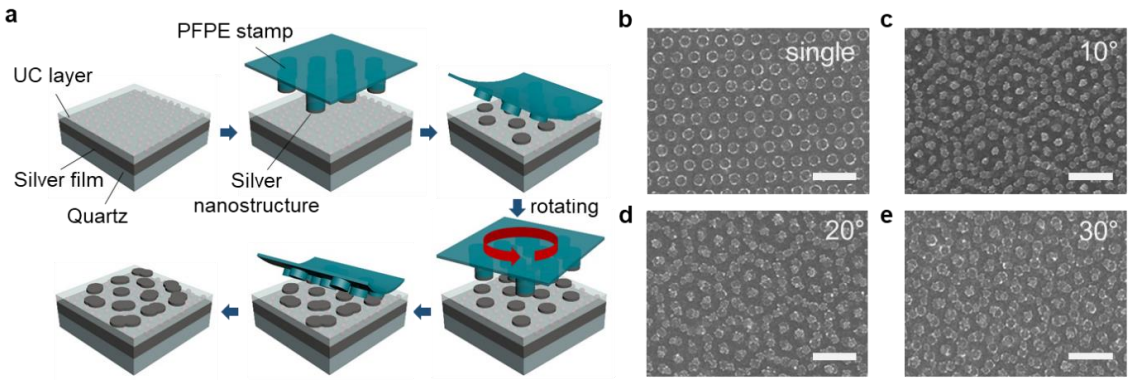

Figure 22. Fabrication process of the quasi-periodic plasmonic platform. (a) Schematics of the metal-contact nanolithography method used to achieve the double-metal-transferred nanostructure. (b–e) SEM images of the transferred metal nanopatterns: (b) original hexagonal array, (c–e) 10°, 20°, and 30° rotated alignments, respectively. The scale bar represents 1 µm.

Periodic plasmonic nanostructures can support a strong resonance mode at a specific wavelength. However, as this study requires resonance modes at relatively broadband emission ranges from UV to VIS as well as an incident NIR wavelength, well-defined periodic plasmonic arrays were not suited to the proposed approach. To overcome the constraint stated above is and to support strong plasmonic resonance modes at the broadband region, quasi-periodic Ag nanostructures were utilized in this study. The quasi-periodicity of the metallic nanostructures increased the number of wave vectors, k-vectors, in the reciprocal space, which allowed the plasmonic platform to generate diverse plasmonic modes at broad wavelengths (*96-99*). The diverse k-vectors of the proposed quasi-periodic plasmonic nanostructures were revealed via light diffraction and dark-field scattering imaging (Figure 23), showing the relative degree of diffraction and scattering intensity depending upon periodicity and rotation angle. Therefore, the proposed structures are able to support plasmon resonance modes at the desired wavelengths by controlling the quasi-periodicity of the metallic nanostructures.

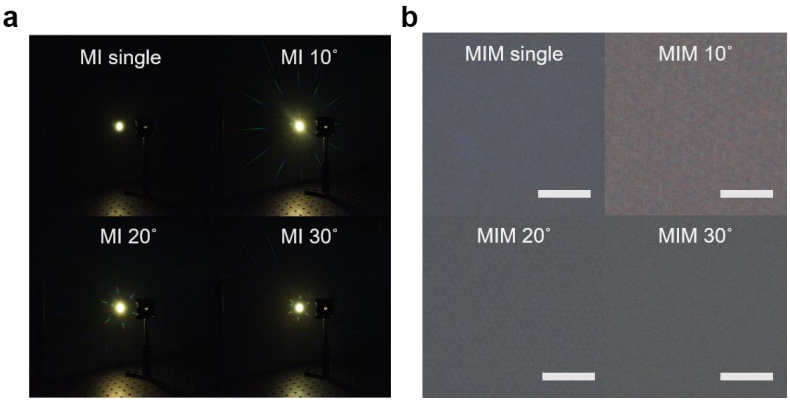

Figure 23. Light diffraction and scattering-field enhancement induced by quasi-periodic Ag nanostructures. (a) Light-diffraction properties under broadband (350–1100 nm) irradiation using a supercontinuum laser. (b) Dark-field scattering image. The scale bar represents 5 μm.

3.3 Photoswitchable upconversion photoluminescence

To study the advantages of the MIM plasmonic structures quantitatively, various structures were prepared, as shown in Figure 24; UCNP-embedded SiO_2 layer on a quartz substrate (Ref), single transferred Ag nanostructure on the UCNP-embedded SiO_2 layer (MI single), UCNP-embedded SiO_2 layer on Ag film (IM), single transferred Ag nanostructure on the IM structure (MIM single), and double transferred Ag nanostructures on the IM structure (MIM rotated angle), where MIM 10° was characterized as an optimized quasi-periodic structure. Using these elaborate structures, the plasmonic effects of the respective components in terms of PL enhancement were compared with those of the Ref. The UCPL intensity of the plasmonic platform was characterized using a lab-built PL measurement system, which featured a microscope.

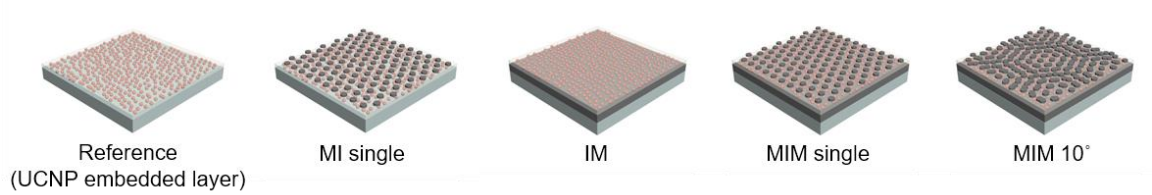

Figure 24. Schematic illustration of the various plasmonic platforms used for UCPL measurements.

As shown in Figure 25a, the UCPL of the MIM platforms was highly enhanced at all emission regions under high-pumped-power 980 nm excitation (588 W/cm^2). Herein, we calculated PL EFs as PL intensity of a particular structure divided by the normalized PL intensity of Ref (I/I_{Ref}) to easily identify the relative increase in PL intensity of each structure in comparison with Ref. In particular, under high-power NIR irradiation, the PL EFs of MIM 10° were 502, 436, 223, and 130 at the red (657 nm), green (545 nm), blue (452 nm), and UV (346 nm) emissions, respectively (c.f., the EFs of the single-structure MIM were 80.8, 165, 314, and 395, respectively). In addition, we measured the PL spectra under conditions of low-pumped-power 980 nm excitation (31 W/cm^2). The UV and blue emissive transitions of Tm^{3+} were not generated due to the fast relaxation of photon within the upconversion energy transfer. Under conditions of low-pumped-power 980 nm excitation (31 W/cm^2), the measured PL EFs of the MIM 10° for red and green emissions were 257 and 200, respectively (c.f., the EFs of the MIM single structure for red and green emissions are 225 and 144, respectively, Figure 25b). These results indicate significant PL EFs by two orders for MIM 10° under both high- and low-power NIR irradiations, retaining the orthogonal spectral conversion property. Notably, the highest EFs were obtained for MIM 10° compared to other double-metal-transferred platforms (e.g., MIM 20° and 30°), which was attributed to dominant absorbance and strong resonance coupling.

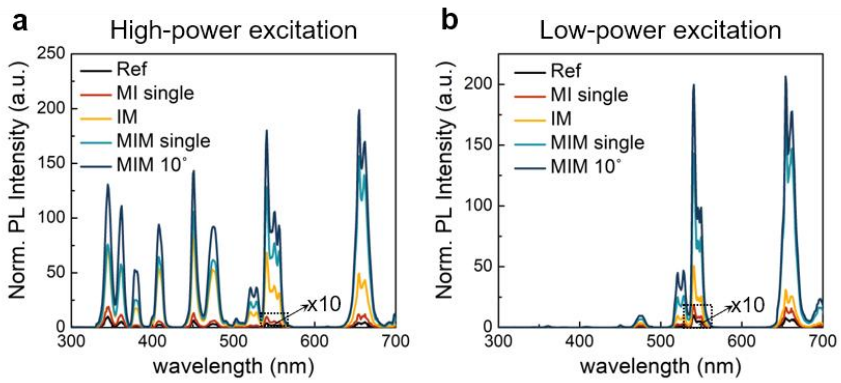

Figure 25. Optical characterization of the plasmonic platforms. (a) and (b) PL spectra of Ref (black line), MI single (red line), IM (green line), MIM single (sky-blue line), and MIM 10° (navy line) under high- (588 W/cm2) and low-power (31 W/cm2) NIR irradiation, respectively.

To confirm the photoswitchable characteristics of the UCPL, methodical investigations were conducted using the excitation power dependence of PL intensity. The UCPL requires a certain number of photons to excite the electrons to an emissive energy level, which results in nonlinearity with a weak pump power; conversely, linear behavior is demonstrated at a strong pump power region because the population of the excited states is sufficiently large (*99*). From the double-logarithmic PL intensity plots and by adjusting the pump power intensity at the strongest emission wavelength of the Er^{3+} (657 nm), a quadratic dependence was observed with a slope of approximately 2.00 at a weak excitation regime; at a strong pump power region, the slope decreased to approximately 1.00 (Figure 26a). Comparably, the strongest emission wavelength of Tm^{3+} (452 nm) exhibited quartic dependence with a slope of ~4.00 at the weak power-pump region; at the high power-pump region, the slope decreased to ~1.00 (Figure 26b). These results imply that the enhanced PL for the MIM 10° platform is occurred during the upconversion process, and the UCPL orthogonally complies with different optical mechanisms under high or low excitation power density without inter-activator energy transfer between Er^{3+} and Tm^{3+} ions (*99*, *100*).

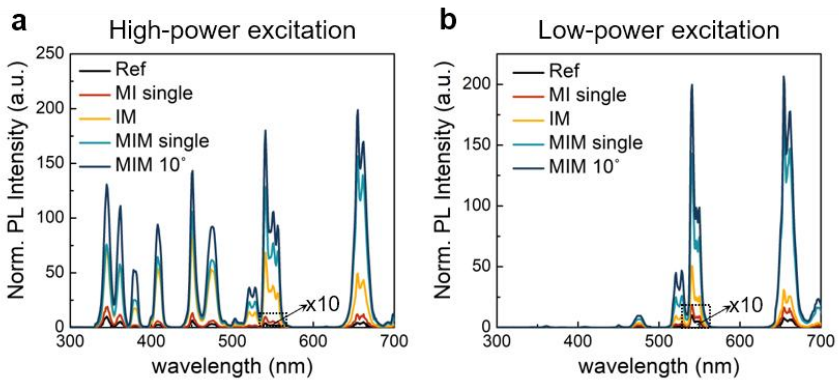

Figure 26. Correlation of intensity of UCPL at (a) 657 nm and (b) 452 nm emission and pumped-power density: Ref (black line) and MIM 10° (red line for 657 nm and blue line for 452 nm emission) structures on a double-logarithmic scale.

Based on these experimental results, a theoretical investigation of the correlation between Tm^{3+} and Er^{3+} transition states with incident excitation power intensity was studied using a rate equation analysis (*53, 101*). The calculation revealed a clear connection between incident pumped-power sensitivity and multiphoton upconversion. For example, under weak excitation, the densities of the Tm^{3+} excited states were small, and the decay process dominated the upconversion process. Upconversion of the Er^{3+} activator mainly occurred under weak power excitation, while the Tm^{3+} activator seldom functioned. Conversely, the Tm^{3+} emission rate at high transition states under strong excitation became linearly proportional to the excitation photon flux, and upconversion of the Tm^{3+} activator was evident. Therefore, whether under weak or strong power excitation, the conformity between the experimental outcome and the theoretical approach to upconversion demonstrated photoswitchable characteristics of UCPL by predominance of different activators, signifying orthogonality of the UCPL based on incident power.

To understand the origin of the enhanced UCPL from the MIM 10° platform, we characterized the absorbance spectra of the set of platforms. At 980 nm, the relative

absorbance supported quantitative improvement in absorption characteristics for the MIM 10° platform compared to those for Ref and MIM single (Figure 27a). Further estimation of the electric-field distribution at the NIR absorption wavelength of 980 nm was performed using a finite-difference time-domain (FDTD) calculation. In Figure 27b, strong field confinement at the 980 nm wavelength was evident within the UCNP-embedded SiO_2 layer, which was anticipated to improve the absorptivity of incident light in MIM 10°. The time-resolved PL (TRPL) rising response was studied to verify resonance mode at 980 nm. Interestingly, the MIM platforms produced a comparably shorter rising time than Ref. Based on this observation, absorption of incident 980 nm light was more efficiently acquired by the MIM 10° platform compared to those by other platforms.

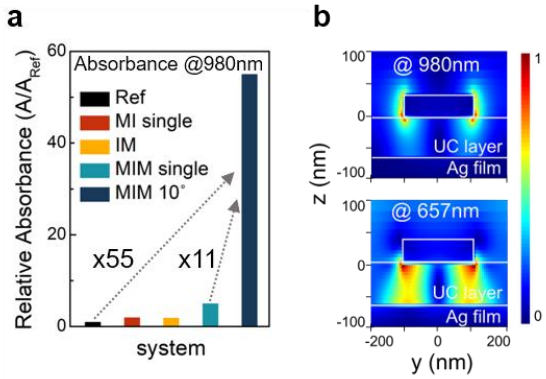

Figure 27. (a) Relative absorbance (A/A_{Ref}) for incident NIR. (b) Cross-sectional view of the normalized electric-field distribution of the incident 980 nm and the emitted 657 nm of the MIM 10° at the center of the UCNP-embedded layer.

In addition to determining the improvement in absorption at the excitation wavelength, the optical characteristics of emission wavelengths were investigated. As a representative of major emissive wavelengths, the electric-field distribution at the most enhanced UCPL wavelength (657 nm) showed strong resonance at the UCNP-embedded SiO_2 layer in MIM 10° (Figure 27b). Compared to the IM and the MIM single structures,

the relative electric-field intensity EFs (I/I_{IM}) of the MIM 10° platform were clearly amplified at the overall emission wavelengths (Figure 28a). These findings showed significantly enhanced UCPL emission, which was attributed to electric-field intensity enhancement at the emission region. Amplification of the electric field at the designated wavelength guided the qualitatively expedited decay rate. The improved spontaneous emission in the MIM 10° platform was further verified by the accelerated TRPL decay rate at the red emission, almost 4-fold faster than that of Ref and 1.5-fold faster than that of MIM single (Figure 28b: 271, 168, 161, 101, and 70 μs for Ref, MI single, IM, MIM single, and MIM 10°, respectively). Comparably, a detailed analysis of the TRPL revealed an analogous time-reduction magnitude at the red emission in MIM 10°, and the fast decay times were acquired at other emission regions. Combining the enhanced electric-field intensities with the rapid rates of decay, the MIM 10° platform demonstrated a significant improvement in broadband UCPL due to the resonance mode in both the NIR excitation and broadband emission regions. Therefore, this platform is proposed as suitable for utilization to facilitate photoisomerization of the DTE derivatives.

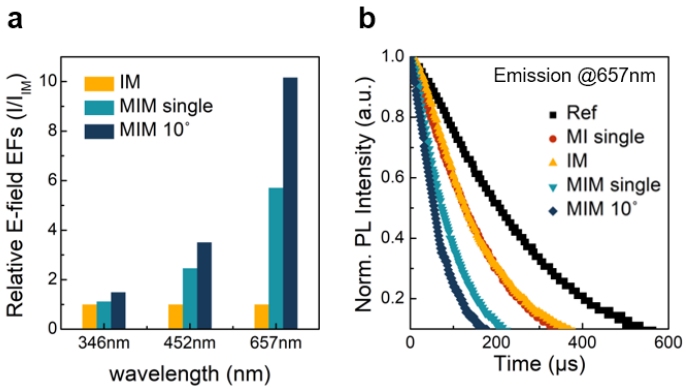

Figure 28. (a) Relative electric-field EFs (I/IIM) at emission wavelengths of 346, 452, and 657 nm. (b) Decay time of the UCPL for the five plasmonic structures at 657 nm emission under 980 nm excitation.

3.4 Plasmonically-assisted photoisomerization

The proposed plasmonic platform provides a feasible approach to reversible photoisomerization. As a proof of concept, a hybrid system was designed to combine the optimized plasmonic platform with the **2** DTE derivatives; this assembly resulted in a reversible photochromic system controlled by NIR excitation (Figure 29). Accordingly, DTE-doped SiO_2 film (270 nm) was placed on the top surface of Ref (referred to as PRef) and MIM 10° (referred to as PMIM 10°) by spin casting the DTE-diffused PHPS solution, followed by annealing. Due to its relatively strong PL enhancement over the entire emission region (as previously discussed), MIM 10° was selected as the representative plasmonic platform.

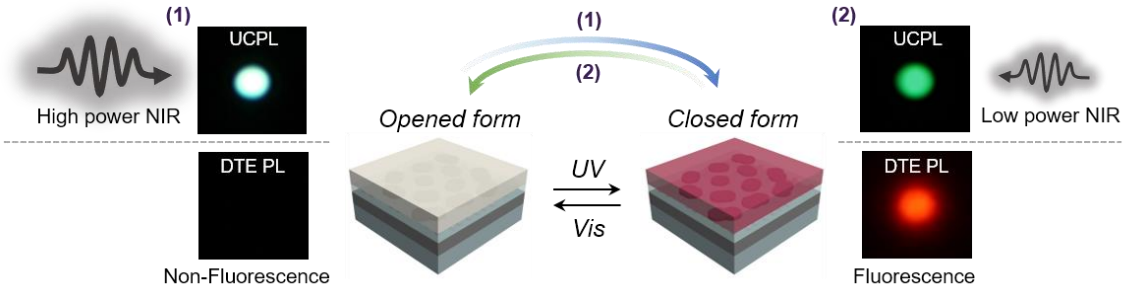

Figure 29. Schematic of the two-way photoswitch system at the quasi-periodic plasmonic platform with DTE film. The DTE film was formed on top of the quasi-periodic plasmonic platform to utilize the plasmonic-enhanced UCPL as a trigger for reversible photoisomerization via high- (588 W/cm2) and low- (31 W/cm2) power NIR irradiation. The photographs were acquired using 2 DTE-incorporated PMIM 10°.

To begin with, the ring-opened **2** DTE film did not show the PL characteristics. Under high-power NIR light (588 W/cm^2) irradiation, a bright white–blue light containing the UV emission appeared from the plasmonic-enhanced UCPL. This UV emission initiated a ring-closing reaction of the **2** DTE film, after which emission by the red PL (600 nm) was initiated by absorption of the amplified green UCPL in the platform. Noticeably,

the calculated photoisomerization QYs of DTE under UV irradiation was much higher than those under green irradiation, which validated that the green UCPL did not trigger reverse photoisomerization to revert to the ring-opened DTE film under high-power NIR irradiation (*102*, *103*). Subsequently, when low power-pumped NIR (31 W/cm^2) excitation was irradiated to the plasmonic platform of the ring-closed DTE film, only VIS UCPL was emitted; thus, the ring-opening reaction of the DTE film was triggered by absorbance of the green UCPL. Therefore, the greatly enhanced UCPL in the assembled plasmonic platform induced each directional photoisomerization by controlling the intensity of the excitation power.

To assess the degree of photoisomerization based on NIR irradiation, the absorbance spectra of the ring-opened DTE films after UV irradiation were compared with those after NIR irradiation. Interestingly, the absorbance spectra of NIR-triggered photocyclization were nearly identical to those of UV-triggered photocyclization, implying that UV intensity should be strong enough to induce photoisomerization of DTE (Figure 30). For the ring-opened DTE-doped SiO_2 without UCNPs, we obtained identical absorption spectra irrespective of NIR irradiation, which confirmed that UCNPs substantially functioned to trigger photoisomerization of the DTE.

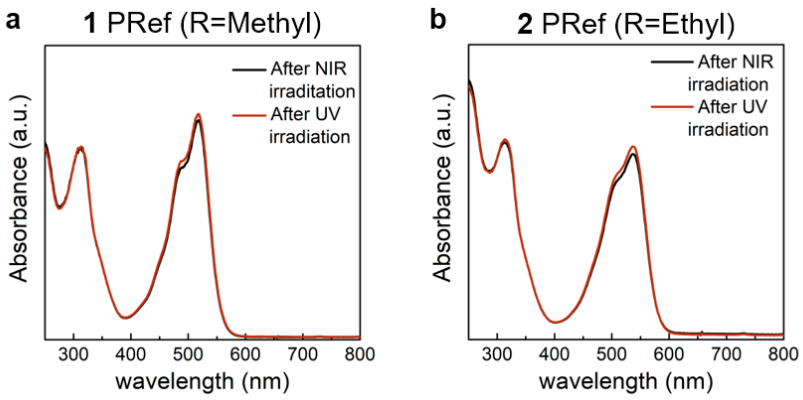

Figure 30. Comparison of absorbance spectra of the DTE film irradiated by NIR and UV. Absorbance spectra of DTE-derivatives (alkyl group (R) of methyl for (a) or ethyl for (b))-doped SiO_2 film on the Ref structure. Red and black curves denote the absorbance spectra of the film after UV and NIR irradiation, respectively. For NIR irradiation, we employed strong power density NIR laser (500 W/cm^2) for 10 min. For both DTE-derivatives-doped SiO2 film, we observed only 3% difference between the two differently irradiated films, which strongly implies that green UCL induced by strong NIR irradiation on the UCNPs did not affect significantly the molecular structures of the DTE.

Furthermore, to examine whether co-emitted green light with UV light hindered ring-opened reaction of DTE, we investigated the absorbance under the various incident light conditions that UV intensity was lower than that of the green intensity. Even under an extreme condition where the green incident intensity was over three times stronger than UV intensity, absorption spectra were identical with one under pure UV irradiation. Combined the results with the previously calculated photoisomerization QYs, therefore we convinced that the plasmonically enhanced UCPL successfully modulated each direction of photoisomerization, thereby functioning as the photoisomerization 'toggle' in response to NIR irradiation.

To evaluate the improvement in UCPL in the DTE-incorporated plasmonic platform, we carried out the TRPL analysis of PRef and PMIM 10° at the overlapped wavelengths between absorption of DTE-incorporated SiO_2 and UCPL. Compared to the UCPL of PRef,

that of PMIM 10° exhibited a highly accelerated decay rates due to strong resonant coupling in the UCPL emission region (Figure 31). In particular, the decay rates of PMIM 10° were about 2.7- and 2.6-fold faster than that of PRef at both the blue (452 nm) and green (545 nm) emissions, suggesting an enhanced UCPL for PMIM 10° via resonant coupling.

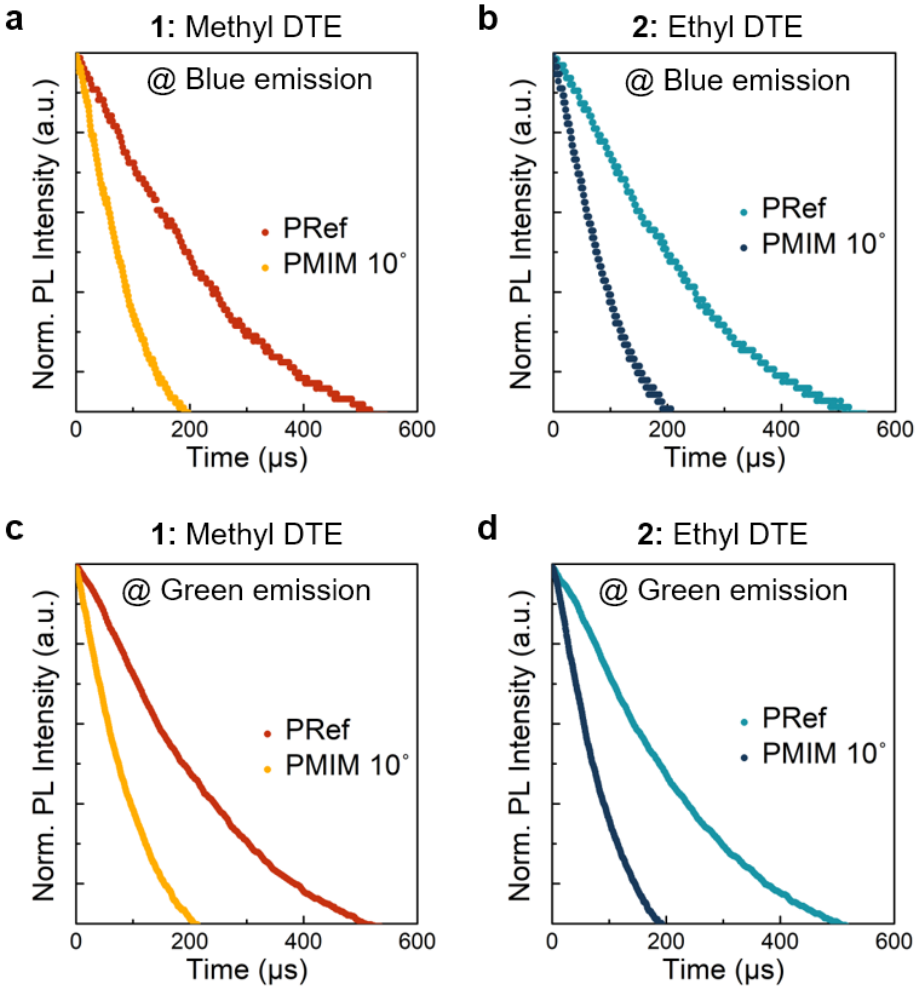

Figure 31. TRPL decay times at the blue and green emissions. (a) and (b) A comparison of decay times of the blue UCPL (452 nm) for the PRef and PMIM 10° under 980 nm excitation, respectively. Integration of the plasmonic platform caused the measured decay times of the blue emission to decrease from 256 to 93 μs at 1 DTE and from 269 to 100 μs at 2 DTE. (c) and (d) A comparison of decay times of the green UCPL (545 nm) for the PRef and the PMIM 10° under 980 nm excitation, respectively. Integration of the plasmonic platform caused the measured decay times

to decrease from 264 to 103 μs at 1 DTE and from 254 to 97 μs at 2 DTE by integration with the plasmonic platform.

To demonstrate photoisomerization performance of the proposed platform, the absorbance properties of the DTE films were characterized at both ring-opened and ring-closed structures (Figure 32a). To achieve UCPL-induced photoswitchability and obtain universality of the proposed template, we modified the intrinsic DTE into alkyl-group substituted forms such that **1** DTE (R = methyl) and **2** DTE (R = ethyl), and the optical performance of both DTE derivatives 1 and 2 was investigated for the doped photochromic films. The UV UCPL was generated under high pumped-power excitation of NIR, and an absorption increase in the DTE films was observed at around 545 nm, accompanied by color change to pink. Furthermore, following photocyclization, the ring-closed DTE films revealed PL in the 600 nm region (Figure 32b). Irrespective of the alkyl substituent species, the PL intensity of the DTE films was universally enhanced by integrating the MIM 10° plasmonic platform; this resulted in 9.78- and 9.68-fold increase at **1** and **2** DTE, respectively, compared to that of PRef (Figure 32c). A clear contrast existed between PL enhancement by PMIM 10° and that by PRef, as illustrated in the captured image of **2** PRef and **2** PMIM 10° (Figure 4d: inset photograph).

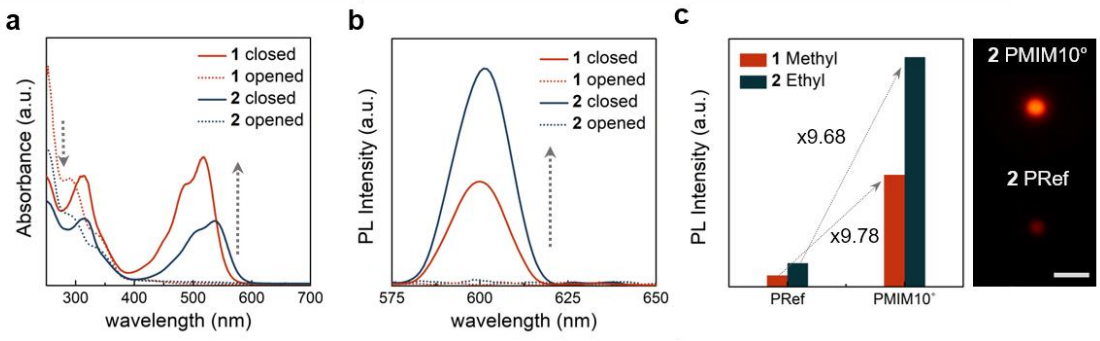

Figure 32. Optical characterization of the DTE-incorporated plasmonic platform. (a) Absorbance spectra of the ring closed/opened forms of the DTE film (1: Methyl- and

2: Ethyl-substituted DTE derivatives). Inset photograph showed macroscopic coloration following the ring-closing reaction of 2 opened (2o) to 2 closed (2c). (b) Normalized PL of the DTE film. The intensity of the PL increased with photocyclization under high-power (588 W/cm2) NIR irradiation for 28 s. (c) The PL intensity comparison of PRef and PMIM 10° platforms at the DTE emission wavelength (600 nm) for both utilized DTE derivatives. The macroscopic PL improvement driven by the plasmonic effect photographed under identical conditions. The scale bar represents 1 mm.

By monitoring the time-dependent absorbance of PMIM 10° at 600 nm in Figure 33a, the photostationary state for PMIM 10° was observed to be promptly reached within 10 s under high-power NIR (588 W/cm^2) excitation compared to that for PRef (30 s). Moreover, the ring-opening reaction of the DTE film under low-power NIR (31 W/cm^2) excitation was achieved within 30 s for PMIM 10° and within 60 s for PRef. The photoswitchable PL properties of the DTE were investigated further as shown in Figure 33b. The PL results showed similarity to the photoswitchable absorption properties in Figure 33a, which were obtained in an identical time domain. The plasmonically-enhanced broadband UCPL promoted the acceleration of forward and reverse photocyclization rates in the DTE film by three and two times, respectively; thus, the plasmonic-enhanced UCPL overcomes the pre-existing restrictions such as slow response time and low PL quantum efficiency. Hence, plasmonically-enhanced UCPL adequately facilitated not only for photocyclization under high-power NIR irradiation but also for reverse photocyclization under low power NIR irradiation.

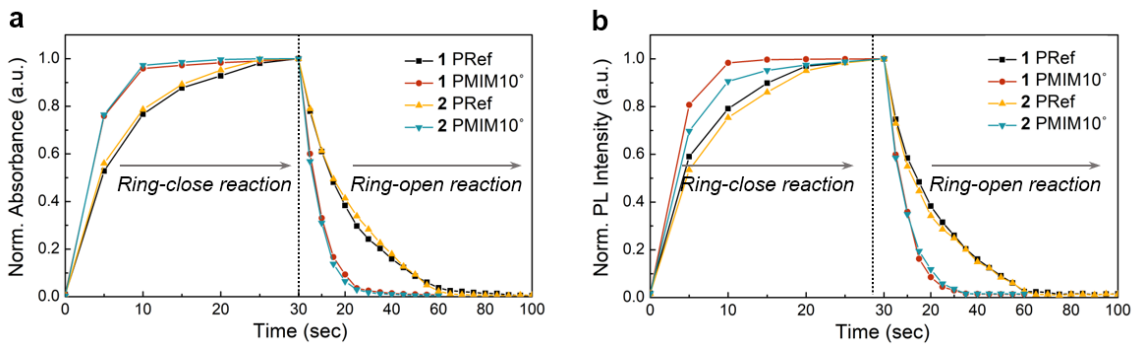

Figure 33. Time-dependent absorbance of PMIM 10° at 600 nm. (a) The time-dependent normalized absorbance at the absorption maximum wavelength of 528 nm (1 DTE) and 545 nm (2 DTE) switched by incident NIR power intensity from high- (588 W/cm^2) to low- (31 W/cm^2). (b) The time-dependent normalized PL intensity at the emission wavelength (600 nm) switched by incident NIR power intensity from high- (588 W/cm^2) to low- (31 W/cm^2).

3.5 Summary

In summary, this study presents a novel way to control photoisomerization using a single light source. It is facilitated by the quasi-periodic plasmonic platform to achieve significantly enhanced broadband UCPL that could emit UV to VIS efficiently. The proposed plasmonic structure was fabricated using the double metal-transfer technique with photoswitchable UCNPs. The prepared quasi-periodic plasmonic platform demonstrated a significantly two orders of magnitude enhancement in UCPL intensity at the overall broadband regime from UV to VIS, conserving highly distinctive PL spectra depending on the intensity of incident NIR. In the prepared platform, resonance couplings at the NIR absorption and the UCPL emission regions accelerated radiative decay and excitation rates, overcoming the inherent UCPL restrictions. Importantly, assembly of the quasi-periodic plasmonic platform with photochromic DTE derivatives facilitated acceleration of the reversible photoisomerization kinetics by three- or two-times and 10-

fold amplification of the PL intensity of the DTE film, which preserved considerable photo-fatigue resistance. The improved photoswitchability and strong UCPL in our platform will provide substantial plausibility and inspire new practical applications for UCNPs in spectroscopic and optical memory systems by achieving highly fast reversibility.

3.6 Methods

Synthesis of photoswitchable upconversion nanoparticles: β-$NaYF_4$:Yb^{3+}/Tm^{3+}@β-$NaYF_4$:Yb^{3+}/Er^{3+}@β-$NaYF_4$ UCNPs were synthesized via a sequential synthesis process by thermal decomposition of a trioleate precursor ($Ln(oleate)_3$), as previously described. $Ln(oleate)_3$ (Ln = Y (70%), Yb (30%), and Tm (0.5%)) precursors were prepared by mixing $Y(CH_3CO_2)_3{\cdot}H_2O$ (1.4 mmol), $Yb(CH_3CO_2)_3{\cdot}4H_2O$ (0.6 mmol), and $Tm(CH_3CO_2)_3{\cdot}H_2O$ (0.01 mmol), respectively, in a mixture of oleic acid (12 ml) and 1-octadecene (30 ml) at 393 K under a vacuum state. Next, a 20-ml methanol solution containing NH_4F (8.0 mmol) and NaOH (5.0 mmol) was added to the cooled $Ln(oleate)_3$ precursor solution and was mixed by stirring for 40 min at 323 K. After the methanol was distilled, the mixed solution was reacted at 588 K for 90 min under a gentle flow of 99.9% nitrogen gas. The synthesized UCNPs were rinsed with ethanol several times and were redispersed in hexane for the next synthesis. To synthesize β-$NaYF_4$:Yb^{3+}/Tm^{3+}@β-$NaYF_4$:Yb^{3+}/Er^{3+} UCNPs, hexane solution containing β-$NaYF_4$:Yb^{3+}/Tm^{3+} UCNPs was added to the cooled $Ln(oleate)_3$ complex solution. After extraction of hexane under an appropriate vacuum state, the above procedure was repeated to synthesize β-$NaYF_4$:Yb^{3+}/Tm^{3+}@β-$NaYF_4$:Yb^{3+}/Er^{3+} UCNPs and stored in hexane. Then, β-$NaYF_4$:Yb^{3+}/Tm^{3+}@β-$NaYF_4$:Yb^{3+}/Er^{3+}@β-$NaYF_4$ UCNPs

were synthesized through the same process with core-shell synthesis, using the synthesized β-$NaYF_4$:Yb^{3+}/Tm^{3+}@β-$NaYF_4$:Yb^{3+}/Er^{3+} UCNPs instead of core solution. The synthesized UCNPs were rinsed several times and were redispersed in chloroform at the target concentration.

Fabrication of a quasi-periodic metal-pattern-insulate metal film structure: The MIM platform was fabricated on a 6.25 cm^2 SiO_2 (quartz) substrate. The substrate was cleaned under ultrasonication for 10 min in acetone, isopropanol, and deionized water before being dried at 423 K with N_2 gas. Next, a 100-nm Ag film was deposited on the substrate via a thermal evaporator (KVT-D438, Korea Vacuum Tech) under 1 x 10^{-5} torr at room temperature. The same procedure was used to prepare Ag (35 nm)-deposited PFPE. The UCNP-embedded SiO_2 was fabricated by spin coating a mixed solution of 2.86-wt% β-$NaYF_4$:Yb^{3+}/Tm^{3+}@β-$NaYF_4$:Yb^{3+}/Er^{3+} UCNPs dissolved in toluene with 2.657-wt% PHPS onto the Ag film at 3000 rpm for 60 s. The prepared Ag-deposited PFPE stamp was applied to the UCNP-embedded SiO_2 layer with precise alignment and 0.5 bar pressure. To transfer the Ag nanostructure array, the stamp-contacted UCNP-embedded SiO_2 layer was hydrothermally polymerized below 393 K with suitable humidity for 20 min. After the first transfer, the PFPE stamp was detached from the UCNP-embedded SiO_2 layer. The second pattern was applied to the UCNP-embedded SiO_2 layer with precise rotation and 0.7 bar pressure. To fabricate the double transferred MIM structure, the second stamp was applied to the UCNP-embedded SiO_2 layer and was cured by hydrothermal polymerization below 413 K at suitable humidity for 1 h.

Fabrication of a photochromic film on a plasmonic platform: The photochromic-material-doped SiO_2 layer was designed to be sufficiently thick to enable measurement of the

appropriate optical property. The 1.5 wt% DTE-based photochromic material was dispersed in dibutyl ether with 18.6 wt% PHPS onto the MIM platform at 3000 rpm for 60 s. Then, the spin-casted film was annealed with 363K and suitable humidity for 90 min. This produced a fabricated photochromic film with a thickness of 270 nm (Figure S19).

Dynamic photoluminescence measurement setup: For collimation and manipulation of power, the NIR light from a continuous wave 980 nm laser (MDL-III-980-2W, CNI laser) was passed through a collimating cage assembly comprising two objective lenses (20x, NA: 0.4, WD: 1.7 mm, Newport) and a 50-μm pinhole rectangular neutral-density filter (0.04–4.0). Then, the collimated NIR light was reflected off a dichroic mirror (DMLP 735B, Thorlabs), and the upconverted Vis light was transmitted simultaneously. The upconverted PL of the plasmonic platforms was dimidiated at a beam splitter (BSW26R, Thorlabs) and was measured using a spectrometer (SP-2150i, Princeton Instruments) and CMOS camera (Alpha 7 Mark 3, Sony) after passing through a negative-type mask and a band-pass filter (FB600-40, Thorlabs). For the absorbance measurements, the collimated UV to NIR light from a Xenon lamp (200–2500 nm, Newport) was aligned with NIR light at the same light path for synchronous spectrometer measurement of PL and absorption. To ensure consistent measurement, two beam splitters (BSW20R and BSW26R, Thorlabs), instead of a dichroic mirror, were established on a rotatable stage and were calibrated after measurement. Thus, PL spectra, absorption spectra, and PL image were successfully obtained (Figure S20).

CHAPTER 4. ENANTIOMER-SELECTIVE MOLECULAR SENSING IN THE NONLINEAR OPTICAL REGIME VIA UPCONVERTING CHIRAL METAMATERIALS

Chirality is a ubiquitous property found in both naturally occurring and synthesized materials such as DNA, amino acids, carbohydrates, and pharmaceuticals (*104*, *105*). Chiral media are asymmetric such that the structure itself, the unit lattice or molecule, and their mirror image cannot be superimposable on each other. The chiral molecules typically exhibit distinct behavior with their mirror image forms, where these molecules are called enantiomers. Both enantiomers of a chiral molecule share almost identical physical properties (e.g. boiling point, chemical reactivity, and refractive index), while their flavor, odor, or biochemical functionality are distinct from each other. For instance, one enantiomer of a pharmaceutical may produce physiological activity, while the other may be inactive or even toxic (*105*). Hence a precise and efficient method to discriminate chiral molecules is crucial in the field of biochemistry, pharmaceuticals, and other chemical industries (*106*).

There are a number of techniques that can be utilized in order to discriminate enantiomers; these include both analytical chemistry methods such as gas chromatography (*107*), mass spectroscopy (*108*), liquid chromatography (*109*), and also optical spectroscopy methods including UV/VIS spectroscopy (*110*, *111*), circular dichroism (*112*, *113*), and optical rotation dispersion (*114*). The latter methods that rely on chiral-optical (chiroptical) effects have been widely employed in chiral sensing of enantiomers as they provide noninvasive and cost-effective characterization (*115*-*117*). Optically chiral

molecules exhibit chiroptical effects, where the enantiomers react differently to the handedness of an incident circularly polarized light. Circular dichroism (CD) is defined by the differential absorption (ΔA) of left (A_l) and right (A_r) circularly polarized lights, and is described as:

$$CD = \Delta A = A_l - A_r \tag{19}$$

The absorption can be rewritten in terms of refractive indices as (*104, 118*):

$$CD = \Delta A = \frac{2\pi l}{\lambda} \mathrm{Im}(n_l - n_r) \tag{20}$$

where λ is the wavelength of the incident light, l is the optical path length, and n_l (n_r) is the complex refractive index for the left (right) circularly polarized incident light. Eq.(20) implies that the chiral medium exhibits a distinct complex refractive index depending on the handedness of the circularly polarized light. Furthermore, by introducing the chiral parameter, ξ, to the complex refractive index of the chiral media as $n_{l,r} = n \pm \xi$, the CD of the chiral media is able to be expressed as (*119*):

$$CD = \Delta A = \frac{2\pi l}{\lambda} \mathrm{Im}(\xi) \tag{21}$$

Indeed, detecting enantiomers by utilizing chiroptical effects, such as CD spectroscopy, is a nondestructive method to differentiate the enantiomers. However, at the same time, the discrimination of the enantiomers has been limited by the intrinsically small chirality (ξ) of the chiral molecules, which are typically on the order of 10^{-3} (*120, 121*). Moreover, the

CD of these molecules is often located in the ultraviolet (UV) region, thus limiting the power of the excitation source, as UV excitation might be detrimental to biochemical species.

In order to mitigate these constraints, recent progress in plasmonics has been proposed to enhance the chiroptical response by leveraging the interaction between chiral molecules and structured man-made materials, known as metamaterials (*122-125*). In plasmonic metamaterials, typically the chiral molecules are placed near the hot spots of the plasmonic structures, which are supported by surface plasmon resonances (*125-127*). The hot spots interact with the chiral molecules which result in the enhancement of the inherent chiroptical response of the molecules, as well as the presentation of the molecule's chiral signature at the plasmonic resonance frequency (*128-131*). Furthermore, chiral plasmonic metamaterials have shown potential to generate condensed superchiral fields near the nanometallic structures (*132*). The generated superchiral fields can further interact with the molecule's chirality in the plasmonic structure, thus modifying the overall chiroptical effects of the system (*121, 133*). While plasmonic metamaterials have the potential to enhance the chiroptical behavior of the chiral molecules and possess chirality at the plasmonic resonance frequency, chirality detection methods via plasmonic metamaterials have primarily focused on the linear optical regime, which is governed by Eq. (21) (*134, 135*). More specifically, the modified linear CD (ΔA) depends on the extremely small change of the molecular chirality (ξ) (*120*). Consequently, the performance of the chiral-sensing methods using plasmonic structures has been severely limited by a small magnitude of change when evaluating the difference in CD.

In this work, we report a novel approach to detect the handedness of enantiomers in the nonlinear regime, which is facilitated by upconverting chiral plasmonic metamaterials (UCMM). The UCMM in aqueous solutions is designed to possess strong electric field confinement as well as a large CD in the NIR region. As a proof-of-concept demonstration, D-/L-glucose molecules are dissolved in a deionized water (DI water) solution where the UCMM device is placed. The different handedness of the chiral molecules interacts with the chiral metamaterial platform, which leads to a change in the CD of the UCMM device in the NIR region. The change in the CD of the device is then identified by comparing the intensity of the emitted nonlinear signal, which is the upconversion photoluminescence (UCPL), from the UCMM device under continuous-wave NIR laser excitation. The nonlinear signal generation substantially enhances the enantiomer selective detection performance by converting a small CD difference into a pronounced UCPL contrast. By analyzing the nonlinear signal intensity generated from the hybrid system, we discerned the handedness of the chiral analyte at different molar concentrations with high fidelity.

4.1 The operating mechanism of the chiral-sensing via chiral metamaterial

Figure 34 shows the overall setup for the enantiomer-selective molecular detection, where the device is placed inside the quartz cuvette and is immersed in DI water with D- or L-type chiral molecules. The chiral molecules interact with the UCMM device and induce CD changes in the reflected optical spectrum. Upon NIR excitation, the intensity of the upconverted emission in the visible (VIS) range varies depending on the handedness of

the chiral analyte in the solution. In this work, we defined the differential intensity of the upconverted light as the difference of the UCPL between right circularly polarized (RCP) and left circularly polarized (LCP) NIR excitation, thus representing the CD of the device in terms of the UCPL. Therefore, the handedness of the chiral molecules is deciphered by comparing the magnitude of the generated VIS light from each chiral species.

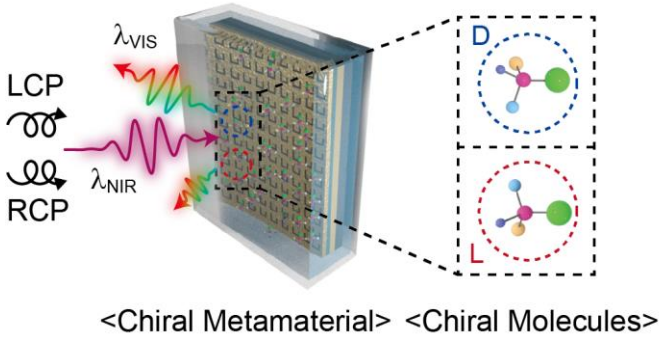

Figure 34. Chiral selective upconversion photoluminescence excited upon LCP and RCP near-infrared excitation. Two enantiomers are identified by comparing the intensity of upconversion photoluminescence, where the intensity difference stems from the different circular dichroisms of each enantiomer at the wavelength of 980 nm.

The upconversion nanoparticles, which are used to convert incident NIR light to VIS emission, are depicted in Figure 35. The prepared upconversion nanoparticles are composed of core-shell-shell structures in which the core is formed by a hexagonal phase (β) $NaYF_4$:Yb^{3+}, Er^{3+} with an interior shell of β-$NaYF_4$:Yb^{3+}, Tm^{3+} and an outer shell of β-$NaYF_4$. The Yb^{3+} ions serve as a sensitizer to improve the absorption of photons in the NIR region, specifically at the wavelength of 980 nm. The Er^{3+} and Tm^{3+} ions emit light in the VIS region via an upconversion process, and β-$NaYF_4$ is a commonly used host matrix (*136-138*). The outer shell passivates the inner core-shell structure to improve the efficiency of the upconversion process by mediating surface quenching (*139, 140*).

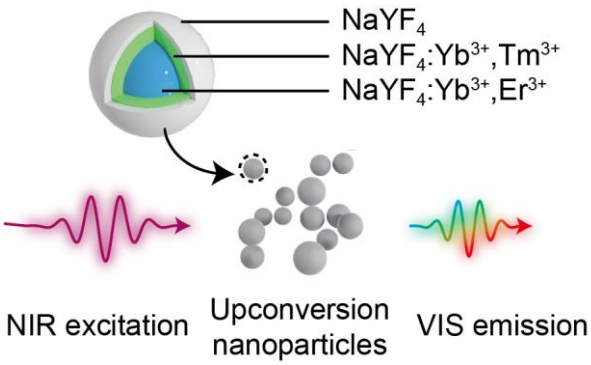

Figure 35. Schematic illustration of the core–shell–shell upconversion nanoparticles, which are embedded in the chiral meta-structure. The upconversion nanoparticles convert the near-infrared light to visible light through multiphoton absorption.

Figure 36a schematically describes the procedure of both the chirality transfer and the chiral interaction. As shown in the upper half of Figure 36a, the intrinsic CD of typical chiral materials is on the order of millidegrees (mdeg), occurring mainly in the UV region. When the chiral molecules are brought in close proximity to the plasmonic structures, the chirality of the molecules transfers to the plasmonic platform due to the Coulomb interaction between the molecules and the plasmonic structures (*130*, *131*). As a result, the plasmonic structure exhibits a shift in the far-field chiroptical response around the plasmonic resonance frequency. Moreover, by forming a highly resonant cavity and large superchiral fields within the plasmonic structure, the CD signal at the plasmonic wavelength can be further amplified (*120, 132*). The lower half of Figure 36a describes the chiral-chiral interactions that occur between the transferred chirality and the intrinsic chirality of the chiral metamaterials. Unlike the chiral molecules which possess a small CD, the chiral plasmonic metamaterials, in principle, allow the possession of a strong CD on the order of tens of degrees (deg) at the prescribed wavelength. The chiral interaction between the intrinsic and induced CD in the metamaterial gives rise to a change in the CD response of the device that depends on the handedness of both the chiral molecules and the

metamaterial. The expected results of the chiral-chiral interactions are shown in Figure 36b.

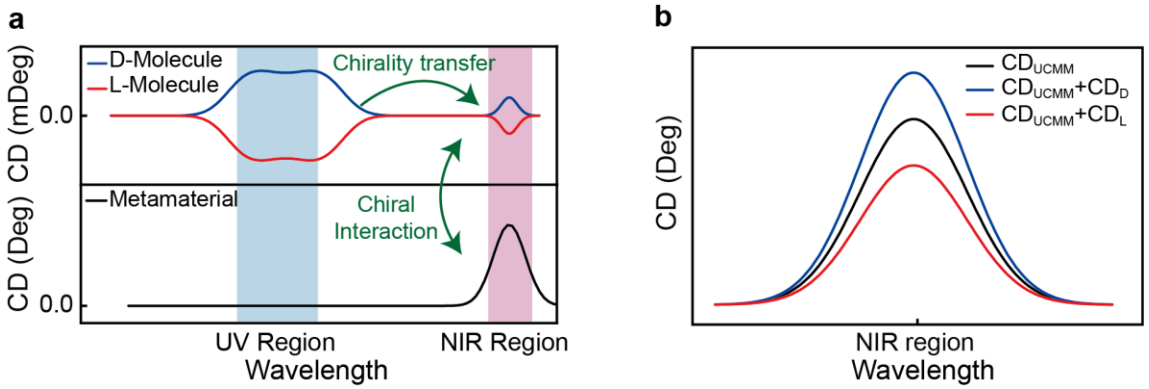

Figure 36. Illustration of the chiral-sensing operating mechanism via an upconverting chiral metamaterial. (a) Schematics of chirality transfer and the chiral interaction mechanism. The transferred chirality from the chiral molecule to the plasmonic platform further interacts with the intrinsic chirality of the chiral metamaterial. The total CD of the system is modified due to the chiral-chiral interactions. (b) Illustrations of the CD difference of the UCMM device, which are produced by the chiral interactions.

4.2 Numerical calculation of the upconverting chiral metamaterial

Figure 37 shows the geometrical design parameters and the calculated optical responses of the UCMM device. The UCMM device was composed of a J-shaped nanopatterned array engraved in a gold sheet. The patterned gold is placed above a second, thick gold film and is separated by a 160 nm-thick dielectric spacer, which contains embedded upconversion nanoparticles. As shown in Figure 37a, the unit cell of the patterned layer contains a J-shaped hole, and the structural asymmetry of the J-shaped structure determines the chirality of the device. The optically thick gold film underneath the dielectric spacer not only enhances the chiroptical responses of the device via reflection

of the optical waves, but also generates a large electric field confinement between the gold layers that increases the efficiency of the upconversion process (*141*).

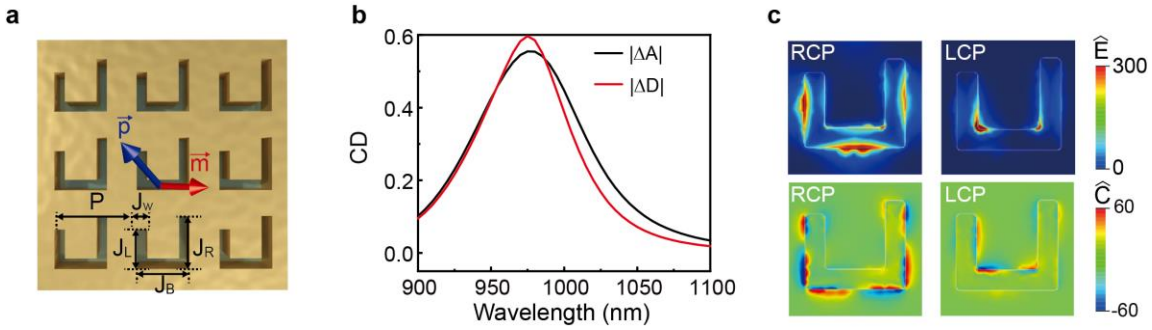

Figure 37. Design and numerical calculation of the UCMM. (a) Schematic illustration of the UCMM device overlaid with the relative orientations of the normalized electric (p, blue arrow) and magnetic (m, red arrow) dipole moments upon excitation with RCP light at a wavelength of 980 nm. Geometrical parameters: P = 400 nm, J_L = 195 nm, J_R = 230 nm, J_B = 270 nm, and J_W = 70 nm. (b) Calculated CD spectrum of the metamaterial from the differential absorption (black) and interaction of both dipole moments (red) of LCP and RCP light. (c) Field profile of the electric field enhancement (top) and chiroptical field enhancement (bottom) under RCP/LCP light at a wavelength of 980 nm.

The chiroptical responses in the chiral metamaterials can be understood based on the superposition of electric and magnetic multipole moments generated in the unit cell upon illumination. Here, we simplified the multipolar analysis into dipolar analysis by adopting the quasi-static approximation as the unit cell of the UCMM was small compared to the wavelength of interest (*119*, *142*). The dipole moments were obtained from $\vec{p} = \frac{1}{i\omega}\int_v \vec{J} dv$ and $\vec{m} = \frac{1}{2}\int_v \vec{r} \times \vec{J}\ dv$, where *p*, *m*, ω, and *J* represent the electric dipole moment, magnetic dipole moment, frequency, and polarization current, respectively (*26*, *143*, *144*). The intrinsic chiroptical response under normal incidence arises from the non-zero product of

in-plane electric and magnetic dipoles, where the CD of metamaterials using the dipole moments can be described as (*131, 145*):

$$|D| \propto |\mathrm{Im}[\vec{p}_{LCP} \cdot \vec{m}_{LCP}] - \mathrm{Im}[\vec{p}_{RCP} \cdot \vec{m}_{RCP}]| \tag{22}$$

where D represents the calculated CD using dipole moments, $\vec{p}$ and $\vec{m}$ are the electric and magnetic dipole moments and LCP/RCP denotes the left- and right-handed circular polarization of the incident light. The representative relative orientation of the in-plane electric and magnetic dipole moments under RCP excitation at the wavelength of 980 nm is illustrated in Figure 37a.

Figure 37b illustrates the CD calculation by using the definition of the absorption, $|\Delta A|$, and dipolar interaction, $|\Delta D|$, thereby elucidating the contrast between LCP and RCP excitation. Because this device is built from a reflective metamaterial, $|\Delta A|$ was calculated by subtracting the reflectance of LCP excitation from that of RCP excitation. The corresponding results of the chiroptical responses of the UCMM device with that of the the dipolar interactions validate the approach. The UCMM device exhibits a maximum CD around a wavelength of 980 nm. Spatial plots of both the electric field enhancement, $\hat{E}$, and the chiroptical field, $\hat{C}$, enhancement are depicted in Figure 37c, at an excitation wavelength of 980 nm for both LCP and RCP waves. Both field profiles were captured within the patterned gold sheet, 45 nm above the dielectric spacer. Here, we define the field enhancement as the near-field intensity at the engraved J-shaped patterned area normalized to the far-field intensity (*121*). Moreover, the chiroptical field is calculated from $C = \mathrm{Im}[\vec{E} \cdot \vec{H}^*]$. (*132*). The J-shaped pattern retained both large electric and chiroptical

field enhancements across the entire patterned area under RCP excitation. In contrast, the metamaterial exhibited electrical and chiroptical field enhancements only in a limited area under LCP excitation. Both the large field enhancement interacts with the chiral molecules that boost the intrinsic chiroptical responses of the molecules (*133*).

Furthermore, we numerically studied the interaction between the UCMM device and the chiral molecules. As shown in Figure 38a, both the chiral molecules and the UCMM device are represented by the electric and magnetic dipoles under circularly polarized incident light, where the dipole modes of the two molecular enantiomers have the same magnitude but opposite signs (*146*). When the D or L configuration of the chiral molecules are adjacent to the J-shaped pattern of the UCMM device, two types of chiral interactions occur as described in Figure 36a; 1) chirality transfer and 2) chiral-chiral interactions. The chirality transfer process from two molecular enantiomers induces different dipole modes at the plasmonic structure, where the magnitude of the transferred chirality is significantly improved by the strong $\hat{E}$ and $\hat{C}$. The transferred chirality then interacts with the intrinsic optical chirality of the UCMM device. The interactions result in the formation of net electric and magnetic dipoles, which depend on the configuration of the chiral molecules.

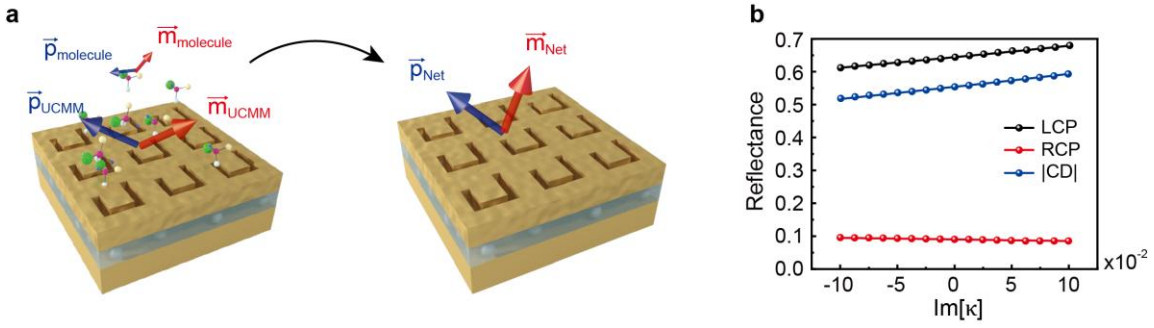

Figure 38. Numerical estimation of the chiral-chiral interactions. (a) Schematic illustration of the UCMM device and the chiral molecule that are represented by the electric and magnetic dipoles. The chiral interaction between the transferred chirality and intrinsic chirality of chiral metamaterial forms the net dipole moments. (b) Numerical estimation of the UCMM device with D- or L-type chiral molecules. The imaginary κ was used to capture the circular dichroism of the system.

Figure 38b shows numerical calculations of the reflectance and circular dichroism of the UCMM device interacting with hypothetical values of D- or L-type chiral molecules. For this fringe case study, the refractive index of DI water was used for the surrounding material and the revised constitutive relations with a chiral parameter κ were introduced to describe the interaction at the location of the J-shaped engraved domain where the chiral interactions are dominant. The chiral parameter, κ, represents the chirality at a wavelength of 980 nm, which originates from the chiral interactions between the chiral molecules and the UCMM device. The revised constitutive relations with the chiral parameter κ are described as (*119*):

$$\begin{pmatrix} \vec{D}/\varepsilon_0 \\ c\vec{B} \end{pmatrix} = \begin{pmatrix} \varepsilon_r & i\kappa \\ -i\kappa & \mu_r \end{pmatrix} \begin{pmatrix} \vec{E} \\ \eta_0 \vec{H} \end{pmatrix} \tag{23}$$

where *D*, *B*, *c*, and ε_0 represents their conventional notations in electromagnetics and ε_r and μ_r are the relative permittivity and permeability of DI water and η_0 is the impedance of free space. The positive (+) and negative (–) signs of κ represent the chiral interactions resulting from the D- and L-type chiral molecules, respectively. A purely imaginary κ with a magnitude ranging from -0.1 to 0.1 was employed to estimate the CD change due to the chiral interactions. We note that the hypothetical κ values of 0.1 and -0.1 are considered to be an extremely strong chiral interaction between the chiral molecules and the UCMM device and are both highly unlikely (*147*). Upon illumination of LCP or RCP light at the

wavelength of 980 nm, the reflection of the UCMM device was numerically adjusted based on the sign and magnitude of κ. The change in reflection with the LCP and RCP light results in CD changes of the hybrid system that show a contrast between the D- or L-type chiral molecules. The CD difference between the extreme cases of the chiral parameter κ, -0.1 and 0.1, shows that the contrast of CD is below 0.1 in the regular linear regime, which implies the need for a novel scheme to enlarge the contrast of CD for efficient chiral sensing.

4.3 Device fabrication and optical characterization

To experimentally demonstrate the enantiomer-selective molecular sensing in the nonlinear optical regime, the UCMM device was fabricated and characterized as shown in Figure 39. Figure 39a provides a scanning electron microscope (SEM) image of the UCMM device. To fabricate the device, a 100 nm thick gold film was deposited on the silicon substrate to form the optically thick lower layer of gold. Then the dielectric layer embedded with upconversion nanoparticles was placed on top of the bottom gold layer. The dielectric spacer was formed through a two-step process. The first step was to form the 155 nm thick layer of SiO_2 by spin-casting the upconversion nanoparticles mixed with the perhydropolysilazane (PHPS) SiO_2 precursor solution onto the bottom gold film. The second step was to deposit a 5 nm SiO_2 layer via atomic layer deposition (ALD). The second step was performed to minimize the surface roughness that occurred when forming the first layer of the dielectric spacer via hydrothermal polymerization. The top engraved, J-shaped, nanopatterned array of the gold sheet was fabricated by using standard e-beam

lithography and a gold deposition technique (see Methods for details). Figure 39b and c show the characterized and calculated reflection spectra of the UCMM, respectively, which are in good agreement. Strong circular dichroism is exhibited around a wavelength of 980 nm by minimizing the reflectance of RCP incident light, while largely reflecting LCP light.

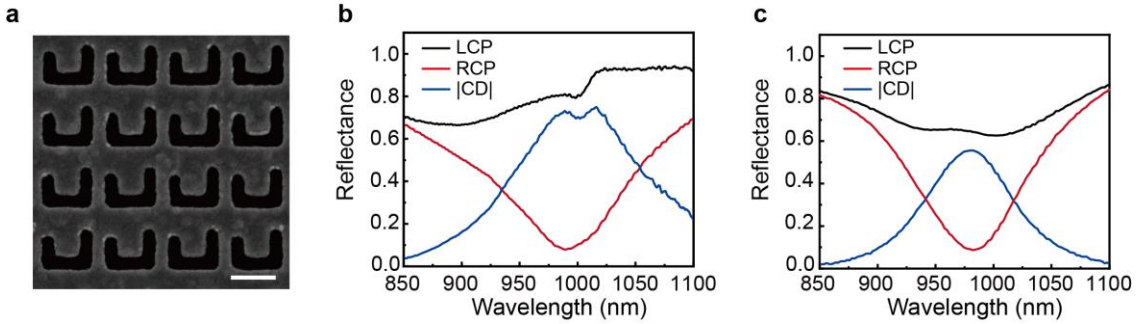

Figure 39. Experimental demonstration and optical characterization of the UCMM device. (a) Scanning electron microscope image of the UCMM device. The scale bar represents 250 nm. (b,c) Measured and calculated linear spectral responses of the UCMM device. A strong CD response was exhibited around a wavelength of 980 nm.

Figure 40a shows a transmission electron microscope (TEM) image of the core-shell-shell structure of the upconversion nanoparticles. The nanoparticles are placed in between the two metallic structures where the gap plasmonic resonance at 980 nm elevates the photon upconversion efficiency (*148-151*). As shown in Figure 40b, the presence of the upconversion nanoparticles enables the representation of the CD magnitude of the UCMM device by using the UCPL intensity. The *UCPL-CD* is described as $UCPL\text{-}CD = UCPL_{RCP} - UCPL_{LCP}$, where the $UCPL_{RCP}$ and $UCPL_{LCP}$ are the intensity of the generated UCPL signal under RCP and LCP light excitation, respectively. The UCPL signal was obtained by using a continuous wave laser at 980 nm with a power density of 40 W/cm^2 for both polarizations. The peaks of the *UCPL-CD* occurred at three primary colors (red, green, blue) in the visible range, namely, at the wavelengths of 452 nm ($^1D_2 \rightarrow {}^3H_6$), 545 nm ($^4S_{3/2}$

$\rightarrow {}^4I_{15/2}$), and 657 nm ($^4F_{9/2} \rightarrow {}^4I_{15/2}$) corresponding to transition states in the Tm^{3+} and Er^{3+} ions (see Fig. S2A for details) (*138*).

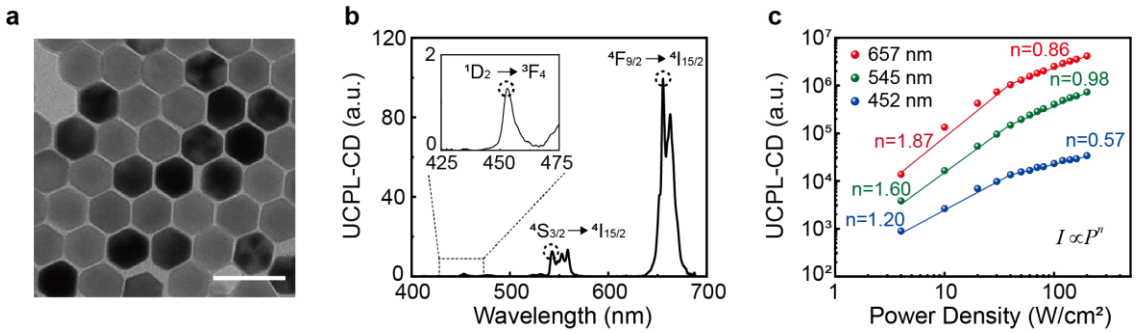

Figure 40. Optical properties of the synthesized upconversion nanoparticles. (a) Transmission electron microscopy image of core-shell–shell upconversion nanoparticles which are embedded in the chiral metamaterials. The scale bar represents 50 nm. (b) Upconversion photoluminescence spectrum of the UCMM device under 980 nm light excitation of 40 W/cm^2. The intensity of the spectrum was acquired by subtracting the photoluminescence intensity of the LCP excitation from the RCP excitation. (c) Excitation power density dependence of 657 nm (red), 545 (green), and 452 (blue) emission of the upconverting chiral metamaterials.

The excitation power survey for the three upconversion emission peaks from the UCMM is shown in Figure 40c. The acquired signals are plotted in a double logarithmic scale and fitted with a function $I \propto P^n$, where P represents the input power density. A noticeable change in the power dependence was observed around the power density of 40 W/cm^2 when transitioning between the nonlinear (n>1) and linear (n<1) regimes. Below the power density of 40 W/cm^2 is defined as the nonlinear regime as it requires multi-photon absorptions (n>1) to emit the upconverted light, while above the power density of 40 W/cm^2 is defined as the linear regime (n<1) as the single-photon excitation dominates the upconversion process. In addition, below the power density of 40 W/cm^2, the wavelength of 657 nm shows a clear quadratic dependence at the low power region, while other wavelengths show sub-quadratic dependence. The sub-quadratic dependence of both

shorter wavelengths, 545 nm and 452 nm, stem from the loss of UCPL that are absorbed by the gold film and the plasmonic cavity. In the nonlinear regime, a small change in the power density leads to a large variation in the intensity of *UCPL-CD*. By the definition of the *UCPL-CD*, the absorbed power density is related to the CD of the UCMM device. As already discussed in Figure 38b, the overall CD of the device could be increased (decreased) when the device interacts with the D- (L-) chiral molecules. Therefore, the small CD difference between the D- and L-chiral molecules could contribute to a large difference in the *UCPL-CD* intensity in the nonlinear regime, which provides a sufficient resolution to identify the handedness of chiral analytes.

4.4 Enantiomer-selective molecular sensing

The demonstration of enantiomer-selective detection using the UCMM device was carried out using either a white light or a 980 nm laser source. A white light source was utilized to emulate the conventional enantiomer detection in the linear regime. On the other hand, a 980 nm laser was employed to enable effective chirality sensing in the nonlinear regime. In our proof-of-concept demonstration, glucose molecules are chosen as the chiral analyte, since it is one of the most important energy sources of cell metabolism (*152*). Figure 41a depicts the detection of the handedness of the enantiomers with the UCMM device in 0.3M of D- and L-glucose solutions in the regular linear absorption regime, using the white light source. As expected in Figure 38b, a slight CD contrast between the two chiral solutions at a wavelength around 980 nm was observed. To investigate the CD contrast of different molarities of the glucose solution, the CD difference, ΔCD, was

defined by subtracting the CD of the L-glucose solution from the CD of the D-glucose solution at a wavelength of 980 nm. Figure 41b shows the ΔCD of various molarities of the glucose solution. Generally, the magnitude of the ΔCD increases as the molarity of the glucose solution increased from 0.05M to 0.3M, where the error bars correspond to the standard deviation in the triple trials of the measurement. The mean of the ΔCD could be used to identify the molarity of the solution, however, the relatively large error as well as the limited sensitivity substantially hampers the chirality sensing performance.

To overcome the limitation of chirality sensing in the linear regime, we studied the enantiomer-selective detection methods using the photon upconversion process. Figure 41c exhibits the chirality sensing results of 0.3M of D- or L-glucose aqueous solution using the UCMM device, which was excited under a 980 nm laser with a varying power density, ranging from 20 to 240 W/cm^2. The Δ*UCPL-CD* was defined to discriminate the D- and L-glucose solution, which is described as:

$$\Delta UCPL - CD = (UCPL - CD)_{RCP\ or\ \mathrm{LCP}} - \frac{(UCPL - CD)_{RCP} + (UCPL - CD)_{LCP}}{2}. \qquad (24)$$

The post-processing of the *UCPL-CD* of each glucose solution allows us to differentiate the two enantiomers by the sign of the Δ*UCPL-CD* intensity, where the positive and negative signs correspond to the D- and L-glucose molecules, respectively. Figure 41d depicts Δ*UCPL-CD* at an emission wavelength of 657 nm as a function of power density. We note that the power density up to 40 W/cm^2 is considered to be the nonlinear regime of the upconversion process and above 40 W/cm^2 is the linear regime of the upconversion

process as discussed in Figure 40c. As the power density became stronger, both the magnitudes of Δ*UCPL-CD* of D- and L-glucose solutions also increased gradually. However, the error bar of the Δ*UCPL-CD* abruptly increased after the power density of 40 W/cm^2, where the transition between the nonlinear and linear regimes of the upconversion process occurs.

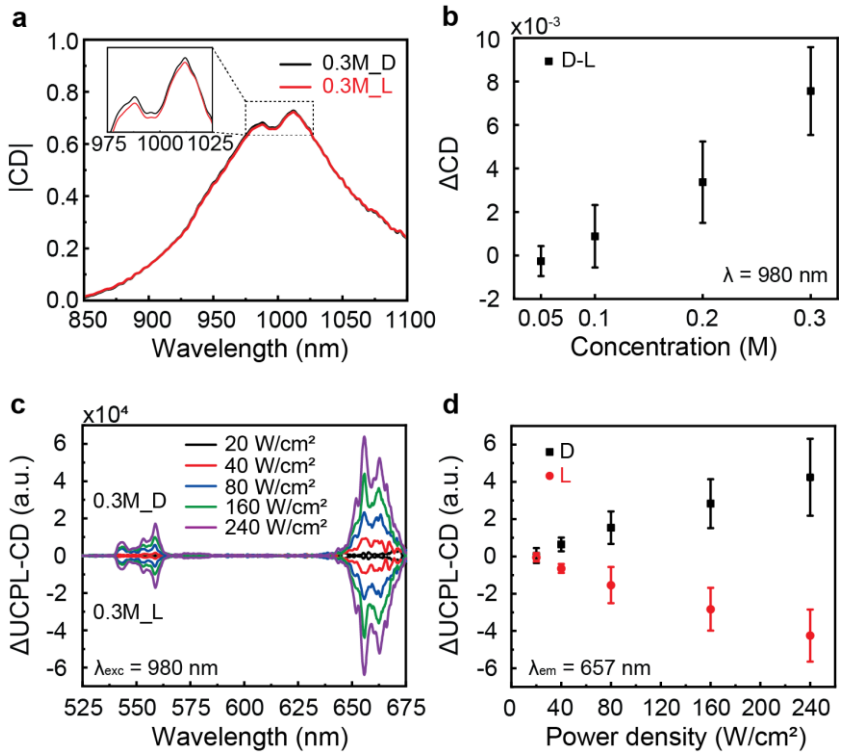

Figure 41. Enantiomer-selective molecular sensing. (a) Characterized CD of the chiral molecule/metamaterial hybrid system. The inset shows a zoom-in around the wavelength of 980 nm. (b) CD difference between the D- and L-Glucose in the hybrid system, while varying the molecular concentration of the chiral solution. (c) Characterized upconversion response of the chiral molecule/metamaterial hybrid system by varying the excitation power density. The Δ*UCPL-CD* was defined by the difference of the UCPL intensity of each hybrid system (D-/L-) and the averaged intensity of both UCPL intensity. (d) Δ*UCPL-CD* at the emission wavelength of 657 nm of the hybrid system. The error bars indicate the standard deviation.

4.5 Effective chirality sensing in the nonlinear regime

To further elucidate the effectiveness of chirality sensing in the nonlinear regime, we conducted a molarity survey at a power density of 40 W/cm^2 and 160 W/cm^2. Each power density represents the chirality detection in the nonlinear and the linear regimes of the upconversion process, respectively. Figure 42a shows the results of the Δ*UCPL-CD* from different molarities of the glucose solutions that are acquired in the nonlinear regime (40 W/cm^2). The small change of the CD in the UCMM device was shown as a significant modulation in the Δ*UCPL-CD*. The D- and L-glucose solutions were discerned from the sign of the signal. Moreover, the magnitude of the signals gradually increased as the molar concentration of the glucose solution increased. The results of the Δ*UCPL-CD* at a wavelength of 657 nm as a function of power density are shown in Figure 42b. The error bar was sufficiently small that both the handedness of the enantiomers and the molecular concentrations were clearly distinguishable. The Δ*UCPL-CD* signal exhibited a large contrast between the different molarities of the glucose solution and the error bars were small enough to identify the type of the enantiomer configurations. For comparison, in Figure 42c, identical experimental conditions were conducted in the linear regime of the upconversion process (160 W/cm^2). Compared to the chirality detection in the nonlinear regime that could boost the weak CD difference into a huge Δ*UCPL-CD* signal, the Δ*UCPL-CD* signals in the linear regime possessed relatively large error bars as shown in Fig. 5D. The relatively large error provided uncertainties in identifying both the molarity of the glucose solutions and the handedness of the enantiomers. By comparing the results of the chirality detection in the nonlinear regime (Figure 42a,b) and in the linear regime (Figure 46a,b and Figure 42c,d), the former strategy exhibited an efficient way to discriminate the handedness of the chiral analyte. The effectiveness of the chirality sensing

in the nonlinear regime via the UCMM device was achieved by bypassing the limitation of the conventional chiral detection method which relies on the extremely small molecular chirality.

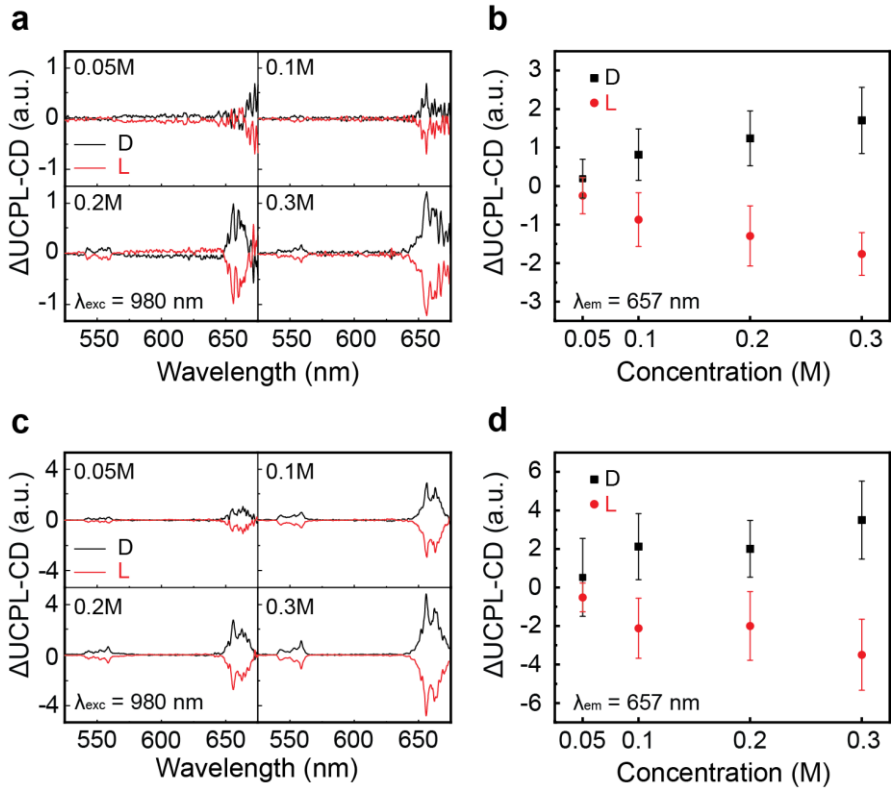

Figure 42. Molarity survey at the nonlinear (40 W/cm2) and the linear (160 W/cm2) region. (a) Characterized upconversion response of the chiral molecule/metamaterial hybrid system in the nonlinear regime by varying the molar concentration of the chiral solutions. (b) The ΔUCPL-CD at the emission wavelength of 657 nm of the hybrid system in the nonlinear regime. (c) Characterized upconversion response of the chiral molecule/metamaterial hybrid system in the linear regime by varying the molar concentration of the chiral solutions. (d) The ΔUCPL-CD at the emission wavelength of 657 nm when characterized in the linear region.

4.6 Summary

In this work, we have demonstrated a novel method for enantiomer-selective molecular detection based on upconverting chiral metamaterials. We experimentally showed the effectiveness of the enantiomer-selective sensing in the nonlinear regime, which was able to not only distinguish the handedness of enantiomers, but also identify the molecular concentration of the solutions. For such a demonstration, a chiral metamaterial was designed and fabricated that possesses both a giant electric and chiroptical field enhancement in the near-infrared region under RCP light excitation. In addition, the upconversion nanoparticles are synthesized and embedded in the dielectric layer of the chiral metamaterial, which emits the upconverted signals in the visible range by absorbing the near-infrared light. The chirality detection supported by upconversion nanoparticles converts a CD absorption measurement into a direct signal emission characterization. In the nonlinear regime of the upconversion photoluminescence, upon illumination at the wavelength of 980 nm of a certain power density, the intensity of the upconverted signal was able to be largely modulated by a small change of the CD in the UCMM device. Thanks to the large upconversion signal difference, the resolution of enantiomer-selective detection was significantly improved. By performing post-processing of the upconverted signal obtained from both chiral solutions, the handedness of the enantiomers was conveniently discriminated by the sign of the signal. Chirality sensing in the nonlinear regime can be envisioned for a diverse set of applications in biochemical analysis where the negligible chiroptical signal change could be captured by the large difference in the intensity of the generated nonlinear optical signals.

4.7 Methods

Device Fabrication: The fabrication process starts with forming the optically thick gold film on the silicon substrate by using the electron-beam (e-beam) evaporator (Denton Inc.). The thickness of the gold layer was 1000 Å and a thin titanium layer was used to promote adhesion between the gold and the silicon substrate. Then the dielectric layer with upconversion nanoparticles was prepared on the gold film in a two-step fabrication process. First, the 155 nm thick SiO_2 layer with embedded upconversion nanoparticles was fabricated by spin-coating a mixed solution of upconversion nanoparticles with perhydropolysilazane onto the gold film. Second, a 5 nm-thick SiO_2 layer was deposited at 150 °C using the plasma-assisted atomic layer deposition (Cambridge Fiji Plasma ALD system). Afterward, the gold film with the J-shaped engraved pattern array was fabricated with a standard electron beam lithography (E-beam litho., Elionix ELS-G100 EBL system) using poly(methyl methacrylate) (PMMA) as the positive tone electron resist. The 3 nm/45 nm-thick Cr/Au layer was deposited by e-beam evaporation and a lift-off process was performed in acetone to resolve the patterned array.

Optical Characterization: A tungsten halogen lamp (B&W Tek BPS 120) was used as a broadband light source to characterize the broadband optical response of the device. A linear polarizer and a quarter waveplate were used to create the circularly polarized light and the handedness of the circularly polarized light was controlled by the quarter waveplate. The reflection spectra of the device at normal incidence were acquired by a home-made spectroscopy system (see Supplementary Note 3 for further details). The objective lens (Mitutoyo, 20X plan Apo NIR infinity-corrected) was used to focus light onto the device and collect the reflected light from the device. The collected light was delivered to the spectroscopy system (Princeton Instrument Acton SP 2300i with PIXIS

400B camera). The reflectance of the device was normalized to the reflection from the plain gold film.

4.8 Supporting Information

Supplementary Note 1. Synthesis of Upconversion Nanoparticles

The core-shell-shell upconversion nanoparticles (UCNPs), *β*-$NaYF_4$:Yb^{3+},Tm^{3+}@β-$NaYF_4$:Yb^{3+},Er^{3+}@β-$NaYF_4$, were synthesized via a sequential epitaxial growth procedure of a trioleate precursor (Ln(oleate)$_3$) (*136*). Ln(oleate)$_3$ (Ln = Y (70%), Yb (30%), and Tm (0.5%)) precursors were prepared by dissolving $Y(CH_3CO_2)_3 \cdot xH_2O$ (1.4 mmol), $Yb(CH_3CO_2)_3 \cdot 4H_2O$ (0.6 mmol), and $Tm(CH_3CO_2)_3 \cdot xH_2O$ (0.01 mmol) in a mixture of oleic acid (12 ml) and 1-octadecene (30 ml) at 393 K under vacuum for 45 min. A solution of ammonium fluoride (8.0 mmol) and sodium hydroxide (5.0 mmol) in methanol (20 ml) was added to the cool-downed Ln(oleate)$_3$ precursor solution and was stirred at 323 K for 40 min. The methanol was subsequently distilled by modulating vacuum and temperature up to 353 K. After then, the temperature was quickly increased to 583 K and stirred for 90 min, maintaining the gentle flow of nitrogen gas. The synthesized *β*-$NaYF_4$:Yb^{3+},Tm^{3+} core UCNPs were rinsed using ethanol several times and redispersed in hexane. To synthesize the *β*-$NaYF_4$:Yb^{3+},Tm^{3+}@β-$NaYF_4$:Yb^{3+},Er^{3+} core-shell UCNPs, Ln(oleate)$_3$ (Ln = Y (80%), Yb (20%), and Er (2%)) precursors were prepared by dissolving $Y(CH_3CO_2)_3 \cdot xH_2O$ (1.6 mmol), $Yb(CH_3CO_2)_3 \cdot 4H_2O$ (0.4 mmol), and $Er(CH_3CO_2)_3 \cdot xH_2O$ (0.04 mmol) in a mixture of oleic acid (12 ml) and 1-octadecene (30 ml) at 393 K under vacuum for 45 min. After cooling the Ln(oleate)$_3$ precursor solution, the synthesized core UCNPs were added and

stirred. The hexane was distilled by increasing temperature up to 353 K and modulating vacuum condition. Then, the same procedure outlined above was repeated to acquire the *β*-$NaYF_4$:Yb^{3+},Tm^{3+}@β-$NaYF_4$:Yb^{3+},Er^{3+} core-shell UCNPs and redispersed in the hexane after rinsing several times. The inert outer shell was synthesized by adding core-shell UCNPs to the $Y(CH_3CO_2)_3 \cdot xH_2O$ (1.5 mmol) for $Ln(oleate)_3$ precursor. Figure 43 illustrates the XRD results of the synthesized core-shell-shell upconversion nanoparticles. Figure 44 shows the energy diagram and the optical chracterization results of the core-shell-shell UCNPs.

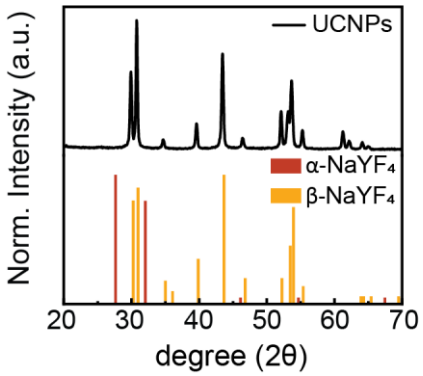

Figure 43. XRD measurement of β-$NaYF_4$:Yb^{3+},Tm^{3+}@$NaYF_4$:Yb^{3+},Er^{3+}@$NaYF_4$ UCNPs. The X-ray diffraction results were compared using JCPDS 027-1428 (α-$NaYF_4$) and JCPDS 016-0334 (β-$NaYF_4$).

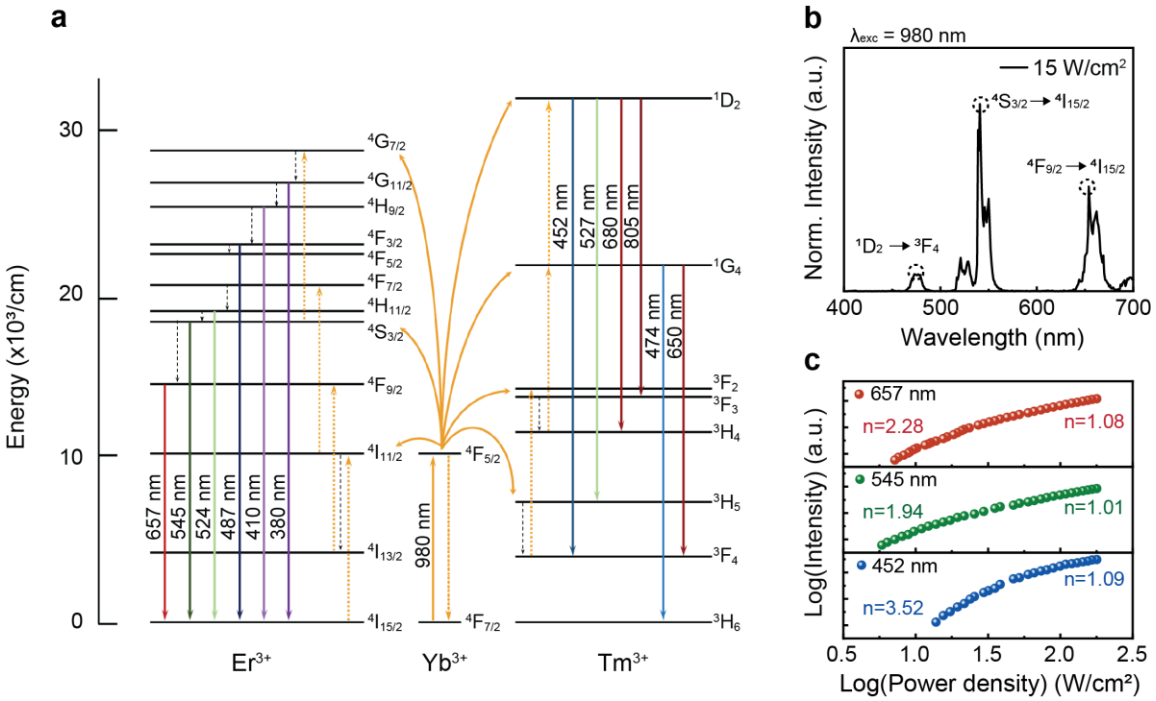

Figure 44. Energy diagram of the upconversion process and optical characterization of the UCNPs. (A) The Yb^{3+} ions functioned as sensitizers for the upconversion process which improve the absorption of near-infrared light. Both Er^{3+} and Tm^{3+} are the activators where the photon upconversion processes occur. (B) Normalized PL spectra of β-$NaYF_4$:Tm^{3+},Yb^{3+}@$NaYF_4$:Er^{3+},Yb^{3+}@$NaYF_4$ UCNPs excited at a wavelength of 980 nm. (C) Pump-power dependency of the upconversion photoluminescence at wavelengths of 452 nm, 545 nm, 657 nm.

Supplementary Note 2. Numerical Simulations

Both the geometrical parameter optimizations and the field enhancement calculations were performed by a commercial finite-element method package (COMSOL 5.4a). The UCMM device was aimed to possess large circular dichroism at a wavelength of 980 nm by maximizing the reflectance of the device at the LCP light and minimizing that of the device at the RCP light. The intrinsic circular dichroism of the optimized device was further described by the dipolar analysis.

As mentioned in the main manuscript, the dipolar analysis method was used to express the circular dichroism (CD) of the UCMM device. The CD effect of a single molecule can be described as the dot product of the two dipolar moments which can be described as (*131*):

$$CD_{molecule} \propto \mathrm{Im}[\vec{p} \cdot \vec{m}] \tag{25}$$

where $\vec{p}$ and $\vec{m}$ are the electric and magnetic dipole moments. In analogy to a single molecule, a meta-atom, which is a single unit cell of the metamaterials, is analyzed to describe the chiroptical properties of the chiral metamaterials. By adopting the quasi-static approximation, the CD of a meta-atom can be also described by using Eq.(25) (*119, 142*). The electric and magnetic dipole moments of the meta-atom was derived by decomposing of polarization $\vec{P} = \varepsilon_0(\varepsilon_m - \varepsilon_d)\vec{E}$ induced by the incident circularly polarized light wave in the UCMM device, where ε_0, ε_m, and ε_d are the vacuum permittivity, the relative permittivity of the meta-atom, and relative permittivity of the surrounding materials. Then

the polarization current $\vec{J} = -i\omega\vec{P}$ was calculated to obtain $\vec{p} = \frac{1}{i\omega}\int_v \vec{J}dv$ and $\vec{m} = \frac{1}{2}\int_v \vec{r} \times \vec{J}\ dv$, of the unit cell of the UCMM device (*26*).

Moreover, we calculated the electric field, $\hat{E}$, and chiroptical field, $\hat{C}$, enhancement at 980 nm for both LCP and RCP. Both the $\hat{E}$ and $\hat{C}$ enhance the chirality of the chiral molecules at the prescribed wavelength (*130, 132, 133*). The chiroptical field is described as $C = \mathrm{Im}[\vec{E} \cdot \vec{H}^*]$ and the definition of the $\hat{E}$ and $\hat{C}$ are shown below:

$$\hat{E} = \frac{|E_{Near\ \mathrm{Field}}|}{|E_{Far\ \mathrm{Field}}|}, \tag{26}$$

$$\hat{C} = \frac{|C_{Near\ \mathrm{Field}}|}{|C_{Far\ \mathrm{Field}}|}, \tag{27}$$

Figure 45 illustrates the field profile of the J-shaped engraved domain under RCP/LCP light at a wavelength of 980 nm. Both the $\hat{E}$ and $\hat{C}$ was shown to produce large magnitude under RCP incidence whereas the magnitude of each enhancement was negligible under LCP excitation.

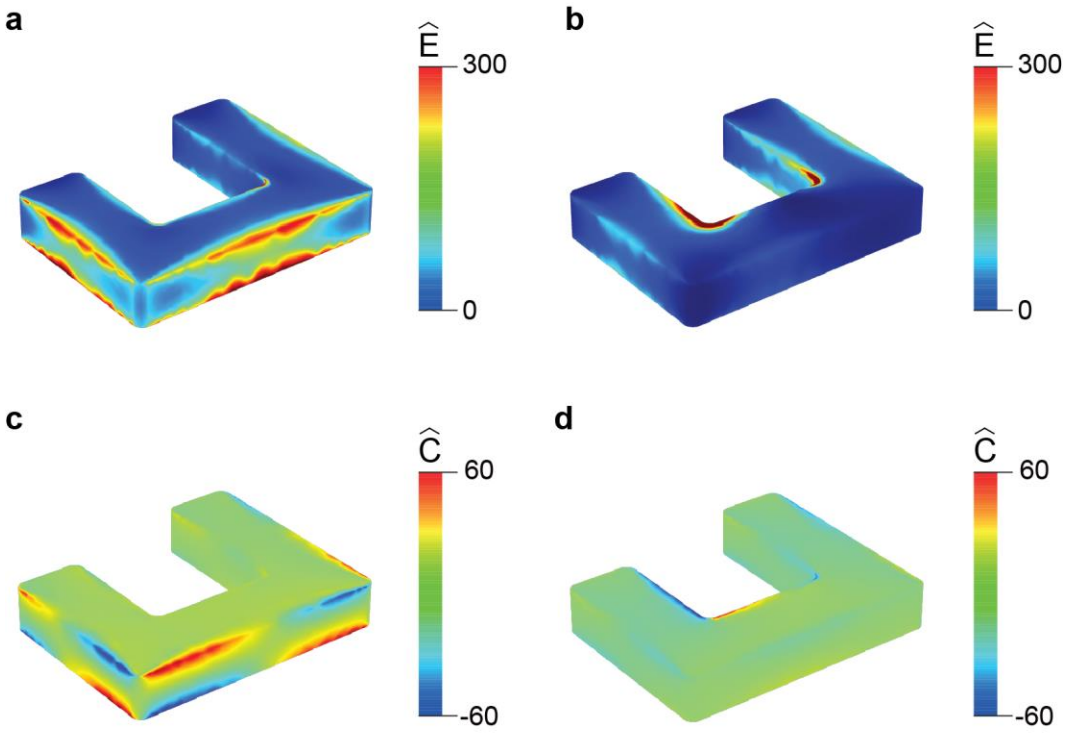

Figure 45. 3D Field profile of the electric field enhancement (top) and chiroptical field enhancement (bottom) at a wavelength of 980 nm. (a,c) Electric and chiroptical field enhancement under RCP excitation. (b,d) Electric and chiroptical field enhancement under LCP excitation.

Supplementary Note 3. Experimental Setup and Optical characterizations

A schematic of the homemade experimental setup for the optical characterization is shown in Figure 46a. Both a fiber-coupled tungsten halogen lamp (B&W Tek BPS 120) and a NIR laser (980 nm, Laserland) source were used to characterize the linear and nonlinear response of the UCMM device, respectively. A linear polarizer (LP) and half waveplate (HWP) were utilized to generate a circularly polarized wave; the quarter waveplate (QWP) converted the linear polarized light to circularly polarized light. The optical analysis was performed in reflection mode using beam splitters and optics. An objective lens (Mitutoyo, 20X plan Apo NIR infinity-corrected) was used to focus the incident light onto the sample and collect the reflected light from the sample. A short-pass filter (SPF) was inserted only during the nonlinear response analysis to filter out the NIR laser source. The collected light from the objective was delivered to the spectroscopy system which consisted of a monochromator (Princeton Instrument Acton SP 2300i) with a visible-near IR detector (PIXIS 400B camera). The reflectance of the UCMM device was achieved by normalizing the reflection from that of the plane gold film at the device.

Figure 46b depicts the state of polarization of the light source before and after the QWP. The rotating linear polarizer was installed to analyze the polarization of the light and depicted in a polar diagram. The acquired polarization diagrams are normalized by its maximum value. The peanut-shaped pattern with black dots describes polarization state of light before it passes through the QWP. The shape indicates that the polarization state before the QWP was a linearly polarized light. The RCP and LCP light, red and blue dots, was generated by orienting an incident linear polarized light at -45° and 45° to the fast axis, respectively.

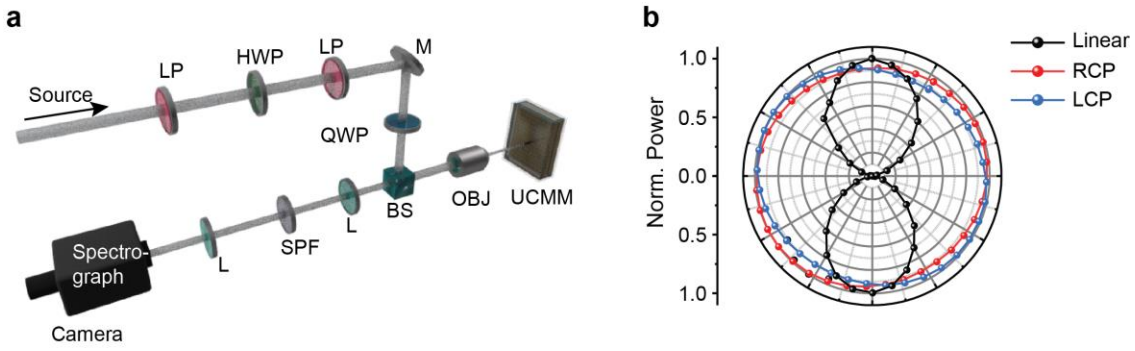

Figure 46. Experimental setup for characterizing the chiral signal from the UCMM device. (a) Home-made optical setup for the enantiomer-selective sensing. Abbreviation for optical components: LP: linear polarizer; HWP: half waveplate; M: mirror; QWP: quarter waveplate; BS: Beam splitter; L: lens; SPF: short-pass filter; QBJ: objective. (b) The angular distributions of polarized intensity.

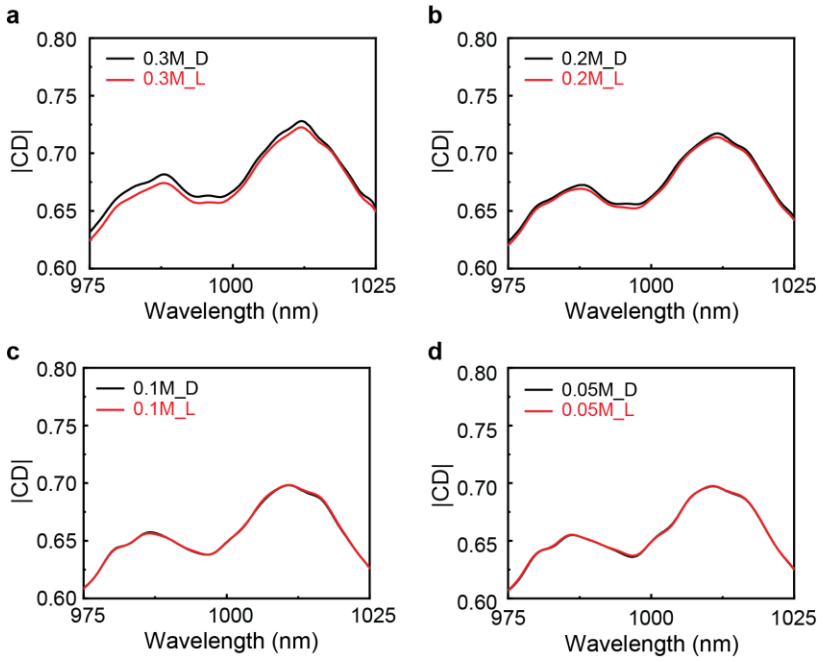

Figure 47. CD characterization of the chiral molecule/metamaterial hybrid system. CD difference between the D- and L-Glucose in the hybrid system increases as the molecular concentration decreases from (a-d).

CHAPTER 5. CONCLUDING REMARKS AND FUTURE DIRECTIONS

5.1 Conclusion

In this thesis, the primitive goal is to realize active nanophotonic devices that are controlled by either an external static electric field or incident light. The optical functionalities of the device were determined by the diverse dipole modes in the nanostructures where the dimensions of the engineered structures are smaller than the wavelength of the incident light. To achieve this goal, I first studied electric and magnetic dipole modes in diverse optical materials including plasmonics, dielectrics, and semiconductors. By engineering the dipole modes in the nanostructured metals or semiconductors, the nanostructures exhibited distinct optical behaviors which cannot be achieved in conventional bulk materials. In addition, active nanophotonic devices were realized by incorporating with the external electric field or the upconversion nanoparticles in the metamaterial system.

5.1.1 Electrically controlled nonlinear optics in magnetic Mie-type silicon metasurfaces

The pursuit of chip-scale and compact data processing capacity in a CMOS-compatible fashion has promoted the investigation of silicon-based photonic platforms for active optical functionalities via the nonlinear light-matter interactions. Crystal inversion symmetry, however, prohibits the second-order nonlinear processes in silicon under the electric dipole approximation. To address such a limitation, here we utilize electrical

signaling to demonstrate electric-field-induced second-harmonic generation in silicon metasurfaces that support a strong magnetic Mie resonance. Furthermore, significantly enhanced second-harmonic generation from the surface is achieved due to a strong circulating electric field induced by the magnetic Mie resonance mode. Our experimental characterizations and numerical modeling reveal that the efficiency of the field-induced frequency doubling peaks in the spectral vicinity of magnetic behavior, substantiating the synergic role of Mie resonances on the nonlinear optical generation from the silicon platform. Our finding reveals a generic route towards the dynamic control of second-order nonlinear processes, such as sum/difference frequency generation, optical rectification, and Pockels effect, in electrically active silicon metasurfaces.

5.1.2 Electric dipole modes with photon upconversion process for photochemical switching

Photochromic molecule-incorporated optical devices offer desirable properties for photocontrollable optical systems, including advanced optical data storage and super-resolution imaging. However, these molecules require multiple illumination sources, such as ultraviolet and visible light, for reversible photochemical reactions, which restricts their potential for advanced application. This study reports an effective strategy for modulating photoisomerization via a single near-infrared light source assisted by plasmonically-enhanced photoswitchable upconversion photoluminescence. The proposed quasi-periodic metal nanostructures to facilitate the resonance modes in the broadband region enabled substitution of the detrimental high-energy light source (i.e., ultraviolet light) with near-

infrared stimuli, which was associated with upconversion photoluminescence enhancement of over two orders with spectrum orthogonality. To validate this concept, the accelerated reversible-photoisomerization kinetics was experimentally confirmed by three- and ten-fold amplification of the photoluminescence intensities of the photochromic disulfonyldiarylethene derivatives. Further validation of the proposed strategy was performed using photodynamic imaging, which revealed accelerated photoisomerization, high photocyclization stability, and high spatial resolution.

5.1.3 Electric Dipole and Magnetic modes for Chiral sensing

Enantiomers are chiral isomers in which the isomer's structure itself and its mirror image cannot be superimposable on each other. Enantiomer selective sensing is critical as enantiomers exhibit distinct functionalities to their mirror image. Discriminating between enantiomers by optical methods has been widely used as these techniques provide nondestructive characterization, however, they are constrained by the intrinsically small chirality of the molecules. Here, we demonstrate a method to effectively discriminate chiral analytes in the nonlinear regime, which is facilitated by an upconverting chiral plasmonic metamaterial. The different handedness of the chiral molecules interacts with the chiral metamaterial platform, which leads to a change in the circular dichroism of the chiral metamaterial in the near-infrared region. The contrast of the circular dichroism is identified by the upconverted signal in the visible region.

5.2 Outlook

5.2.1 Pixelated Photodetectors based on Plasmonic Metamaterials

Photodetectors, which convert light into electrical signals for direct readout or further control of downstream elements in an integrated system, represent a pillar of the entire photonics industry. In particular, semiconductor-based photodetection technologies, such as CCD (charge-coupled device) or CMOS (complementary metal-oxide-semiconductor) sensor arrays, are used in a variety of critical applications, ranging from digital cameras to health care devices and surveillance systems. These conventional photosensors, typically consisting of an array of micrometer-scale pixels with an individual photodetector and active amplifier assigned to each pixel, are encountering a series of growing challenges**.** First, the size of the pixel cannot be continuously shrunk well below the wavelength, because of the diffraction limit in classical optics. Crosstalk between adjacent pixels caused by scattering of light becomes progressively pronounced as pixel size gets smaller, thereby significantly reducing the efficiency and image quality of the device. Second, future photonic systems demand a complete set of information of light.

However, the pixel array in today's CCD and CMOS can only record the intensity information, while the wavelength and polarization of light are simply lost once it is absorbed by the photodetector. Color filters (*e.g.* Bayer filter) using dye-doped glass or polymers are necessary to assign a specific narrow-band response (red, green, and blue, as widely used in the RGB model) to each pixel in order to produce color images. However, when the size of the pixels shrinks to micron and submicron scale (*i.e.*, wavelength scale), the fabrication of the dye filters becomes increasingly complicated and prone to

imperfections. Meanwhile, the well capacity shrinks, leading to a reduced dynamic range. This is also accompanied by a compromised sensitivity of the pixels as light impinges upon a smaller area for the photo-collection. Third, it would be a daunting task, if not impossible at all, to extend such silicon-based technology for longer wavelength (with the corresponding photon energy less than the electronic bandgap of semiconductors) or to use them for extracting the polarization information of light without additional, bulky elements placed in front of them.

A new paradigm of photodetectors to address the aforementioned challenges demands a deep understanding of light-matter interactions in materials or structures that are not readily obtained in nature. Over the past decade, optical metamaterials have shown the capability of creating extraordinary properties and subsequently controlling the flow of light in an unconventional way. Metamaterials comprise structured elements with their size and spacing much smaller than the wavelength of interest. These artificially structured elements, acting as man-made "atoms", interact with external light waves in a prescribed manner (*153-156*). At the macroscopic level, the assembly of these inhomogeneous, subwavelength elements can be viewed as homogenized media with effective material parameters derived from the structure and arrangement of the meta-atoms. Remarkably, the effective material properties are primarily determined by the size, shape, or structure of the building blocks, rather than the intrinsic properties of the constituent materials that constitute the metamaterials. By exploiting different building blocks, researchers have been able to engineer properties of metamaterials with unprecedented degrees of freedom, and have demonstrated a wide range of highly unconventional electromagnetic behaviors including diluted metals (*157*), artificial magnetism (*158*), strong chirality (*159, 160*), and

negative (*161, 162*), zero (*163, 164*), or extremely large refractive indices (*165, 166*).

Based on the prescribed extraordinary optical properties of metamaterials, we can develop the metamaterial-based photoconductor which maximizes sensing in the NIR region. Specifically, the structure can be designed which is able to convert optical signals of incoming optical information, such as wavelength, intensity, and polarization, to electrical signals by tailoring the design parameter of the top electrode of a vertical type of metal-semiconductor-metal (MSM) photoconductor. Figure 48 schematically illustrates the proposed device, which consists of two pieces of patterned metallic films along with a layer of photoconductive material sandwiched in between. Amorphous germanium was selected as a photoconductive material for infrared sensing and gold for two metallic films. With the ability to discriminate the polarization, intensity, wavelength of the incoming light in the NIR region and the cost-effective configuration, the proposed device can be a good candidate for replacing the current pricey Lidar system.

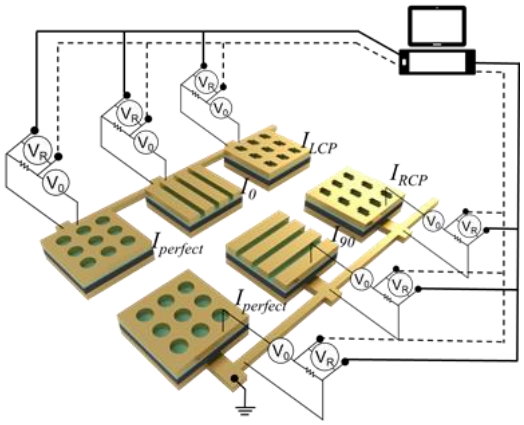

Figure 48. Schematic of polarization-resolved metamaterial photosensors for complete diagnosis of polarization of light. The six closely spaced pixelated metamaterial absorbers have different responsivity to different polarization components of the incoming light. This absorption consequently translates to the generation of an electrical signal due to the photoconductive spacer in each pixel.

REFERENCES

1. W. Cai, V. Shalaev, Optical Metamaterials: Fundamentals and Applications. *Optical Metamaterials: Fundamentals and Applications* (Springer, New York, 2010).

2. N. F. Yu *et al.*, Light Propagation with Phase Discontinuities: Generalized Laws of Reflection and Refraction. *Science* **334**, 333-337 (2011).

3. J. B. Pendry, A. J. Holden, D. J. Robbins, W. J. Stewart, Magnetism from conductors and enhanced nonlinear phenomena. *IEEE Trans. Microw. Theory Tech.* **47**, 2075-2084 (1999).

4. M. Hentschel, M. Schaferling, X. Y. Duan, H. Giessen, N. Liu, Chiral plasmonics. *Sci. Adv.* **3**, e1602735 (2017).

5. L. Kang *et al.*, Preserving Spin States upon Reflection: Linear and Nonlinear Responses of a Chiral Meta-Mirror. *Nano Lett.* **17**, 7102-7109 (2017).

6. W. S. Cai, A. P. Vasudev, M. L. Brongersma, Electrically Controlled Nonlinear Generation of Light with Plasmonics. *Science* **333**, 1720-1723 (2011).

7. M. Taghinejad, Z. H. Xu, K. T. Lee, T. Q. Lian, W. S. Cai, Transient Second-Order Nonlinear Media: Breaking the Spatial Symmetry in the Time Domain via Hot-Electron Transfer. *Phys. Rev. Lett.* **124**, 013901 (2020).

8. S. F. Lan *et al.*, Backward phase-matching for nonlinear optical generation in negative-index materials. *Nature Mater.* **14**, 807-811 (2015).

9. A. Alu, A. Salandrino, Negative effective permeability and left-handed materials at optical frequencies. *Opt. Express* **14**, 1557-1567 (2006).

10. J. D. Jackson, *Classical electrodynamics. 3rd edition* (Wiley, New York, 1999).

11. X. F. Fan, W. T. Zheng, D. J. Singh, Light scattering and surface plasmons on small spherical particles. *Light Sci. Appl.* **3**, e179 (2014).

12. G. Mie, Articles on the optical characteristics of turbid tubes, especially colloidal metal solutions. *Ann. Phys. (Berlin)* **25**, 377-445 (1908).

13. H. Horvath, Gustav Mie and the scattering and absorption of light by particles: Historic developments and basics. *J. Quant. Spectrosc. Radiat. Transfer* **110**, 787-799 (2009).

14. R. W. Boyd, Nonlinear Optics, 3rd Edition. *Nonlinear Optics, 3rd Edition* (2008).

15. M. Cazzanelli, J. Schilling, Second order optical nonlinearity in silicon by symmetry breaking. *Appl. Phys. Rev.* **3**, 011104 (2016).

16. O. A. Aktsipetrov *et al.*, dc-electric-field-induced and low-frequency electromodulation second-harmonic generation spectroscopy of Si(001)-SiO2 interfaces. *Phys. Rev. B* **60**, 8924-8938 (1999).

17. F. Auzel, Upconversion and anti-stokes processes with f and d ions in solids. *Chem. Rev.* **104**, 139-173 (2004).

18. R. J. Mears, L. Reekie, I. M. Jauncey, D. N. Payne, Low-Noise Erbium-Doped Fiber Amplifier Operating at 1.54-Mu-M. *Electron. Lett.* **23**, 1026-1028 (1987).

19. S. Heer, K. Kompe, H. U. Gudel, M. Haase, Highly efficient multicolour upconversion emission in transparent colloids of lanthanide-doped NaYF4 nanocrystals. *Adv. Mater.* **16**, 2102-2105 (2004).

20. K. -T. Lee *et al.*, Simultaneous Enhancement of Upconversion and Downshifting Luminescence via Plasmonic Structure. *Nano Lett.* **15**, 2491-2497 (2015).

21. J. Valentine *et al.*, Three-dimensional optical metamaterial with a negative refractive index. *Nature* **455**, 376-379 (2008).

22. N. Fang, H. Lee, C. Sun, X. Zhang, Sub-diffraction-limited optical imaging with a silver superlens. *Science* **308**, 534-537 (2005).

23. B. Frank *et al.*, Large-Area 3D Chiral Plasmonic Structures. *ACS Nano* **7**, 6321-6329 (2013).

24. S. Y. Chang, X. X. Guo, X. J. Ni, Optical Metasurfaces: Progress and Applications. *Annu. Rev. Mater. Res.* **48**, 279-302 (2018).

25. P. Grahn, A. Shevchenko, M. Kaivola, Electromagnetic multipole theory for optical nanomaterials. *New J. Phys.* **14**, 093033 (2012).

26. A. B. Evlyukhin, T. Fischer, C. Reinhardt, B. N. Chichkov, Optical theorem and multipole scattering of light by arbitrarily shaped nanoparticles. *Phys. Rev. B* **94**, 205434 (2016).

27. A. E. Miroshnichenko *et al.*, Nonradiating anapole modes in dielectric nanoparticles. *Nature Commun.* **6**, 8069 (2015).

28. J. Chen, J. Ng, Z. F. Lin, C. T. Chan, Optical pulling force. *Nature Photon.* **5**, 531-534 (2011).

29. S. A. Maier *et al.*, Plasmonics - A route to nanoscale optical devices. *Adv. Mater.* **13**, 1501-1505 (2001).

30. W. L. Barnes, A. Dereux, T. W. Ebbesen, Surface plasmon subwavelength optics. *Nature* **424**, 824-830 (2003).

31. D. A. Genov, A. K. Sarychev, V. M. Shalaev, Plasmon localization and local field distribution in metal-dielectric films. *Phys. Rev. E* **67**, 056611 (2003).

32. F. Brouers *et al.*, Theory of giant Raman scattering from semicontinuous metal films. *Phys. Rev. B* **55**, 13234-13245 (1997).

33. P. Christopher, H. L. Xin, S. Linic, Visible-light-enhanced catalytic oxidation reactions on plasmonic silver nanostructures. *Nature Chem.* **3**, 467-472 (2011).

34. W. Li, J. Valentine, Metamaterial Perfect Absorber Based Hot Electron Photodetection. *Nano Lett.* **14**, 3510-3514 (2014).

35. C. F. Bohren, D. R. Huffman, *Absorption and scattering of light by small particles*. (Wiley, Germany 1983).

36. N. Liu, S. Kaiser, H. Giessen, Magnetoinductive and Electroinductive Coupling in Plasmonic Metamaterial Molecules. *Adv. Mater.* **20**, 4521-4525 (2008).

37. J. M. Hao *et al.*, High performance optical absorber based on a plasmonic metamaterial. *Appl. Phys. Lett.* **96**, 251104 (2010).

38. A. F. Cihan, A. G. Curto, S. Raza, P. G. Kik, M. L. Brongersma, Silicon Mie resonators for highly directional light emission from monolayer MoS2. *Nature Photon.* **12**, 284-290 (2018).

39. Q. Zhao, J. Zhou, F. L. Zhang, D. Lippens, Mie resonance-based dielectric metamaterials. *Mater. Today* **12**, 60-69 (2009).

40. R. Camacho-Morales *et al.*, Nonlinear Generation of Vector Beams From AlGaAs Nanoantennas. *Nano Lett.* **16**, 7191-7197 (2016).

41. A. I. Kuznetsov, A. E. Miroshnichenko, M. L. Brongersma, Y. S. Kivshar, B. Luk'yanchuk, Optically resonant dielectric nanostructures. *Science* **354**, aag2472 (2016).

42. M. R. Shcherbakov *et al.*, Enhanced Third-Harmonic Generation in Silicon Nanoparticles Driven by Magnetic Response. *Nano Lett.* **14**, 6488-6492 (2014).

43. K. -T. Lee *et al.*, Electrically Biased Silicon Metasurfaces with Magnetic Mie Resonance for Tunable Harmonic Generation of Light. *ACS Photonics* **6**, 2663-2670 (2019).

44. G. T. Reed, G. Mashanovich, F. Y. Gardes, D. J. Thomson, Silicon optical modulators. *Nature Photon.* **4**, 518-526 (2010).

45. G. Lupke *et al.*, Optical 2nd-Harmonic Generation as a Probe of Electric-Field-Induced Perturbation of Centrosymmetric Media. *Opt. Lett.* **20**, 1997-1999 (1995).

46. I. Staude *et al.*, Tailoring Directional Scattering through Magnetic and Electric Resonances in Subwavelength Silicon Nanodisks. *ACS Nano* **7**, 7824-7832 (2013).

47. D. A. Smirnova, A. B. Khanikaev, L. A. Smirnov, Y. S. Kivshar, Multipolar Third-Harmonic Generation Driven by Optically Induced Magnetic Resonances. *ACS Photonics* **3**, 1468-1476 (2016).

48. J. E. Sipe, D. J. Moss, H. M. van Driel, Phenomenological theory of optical second- and third-harmonic generation from cubic centrosymmetric crystals. *Phys. Rev. B Condens. Matter.* **35**, 1129-1141 (1987).

49. H. W. K. Tom, T. F. Heinz, Y. R. Shen, 2nd-Harmonic Reflection from Silicon Surfaces and Its Relation to Structural Symmetry. *Phys. Rev. Lett.* **51**, 1983-1986 (1983).

50. Y. Q. An, R. Carriles, M. C. Downer, Absolute phase and amplitude of second-order nonlinear optical susceptibility components at Si(001) interfaces. *Phys. Rev. B* **75**, 241307 (2007).

51. D. Timbrell, J. W. You, Y. S. Kivshar, N. C. Panoiu, A comparative analysis of surface and bulk contributions to second-harmonic generation in centrosymmetric nanoparticles. *Sci. Rep.* **8**, 3586 (2018).

52. C. C. Jia *et al.*, Covalently bonded single-molecule junctions with stable and reversible photoswitched conductivity. *Science* **352**, 1443-1445 (2016).

53. O. Nevskyi, D. Sysoiev, A. Oppermann, T. Huhn, D. Woll, Nanoscopic Visualization of Soft Matter Using Fluorescent Diarylethene Photoswitches. *Angew. Chem. Int. Edit.* **55**, 12698-12702 (2016).

54. Y. Osakada, L. Hanson, B. X. Cui, Diarylethene doped biocompatible polymer dots for fluorescence switching. *Chem. Commun.* **48**, 3285-3287 (2012).

55. G. Naren *et al.*, An all-photonic full color RGB system based on molecular photoswitches. *Nature Commun.* **10**, 3996 (2019).

56. D. Kim, S. Y. Park, Multicolor Fluorescence Photoswitching: Color-Correlated versus Color-Specific Switching. *Adv. Opt. Mater.* **6**, 1800678 (2018).

57. P. Villanueva-Delgado, K. W. Kramer, R. Valiente, Simulating Energy Transfer and Upconversion in beta-NaYF4: Yb3+, Tm3+. *J. Phys. Chem. C* **119**, 23648-23657 (2015).

58. P. Dawson, M. Romanowski, Excitation Modulation of Upconversion Nanoparticles for Switch-like Control of Ultraviolet Luminescence. *J. Am. Chem. Soc.* **140**, 5714-5718 (2018).

59. A. Teitelboim *et al.*, Energy Transfer Networks within Upconverting Nanoparticles Are Complex Systems with Collective, Robust, and History-Dependent Dynamics. *J. Phys. Chem. C* **123**, 2678-2689 (2019).

60. J. C. Boyer, C. J. Carling, B. D. Gates, N. R. Branda, Two-Way Photoswitching Using One Type of Near-Infrared Light, Upconverting Nanoparticles, and Changing Only the Light Intensity. *J. Am. Chem. Soc.* **132**, 15766-15772 (2010).

61. J. P. Lai, Y. X. Zhang, N. Pasquale, K. B. Lee, An Upconversion Nanoparticle with Orthogonal Emissions Using Dual NIR Excitations for Controlled Two-Way Photoswitching. *Angew. Chem. Int. Edit.* **53**, 14419-14423 (2014).

62. K. Z. Zheng *et al.*, Rewritable Optical Memory Through High-Registry Orthogonal Upconversion. *Adv. Mater.* **30**, 1801726 (2018).

63. Y. S. Mi *et al.*, A photochromic upconversion nanoarchitecture: towards activatable bioimaging and dual NIR light-programmed singlet oxygen generation. *Chem. Sci.* **10**, 10231-10239 (2019).

64. S. Fischer, N. D. Bronstein, J. K. Swabeck, E. M. Chan, A. P. Alivisatos, Precise Tuning of Surface Quenching for Luminescence Enhancement in Core-Shell Lanthanide-Doped Nanocrystals. *Nano Lett.* **16**, 7241-7247 (2016).

65. N. J. J. Johnson *et al.*, Direct Evidence for Coupled Surface and Concentration Quenching Dynamics in Lanthanide-Doped Nanocrystals. *J. Am. Chem. Soc.* **139**, 3275-3282 (2017).

66. M. D. Wisser *et al.*, Improving Quantum Yield of Upconverting Nanoparticles in Aqueous Media via Emission Sensitization. *Nano Lett.* **18**, 2689-2695 (2018).

67. X. J. Xie *et al.*, Mechanistic Investigation of Photon Upconversion in Nd3+-Sensitized Core-Shell Nanoparticles. *J. Am. Chem. Soc.* **135**, 12608-12611 (2013).

68. S. L. Gai, C. X. Li, P. P. Yang, J. Lin, Recent Progress in Rare Earth Micro/Nanocrystals: Soft Chemical Synthesis, Luminescent Properties, and Biomedical Applications. *Chem. Rev.* **114**, 2343-2389 (2014).

69. J. J. He *et al.*, Plasmonic enhancement and polarization dependence of nonlinear upconversion emissions from single gold nanorod@SiO2@CaF2:Yb3+,Er3+ hybrid core-shell-satellite nanostructures. *Light Sci. Appl.* **6**, e16217 (2017).

70. Y. N. Ji *et al.*, Huge upconversion luminescence enhancement by a cascade optical field modulation strategy facilitating selective multispectral narrow-band near-infrared photodetection. *Light Sci. Appl.* **9**, 184 (2020).

71. J. A. Schuller *et al.*, Plasmonics for extreme light concentration and manipulation. *Nature Mater.* **9**, 193-204 (2010).

72. J. A. Dionne, L. A. Sweatlock, H. A. Atwater, A. Polman, Plasmon slot waveguides: Towards chip-scale propagation with subwavelength-scale localization. *Phys. Rev. B* **73**, 035407 (2006).

73. F. Ding, Y. Q. Yang, R. A. Deshpande, S. I. Bozhevolnyi, A review of gap-surface plasmon metasurfaces: fundamentals and applications. *Nanophotonics* **7**, 1129-1156 (2018).

74. A. Das, C. C. Mao, S. Cho, K. Kim, W. Park, Over 1000-fold enhancement of upconversion luminescence using water-dispersible metal-insulator-metal nanostructures. *Nature Commun.* **9**, 4828 (2018).

75. W. Xu *et al.*, Broadband Plasmonic Antenna Enhanced Upconversion and Its Application in Flexible Fingerprint Identification. *Adv. Opt. Mater.* **6**, 1701119 (2018).

76. H. L. Liu *et al.*, Tunable Resonator-Upconverted Emission (TRUE) Color Printing and Applications in Optical Security. *Adv. Mater.* **31**, 1807900 (2019).

77. F. B. Meng *et al.*, Orthogonally modulated molecular transport junctions for resettable electronic logic gates. *Nature Commun.* **5**, 3023 (2014).

78. T. Leydecker *et al.*, Flexible non-volatile optical memory thin-film transistor device with over 256 distinct levels based on an organic bicomponent blend. *Nature Nanotechnol.* **11**, 769-775 (2016).

79. O. Babii *et al.*, Direct Photocontrol of Peptidomimetics: An Alternative to Oxygen-Dependent Photodynamic Cancer Therapy. *Angew. Chem. Int. Edit.* **55**, 5493-5496 (2016).

80. N. A. Simeth, A. C. Kneuttinger, R. Sterner, B. Konig, Photochromic coenzyme Q derivatives: switching redox potentials with light. *Chem. Sci.* **8**, 6474-6483 (2017).

81. Y. Arai *et al.*, One-colour control of activation, excitation and deactivation of a fluorescent diarylethene derivative in super-resolution microscopy. *Chem. Commun.* **53**, 4066-4069 (2017).

82. B. Roubinet *et al.*, Fluorescent Photoswitchable Diarylethenes for Biolabeling and Single-Molecule Localization Microscopies with Optical Superresolution. *J. Am. Chem. Soc.* **139**, 6611-6620 (2017).

83. O. Nevskyi *et al.*, Fluorescent Diarylethene Photoswitches-A Universal Tool for Super-Resolution Microscopy in Nanostructured Materials. *Small* **14**, 1703333 (2018).

84. F. Wang *et al.*, Tuning upconversion through energy migration in core-shell nanoparticles. *Nature Mater.* **10**, 968-973 (2011).

85. Y. Wang, The role of an inert shell in improving energy utilization in lanthanide-doped upconversion nanoparticles. *Nanoscale* **11**, 10852-10858 (2019).

86. W. L. Li *et al.*, Separation of Photoactive Conformers Based on Hindered Diarylethenes: Efficient Modulation in Photocyclization Quantum Yields. *Angew. Chem. Int. Edit.* **53**, 4603-4607 (2014).

87. C. Wiebeler, S. Schumacher, Quantum Yields and Reaction Times of Photochromic Diarylethenes: Nonadiabatic Ab initio Molecular Dynamics for Normal- and Inverse-Type. *J. Phys. Chem. A* **118**, 7816-7823 (2014).

88. Y. C. Jeong, D. G. Park, I. S. Lee, S. I. Yang, K. H. Ahn, Highly fluorescent photochromic diarylethene with an excellent fatigue property. *J. Mater. Chem.* **19**, 97-103 (2009).

89. M. Morimoto, T. Sumi, M. Irie, Photoswitchable Fluorescent Diarylethene Derivatives with Thiophene 1,1-Dioxide Groups: Effect of Alkyl Substituents at the Reactive Carbons. *Materials* **10**, 1021 (2017).

90. Y. Takagi *et al.*, Turn-on mode fluorescent diarylethenes: Control of the cycloreversion quantum yield. *Tetrahedron* **73**, 4918-4924 (2017).

91. E. Barrez, G. Laurent, C. Pavageau, M. Sliwa, R. Metivier, Comparative photophysical investigation of doubly-emissive photochromic-fluorescent diarylethenes. *Phys. Chem. Chem. Phys.* **20**, 2470-2479 (2018).

92. W. H. Zhu *et al.*, Unprecedented Stability of a Photochromic Bisthienylethene Based on Benzobisthiadiazole as an Ethene Bridge. *Angew. Chem. Int. Edit.* **50**, 10986-10990 (2011).

93. S. Kawai *et al.*, Photochromic amorphous molecular materials based on dibenzothienylthiazole structure. *J. Mater. Chem.* **19**, 3606-3611 (2009).

94. A. L. Feng *et al.*, Distance-Dependent Plasmon-Enhanced Fluorescence of Upconversion Nanoparticles using Polyelectrolyte Multilayers as Tunable Spacers. *Sci. Rep.* **5**, 7779 (2015).

95. J. R. Niskala, W. You, Metal-Molecule-Metal Junctions via PFPE Assisted Nanotransfer Printing (nTP) onto Self-Assembled Monolayers. *J. Am. Chem. Soc.* **131**, 13202-13203 (2009).

96. C. Bauer, G. Kobiela, H. Giessen, Optical properties of two-dimensional quasicrystalline plasmonic arrays. *Phys. Rev. B* **84**, 193104 (2011).

97. C. Bauer, G. Kobiela, H. Giessen, 2D quasiperiodic plasmonic crystals. *Sci. Rep.* **2**, 681 (2012).

98. S. M. Lubin, A. J. Hryn, M. D. Huntington, C. J. Engel, T. W. Odom, Quasiperiodic Moire Plasmonic Crystals. *ACS Nano* **7**, 11035-11042 (2013).

99. M. Pollnau, D. R. Gamelin, S. R. Luthi, H. U. Gudel, M. P. Hehlen, Power dependence of upconversion luminescence in lanthanide and transition-metal-ion systems. *Phys. Rev. B* **61**, 3337-3346 (2000).

100. C. Zhang *et al.*, White-Light Emission from an Integrated Upconversion Nanostructure: Toward Multicolor Displays Modulated by Laser Power. *Angew. Chem. Int. Edit.* **54**, 11531-11535 (2015).

101. D. W. Lu *et al.*, Plasmon Enhancement Mechanism for the Upconversion Processes in NaYF4: Yb3+,Er3+ Nanoparticles: Maxwell versus Forster. *ACS Nano* **8**, 7780-7792 (2014).

102. J. Ern *et al.*, Ring-opening and -closure reaction dynamics of a photochromic dithienylethene derivative. *J. Phys. Chem. A* **106**, 1654-1660 (2002).

103. K. Stranius, K. Borjesson, Determining the Photoisomerization Quantum Yield of Photoswitchable Molecules in Solution and in the Solid State. *Sci. Rep.* **7**, 41145 (2017).

104. L. D. Barron, *Molecular light scattering and optical activity. 2nd edition* (Cambridge University Press, 2004).

105. L. A. Nguyen, H. He, C. Pham-Huy, Chiral drugs: an overview. *J. Biomed. Sci.* **2**, 85-100 (2006).

106. T. D. James, K. R. A. S. Sandanayake, S. Shinkai, Chiral Discrimination of Monosaccharides Using a Fluorescent Molecular Sensor. *Nature* **374**, 345-347 (1995).

107. H. S. M. Ali, R. Patzold, H. Bruckner, Gas chromatographic determination of amino acid enantiomers in bottled and aged wines. *Amino Acids* **38**, 951-958 (2010).

108. D. Q. Han, Z. P. Yao, Chiral mass spectrometry: An overview. *Trends. Analyt. Chem.* **123**, 115763 (2020).

109. A. Rocco, Z. Aturki, S. Fanali, Chiral separations in food analysis. *Trends. Analyt. Chem.* **52**, 206-225 (2013).

110. Y. Kubo, S. Maeda, S. Tokita, M. Kubo, Colorimetric chiral recognition by a molecular sensor. *Nature* **382**, 522-524 (1996).

111. L. Zhu, E. V. Anslyn, Facile quantification of enantiomeric excess and concentration with indicator-displacement assays: An example in the analyses of alpha-hydroxyacids. *J. Am. Chem. Soc.* **126**, 3676-3677 (2004).

112. Y. Mizuno, T. Aida, K. Yamaguchi, Chirality-memory molecule: Crystallographic and spectroscopic studies on dynamic molecular recognition events by fully substituted chiral porphyrins. *J. Am. Chem. Soc.* **122**, 5278-5285 (2000).

113. S. Nieto, V. M. Lynch, E. V. Anslyn, H. Kim, J. Chin, High-throughput screening of identity, enantiomeric excess, and concentration using MLCT transitions in CD spectroscopy. *J. Am. Chem. Soc.* **130**, 9232-9233 (2008).

114. P. Schreier, A. Bernreuther, M. Huffer, *Analysis of chiral organic molecules: Methodology and applications*. (De Gruyter, Berlin, 1995).

115. W. Ma *et al.*, Chiral Inorganic Nanostructures. *Chem. Rev.* **117**, 8041-8093 (2017).

116. A. Cecconello, L. V. Besteiro, A. O. Govorov, I. Willner, Chiroplasmonic DNA-based nanostructures. *Nature Rev. Mater.* **2**, 17039 (2017).

117. J. T. Collins *et al.*, Chirality and Chiroptical Effects in Metal Nanostructures: Fundamentals and Current Trends *Adv. Opt. Mater.* **5**, 1700182 (2018).

118. S. Yoo, Q. H. Park, Metamaterials and chiral sensing: a review of fundamentals and applications. *Nanophotonics* **8**, 249-261 (2019).

119. I. V. Lindell, A. H. Sihvola, S. A. Tretyakov, A. J. Viitanen, *Electromagnetic Waves in Chiral and Bi-isotropic Media*. (Artech House, Boston, 1994).

120. A. O. Govorov, Z. Y. Fan, Theory of Chiral Plasmonic Nanostructures Comprising Metal Nanocrystals and Chiral Molecular Media. *Chemphyschem* **13**, 2551-2560 (2012).

121. Y. Q. Tang, A. E. Cohen, Optical Chirality and Its Interaction with Matter. *Phys. Rev. Lett.* **104**, 163901 (2010).

122. S. P. Rodrigues *et al.*, Intensity-dependent modulation of optically active signals in a chiral metamaterial. *Nature Commun.* **8**, 14602 (2017).

123. M. Hentschel, M. Schaferling, X. Y. Duan, H. Giessen, N. Liu, Chiral plasmonics. *Sci. Adv.* **3**, e1602735 (2017).

124. M. J. Urban *et al.*, Chiral Plasmonic Nanostructures Enabled by Bottom-Up Approaches. *Annu. Rev. Phys. Chem.* **70**, 275-299 (2019).

125. X. T. Kong, L. V. Besteiro, Z. M. Wang, A. O. Govorov, Plasmonic Chirality and Circular Dichroism in Bioassembled and Nonbiological Systems: Theoretical Background and Recent Progress. *Adv. Mater.* **32**, 1801790 (2020).

126. Y. Y. Lee, R. M. Kim, S. W. Im, M. Balamurugan, K. T. Nam, Plasmonic metamaterials for chiral sensing applications. *Nanoscale* **12**, 58-66 (2020).

127. Z. L. Cao *et al.*, Chirality Transfer from Sub-Nanometer Biochemical Molecules to Sub-Micrometer Plasmonic Metastructures: Physiochemical Mechanisms, Biosensing, and Bioimaging Opportunities. *Adv. Mater.* **32**, 1907151 (2020).

128. N. A. Abdulrahman *et al.*, Induced Chirality through Electromagnetic Coupling between Chiral Molecular Layers and Plasmonic Nanostructures. *Nano Lett.* **12**, 977-983 (2012).

129. H. Zhang, A. O. Govorov, Giant circular dichroism of a molecule in a region of strong plasmon resonances between two neighboring gold nanocrystals. *Phys. Rev. B* **87**, 075410 (2013).

130. A. O. Govorov, Plasmon-Induced Circular Dichroism of a Chiral Molecule in the Vicinity of Metal Nanocrystals. Application to Various Geometries. *J. Phys. Chem. C* **115**, 7914-7923 (2011).

131. A. O. Govorov, Z. Y. Fan, P. Hernandez, J. M. Slocik, R. R. Naik, Theory of Circular Dichroism of Nanomaterials Comprising Chiral Molecules and Nanocrystals: Plasmon Enhancement, Dipole Interactions, and Dielectric Effects. *Nano Lett.* **10**, 1374-1382 (2010).

132. Y. Q. Tang, A. E. Cohen, Enhanced Enantioselectivity in Excitation of Chiral Molecules by Superchiral Light. *Science* **332**, 333-336 (2011).

133. Y. Zhao *et al.*, Chirality detection of enantiomers using twisted optical metamaterials. *Nature Commun.* **8**, 14180 (2017).

134. Y. Zhao, A. A. E. Saleh, J. A. Dionne, Enantioselective Optical Trapping of Chiral Nanoparticles with Plasmonic Tweezers. *ACS Photonics* **3**, 304-309 (2016).

135. Y. Qu *et al.*, Chiral Near-Fields Induced by Plasmonic Chiral Conic Nanoshell Metallic Nanostructure for Sensitive Biomolecule Detection. *J. Phys. Chem. C* **124**, 13912-13919 (2020).

136. J. C. Boyer, C. J. Carling, B. D. Gates, N. R. Branda, Two-Way Photoswitching Using One Type of Near-Infrared Light, Upconverting Nanoparticles, and Changing Only the Light Intensity. *J Am Chem Soc* **132**, 15766-15772 (2010).

137. S. H. Wen *et al.*, Advances in highly doped upconversion nanoparticles. *Nature Commun.* **9**, 2415 (2018).

138. A. Nadort, J. B. Zhao, E. M. Goldys, Lanthanide upconversion luminescence at the nanoscale: fundamentals and optical properties. *Nanoscale* **8**, 13099-13130 (2016).

139. C. Siefe *et al.*, Sub-20 nm Core-Shell-Shell Nanoparticles for Bright Upconversion and Enhanced Forster Resonant Energy Transfer. *J. Am. Chem. Soc.* **141**, 16997-17005 (2019).

140. S. Fischer, N. D. Bronstein, J. K. Swabeck, E. M. Chan, A. P. Alivisatos, Precise Tuning of Surface Quenching for Luminescence Enhancement in Core-Shell Lanthanide-Doped Nanocrystals. *Nano Lett* **16**, 7241-7247 (2016).

141. L. Kang *et al.*, Preserving Spin States upon Reflection: Linear and Nonlinear Responses of a Chiral Meta-Mirror. *Nano Lett.* **17**, 7102-7109 (2017).

142. A. H. Sihvola, *Electromagnetic Mixing Formulas and Applications*. IEEE Electromagnetic waves series (Institution of Engineering and Technology, London, 1999).

143. L. Hu, Y. Z. Huang, L. J. Pan, Y. R. Fang, Analyzing intrinsic plasmonic chirality by tracking the interplay of electric and magnetic dipole modes. *Sci. Rep.* **7**, 11151 (2017).

144. A. Y. Zhu *et al.*, Giant intrinsic chiro-optical activity in planar dielectric nanostructures. *Light: Science & Applications* **7**, 17158 (2018).

145. B. Semnani, J. Flannery, R. Al Maruf, M. Bajcsy, Spin-preserving chiral photonic crystal mirror. *Light Sci. Appl.* **9**, 23 (2020).

146. D. Patterson, M. Schnell, J. M. Doyle, Enantiomer-specific detection of chiral molecules via microwave spectroscopy. *Nature* **497**, 475-477 (2013).

147. S. Lee, J. H. Kang, S. Yoo, Q. H. Park, Robust numerical evaluation of circular dichroism from chiral medium/nanostructure coupled systems using the finite-element method. *Sci. Rep.* **8**, 8406 (2018).

148. K. -T. Lee *et al.*, Simultaneous Enhancement of Upconversion and Downshifting Luminescence via Plasmonic Structure. *Nano Lett.* **15**, 2491-2497 (2015).

149. I. H. Ahn *et al.*, A Multi-Functional Highly Efficient Upconversion Luminescent Film with an Array of Dielectric Microbeads Decorated with Metal Nanoparticles. *Adv. Funct. Mater.* **30**, 1909445 (2020).

150. D. M. Wu, A. Garcia-Etxarri, A. Salleo, J. A. Dionne, Plasmon-Enhanced Upconversion. *J. Phys. Chem. Lett.* **5**, 4020-4031 (2014).

151. D. W. Lu, C. C. Mao, S. K. Cho, S. Ahn, W. Park, Experimental demonstration of plasmon enhanced energy transfer rate in $NaYF_4$:Yb^{3+}, Er^{3+} upconversion nanoparticles. *Sci. Rep.* **6**, 18894 (2016).

152. A. Heller, B. Feldman, Electrochemical glucose sensors and their applications in diabetes management. *Chem. Rev.* **108**, 2482-2505 (2008).

153. D. Smith, J. Pendry, M. Wiltshire, Metamaterials and negative refractive index. *Science* **305**, 788-792 (2004).

154. C. M. Soukoulis, M. Wegener, Past achievements and future challenges in the development of three-dimensional photonic metamaterials. *Nature Photon.* **5**, 523-530 (2011).

155. Y. Liu, X. Zhang, Metamaterials: a new frontier of science and technology. *Chem. Soc. Rev.* **40**, 2494-2507 (2011).

156. W. Cai, V. M. Shalaev, *Optical metamaterials: fundamentals and applications*. (Springer, 2010).

157. J. B. Pendry, A. Holden, W. Stewart, I. Youngs, Extremely low frequency plasmons in metallic mesostructures. *Phys. Rev. Lett.* **76**, 4773-4776 (1996).

158. J. B. Pendry, A. Holden, D. Robbins, W. Stewart, Magnetism from conductors and enhanced nonlinear phenomena. *IEEE Trans. Microw. Theory Techn.* **47**, 2075-2084 (1999).

159. J. K. Gansel *et al.*, Gold helix photonic metamaterial as broadband circular polarizer. *Science* **325**, 1513-1515 (2009).

160. A. Kuzyk *et al.*, DNA-based self-assembly of chiral plasmonic nanostructures with tailored optical response. *Nature* **483**, 311-314 (2012).

161. D. R. Smith, N. Kroll, Negative refractive index in left-handed materials. *Phys. Rev. Lett.* **85**, 2933-2936 (2000).

162. J. Valentine *et al.*, Three-dimensional optical metamaterial with a negative refractive index. *Nature* **455**, 376-379 (2008).

163. V. Mocella *et al.*, Self-collimation of light over millimeter-scale distance in a quasi-zero-average-index metamaterial. *Phys. Rev. Lett.* **102**, 133902 (2009).

164. E. J. R. Vesseur, T. Coenen, H. Caglayan, N. Engheta, A. Polman, Experimental Verification of n= 0 Structures for Visible Light. *Phys. Rev. Lett.* **110**, 013902 (2013).

165. J.-T. Shen, P. B. Catrysse, S. Fan, Mechanism for designing metallic metamaterials with a high index of refraction. *Phys. Rev. Lett.* **94**, 197401 (2005).

166. M. Choi *et al.*, A terahertz metamaterial with unnaturally high refractive index. *Nature* **470**, 369-373 (2011).